Charles University in Prague
Faculty of Mathematics and Physics

DOCTORAL THESIS

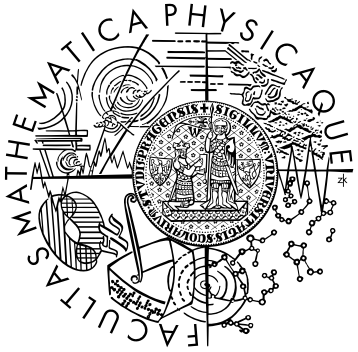

Marie Hrudková

Planets by other suns

Astronomical Institute of the Charles University

Supervisor: **Prof. RNDr. Petr Harmanec, DrSc.**
Advisers: **Dr. Ian Skillen, Dr. Chris Benn, Doc. RNDr. Marek Wolf,CSc., Prof. Dr. Artie Hatzes, Prof. Dr. Edward F. Guinan**

A dissertation submitted to Committee for Doctoral Study Programme F1 of MFF UK in partial fulfillment of the requirements for the degree of Doctor of Philosophy.

Amicus certus in re incerta cernitur.
Cicero

This thesis was supported by the grants 205/08/H005 and 205/06/0304 of the Czech Science Foundation and from the Research Program MSM0021620860 of the Ministry of Education of the Czech Republic. The data used in this thesis were made with the William Herschel Telescope operated by the Isaac Newton Group, with the Nordic Optical Telescope operated jointly by Denmark, Finland, Iceland, Norway, and Sweden, both located in the Spanish Observatorio del Roque de los Muchachos of the Instituto de Astrofísica de Canarias on the island of La Palma, and with the Alfred-Jensch Telescope in Tautenburg, Germany. The data have been taken using ALFOSC, which is owned by the Instituto de Astrofísica de Andalucia (IAA) and operated at the Nordic Optical Telescope under agreement between IAA and the NBIfAFG of the Astronomical Observatory of Copenhagen.

I would like to take this opportunity to thank my supervisor Prof. Petr Harmanec for his patient leadership and support over the whole period and my advisers Ian Skillen and Chris Benn for their invaluable support, discussions and a fruitful collaboration, which I hope will continue also in the future. I am grateful to my parents and sister, for their love and support during the whole period, and to Raine.

I would like to thank Don Pollacco, Neale Gibson, Yogesh Joshi, Thomas Augusteijn and Prof. Edward Guinan for useful discussions. I would also like to thank David Nesvorný, who helped with transit timing variations analysis. I am grateful to Prof. Artie Hatzes and Eike Guenther, for their help and discussions on how to measure radial velocities with the echelle spectrograph and to Eike for his comments on plage regions. I would like to thank all my colleagues at the Astronomical Institute of the Charles University for a good working environment and support, mainly to Doc. Marek Wolf, then Michal, Zetor, Pepa, Mirek and Kuba for discussions, lunches and sharing experiences.

Part of this thesis was done at the Isaac Newton Group on La Palma. I would like to show my deepest gratitude for all the staff members who contributed to a very friendly atmosphere. I am thankful to Juan, Chelo, Mónica, Lourdes and Yasmín for the administration help, Mischa for the infrared reductions, Dan for IDL hints and Sam for Unix help.

Special thanks belong to my La Palma friends that made my life happy – Auni, Tiina, Kat, Ian, Miguel, Sam and Craige. I am greatful to Ivana, Jirka, Zuzka, Táňa, Vlasta and Erika for being close when needed.

I declare that this thesis was written by my own with the use of cited resources.

In Prague

Marie Hrudková

Contents

Title: *Planets by other suns*
Author: *Marie Hrudková, mariehrudkova@gmail.com*
Institute: *Astronomical Institute of the Charles University*
Supervisor: *Prof. RNDr. Petr Harmanec, DrSc., hec@sirrah.troja.mff.cuni.cz*
Advisers: *Dr. Ian Skillen, wji@ing.iac.es,*
Dr. Chris Benn, crb@ing.iac.es,
Doc. RNDr. Marek Wolf, CSc., wolf@cesnet.cz,
Prof. Dr. Artie Hatzes, artie@tls-tautenburg.de,
Prof. Dr. Edward F. Guinan, edward.guinan@villanova.edu
Study branch: *f1 – Theoretical physics, astronomy, and astrophysics*
Keywords: *Planetary systems – stars: individual: HD 189733, TrES-1, 51 Peg – techniques: photometric – techniques: radial velocities.*

Abstract

Exploring distant planetary systems can help us to understand our own. In this thesis, two methods are further investigated for this purpose. First, to detect Earth-mass planets high-accurate measurements of radial velocities and also accurate barycentric corrections are needed. The program for computing these corrections was developed. The accuracy achieved is few $\mathrm{cm\,s^{-1}}$ and hundredths of s for radial velocity and time corrections, respectively. The program was used to compute barycentric corrections of the 51 Peg system, for which measurements with the 2-m Alfred-Jensch Telescope were taken and analysed. Second, the method of planetary transits was used for a transit timing study of two transiting exoplanetary systems, HD 189733 and TrES-1. The data were taken with the 4.2-m William Herschel Telescope and the 2.6-m Nordic Optical Telescope, La Palma. The program using the Markov-Chain Monte Carlo simulations was written for a purpose of a transit timing study to derive system parameters, mid-transit times and their uncertainties. An additional planet in a transiting system perturbs the motion of the transiting planet, and the interval between the mid-eclipses is not constant. Deviations from the predicted mid-transit times which can reveal the presence of other bodies in the system were analysed.

Mottoes:

The diversity of the phenomena of nature is so great, and the treasures hidden in the heavens so rich, precisely in order that the human mind shall never be lacking in fresh nourishment.

Johannes Kepler

A time would come when men should be able to stretch out their eyes... They should see the planets like our Earth.

Christopher Wren, Inauguration Speech, Gresham College, 1657

1 Preface

This thesis collects results obtained during my Ph.D. study program on the topic of extrasolar planetary systems. One of the main subject is the improvement of accuracy of barycentric corrections, with an application to the extrasolar system 51 Peg. The second main topic is a determination of mid-transit times of selected transiting extrasolar systems with subsequent analyses of results.

The overview of the physics and known properties of extrasolar planetary systems is presented in section §2. Planetary formation and evolution theories in a context with transiting extrasolar planets are summarized in section §2.1. Interesting connections between planetary system properties and their formation and evolution history may be revealed via a statistical analysis of known extrasolar systems. This is explored for all and only transiting extrasolar planets in sections §2.2 and §2.3.6, respectively. Different detection methods allow discoveries of planets with variety of characteristics due to the fact that each method is sensitive differently to distinct planetary parameters. Their overview is given in sections §2.3, §2.4 and §2.5.

In section §3 the program for computations of barycentric radial velocity and time corrections is presented. The physical background is also explained and the resulting corrections are compared to those from similar programs.

The photometry of transiting extrasolar planets is discussed in section §4. Difficulties to obtain accurate photometric measurements are summarized in section §4.1, and the procedure how the system parameters were computed from a light curve is presented in section §4.2.

Sections §5, §6 and §7 present an application of previous results to the real data. The radial velocities of 51 Peg system, to which the barycentric corrections computed in section §3 were applied, were analysed in section §5. In sections §6 and §7 light curves of the transiting extrasolar systems HD 189733 and TrES-1, respectively, were modelled using the procedure presented in section §4.2, and the accurate mid-transit times were determined. They were further investigated because the deviations from the predicted mid-transit times can reveal the presence of additional bodies in the transiting system, or place limits on their existence. The results are summarized in section §8.

2 Introduction

More than two thousand years ago the Greek philosopher Epicuros speculated that there are many other inhabited words besides our own in the Universe. In 1584 the Italian philosopher Giordano Bruno, the proponent of heliocentrism and infinity of the Universe, published his model, where the Sun was an ordinary star and all other similar stars had their own planets. Bruno saw a system of sun/star with planets as a fundamental unit of the Universe. These were one of the first recorded human thoughts about the existence of extrasolar planets.

First real attempts to detect extrasolar planets began in the first half of the 20th century using the astrometric method, where low-mass companions can be discovered by periodic changes in the star position. Strand (1943) published the detection of an extrasolar planet by 61 Cyg and later van de Kamp (1963) reported the detection of planets by Barnard's Star. Both discoveries were based on observations from Sproul Observatory and later shown to be spurious detections.

Unfortunately, the astrometric method was not the best choice for detecting extrasolar planets due to an insufficient accuracy of astrometric measurements at that time. However, observing stars spectroscopically could reveal the existence of a planet by detecting radial velocity (RV) changes of a parent star due to its orbital motion around a common centre of gravity. Therefore several groups started to monitor RVs of different star samples. First promising discovery was published by Campbell et al. (1988), who found evidence of a probable third body of planetary mass with the period ~ 2.7 years in the RV residuals of the spectroscopic binary star γ Cep. Walker et al. (1992) confirmed the period of ~ 2.52 years, but found that Ca II emission line index varied with the same period and concluded that the observed variations are most probably due to star's rotation. Later, Hatzes et al. (2003) published a new analysis using four independent data sets spanning more than 20 years, and confirmed the planetary-mass companion with a period of ~ 2.48 years and a minimum mass $M_p \sin i = 1.7$ $\mathrm{M_J}$, where M_p is a mass of the planet, $\mathrm{M_J}$ is a mass of Jupiter and i is the inclination of the planetary orbit, defined so that $i = 0^\circ$ when the planetary orbit lies in the plane of the sky.

Other promising detection was published by Latham et al. (1989). They presented a spectroscopic evidence for a companion to the solar-like star HD 114762 with a period of 84 days and $M_p \sin i = 11$ $\mathrm{M_J}$. They suggested that the companion is probably a brown dwarf, but may even be a giant planet. The uncertainty in mass is due to the unknown inclination, i. A brown dwarf is an object which has a sufficient mass to reach a temperature in its centre needed for a synthesis of deuterium, but not hydrogen. To date no definition of an extrasolar planet exists. A planet is usually considered as an extrasolar planet if it orbits around a star other than the Sun, and if its mass is less than the mass needed for a synthesis of deuterium, which is around 13 $\mathrm{M_J}$ for a solar-composition planet.

In 1992, an unexpected planetary system was found by Wolszczan & Frail (1992) around the millisecond pulsar PSR 1257+12. Planets were discovered via periodic changes in the pulsar signal arrival times. It is not clear, however, whether they survived the giant star explosion or were captured later by gravitational forces of the neutron star.

In 1995, the discovery of an extrasolar planet by the solar-like star 51 Peg was announced by Mayor & Queloz (1995). This is the milestone of exoplanet studies for many reasons. First of all, it was a clear evidence of the planetary-mass companion to the solar-like star, with the mass $M_p \sin i = 0.47$ M_J. Second, the planet was found to orbit very closely to its parent star with the period of only 4.23 days. It was the time when theories of planetary system formation and evolution needed to be revised in order to explain the existence of a planet at such a close distance to its parent star. This discovery was then followed by many others presenting new planets found spectroscopically. Since then, about 290 out of 370[1] extrasolar planets known to date were discovered with this method due to the progress in instrumentation and data reduction software providing more accurate RV measurements.

Another great success was a discovery of a first planet transiting in front of its parent star HD 209458 (Charbonneau et al., 2000a; Henry et al., 2000; Mazeh et al., 2000). The 60 transiting extrasolar planets known to date are the only ones for which we know the key physical parameters such as their mass, radius, and inferred internal structure.

About 30 % of all the known extrasolar planets are 'hot Jupiters', planets with masses close to or more than of Jupiter, orbiting typically within 0.1 AU (with orbital periods less than 10 days for a planet around a solar-type star), where 1 AU is defined as the mean distance between the Earth and the Sun and is approximately 1.5×10^{11} m. The name 'hot Jupiters' comes from their high equilibrium temperature due to the small separations from their parent stars. Nowadays, also another class of extrasolar planets is observed, so called 'very hot Jupiters', with orbital periods less than 2 days.

2.1 The planetary formation and migration

There are two main theories of giant planet formation. In one of them, initially a rocky core of several Earth masses forms by planetesimal collisions in a protoplanetary disk, hence its name the 'core accretion model', and then a massive gaseous envelope is accreted, all on a timescale of less than 1 Myr (Chambers, 2006) or several Myr (Alibert et al., 2005). According to the competing 'disk instability model' planets form by a gravitational collapse of disk fragments in less than a thousand years (Mayer et al., 2002). Then after a few more thousand years the dust and planetesimals inside the gaseous protoplanets can settle to the centre of the protoplanet by local pressure gradients and low mass solid core is formed (Boss et al., 2002).

It seems that both giant planet formation theories are needed to explain the diversity of extrasolar planets detected to date. Giant planets with very large core masses are better explained by the 'core accretion', whereas a formation via the 'disk instability' could explain gas giants in very low metallicity systems. Although the 'core accretion' is generally accepted for already three decades (Mizuno, 1980), 'disk instability' is only one decade old as a serious competing theory to 'core accretion' (Boss, 2008, 2009).

Nevertheless, none of the two theories can explain the proximity of 'hot Jupiters' to their parent stars. The standard explanation for this is that planets form further out in

[1]The Extrasolar Planets Encyclopedia: http://exoplanet.eu

the protoplanetary disk and then migrate towards the parent star. There are different mechanisms how the planet migration could be initiated and it is still not clear whether one is dominant (see section §2.3.3).

Terrestrial-type planets play an interesting role in planet formation scenarios. They are expected to form by the collisional accumulation of the planetesimals in the protoplanetary disk similarly as rocky cores of giant planets in 'core accretion model'. According to Zhou et al. (2005) close-in terrestrial planets are unlikely in the 'disk instability model', but should be abundant in the 'core accretion model'. Therefore the detection of such close-in terrestrial planets would distinguish which mechanism for the planet formation is dominant.

2.2 Statistical properties

Formation processes produce a surprising variety of exoplanetary systems: planets with masses considerably larger than that of Jupiter, planets on highly eccentric orbits, planets orbiting as close as 4 stellar radii, planets in stellar binary systems, and planets in resonant multiplanet systems. Understanding such a wide variety is a goal of planet formation theories. A statistical analysis of known extrasolar systems may reveal interesting connections between planetary system properties and their formation and evolution history.

The most recent statistical analysis was carried out by Udry & Santos (2007), who discussed many statistical aspects of extrasolar systems. First, the most direct statistical property of planet-search programs is the percentage of positive detections. For the ELODIE program, Naef et al. (2005) estimated for planets with masses more than 0.5 M_J a corrected fraction of $0.7 \pm 0.5\,\%$ for 'hot Jupiters' with $P \leq 5$ days, and of $7.3 \pm 1.5\,\%$ for planets with periods less than 3900 days. In this section we use the most recent data from J. Schneider's Extrasolar Planets Encyclopaedia and make an updated statistical research to Udry & Santos (2007) of the known extrasolar planets.

Other interesting properties directly obtained from RV measurements are the minimum mass of the companion and its separation from the central star. The first produces a bimodal distribution, which results from occurence of planets with masses usually less than 5 M_J and stellar binaries with masses more than 75 M_J. The interval between the two populations, the 'brown dwarf desert', corresponding to masses between ~ 15 M_J and ~ 75 M_J, contains only a few objects. In Fig. 1a we display the planetary mass distribution where the steep rise toward the lowest masses is observed. Exploring planet separations revealed a high number of planets with periods around 3 days, which is most probably the result of a planetary migration, and then a rise of a number of planets with increasing distance from a parent star, which indicates that a large population of yet undetected Jupiter-mass planets may exist between 3 – 20 AU (see Fig. 1b).

However, as displayed in Fig. 2a, a lack of massive planets on short-period orbits in the period-mass diagram presented by Udry & Santos (2007) disappeared with recent discoveries of transiting planets with masses ≥ 2 M_J and periods of a few days. Nevertheless, two other relationships proposed by Udry & Santos (2007) are still valid. First, extrasolar planets with orbital periods longer than about 3 days have eccentricities larger than those of giant planets in the Solar system, as shown in Fig. 2b. Second, the more massive planets

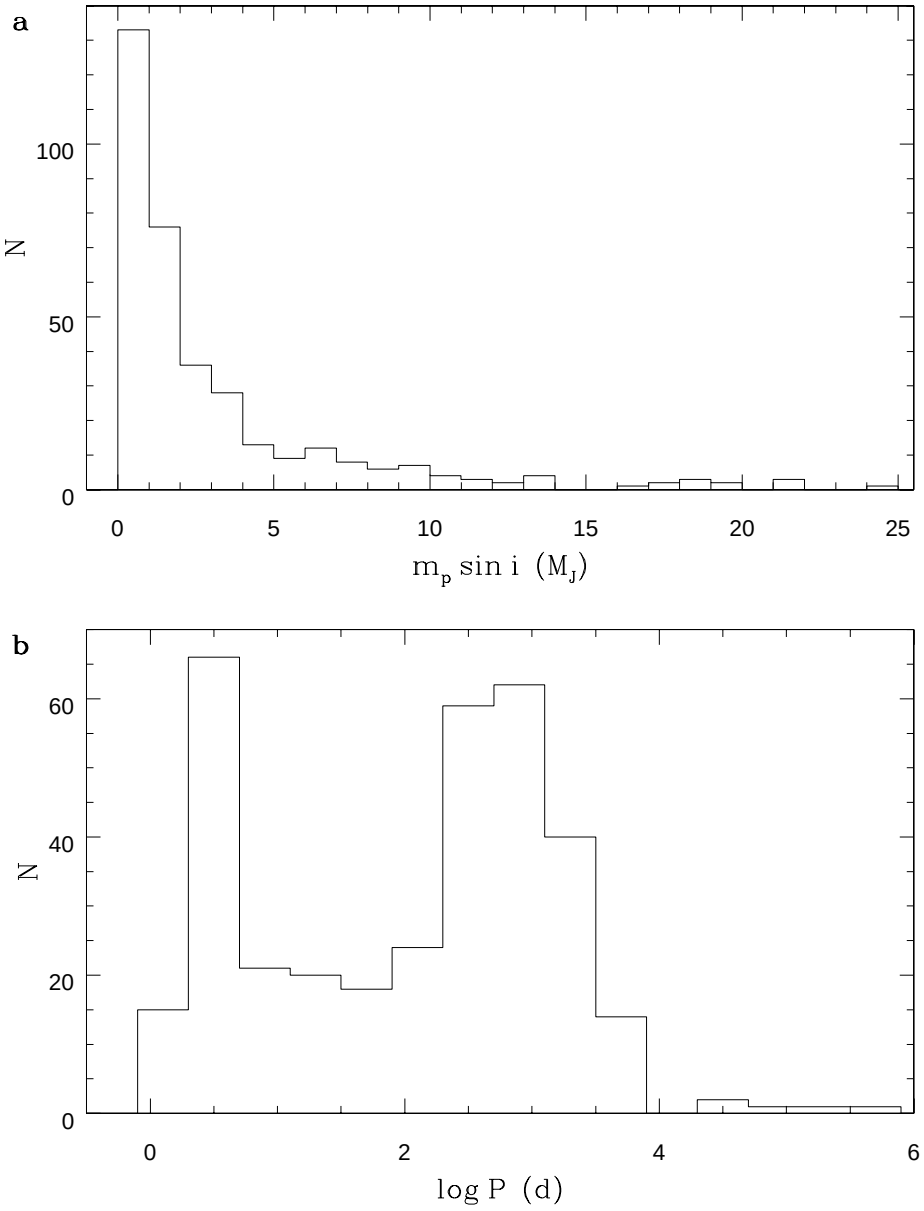

Figure 1: (a) Planetary mass distribution in the linear scale with the steep rise toward the lowest masses. (b) Period distribution shows a high number of planets with periods around 3 days and then a rise of a number of planets with increasing distance from a parent star. N indicates the number of exoplanets in each selected interval. Data were taken from J. Schneider's Extrasolar Planets Encyclopaedia and all extrasolar planets for which the corresponding quantities are known were included.

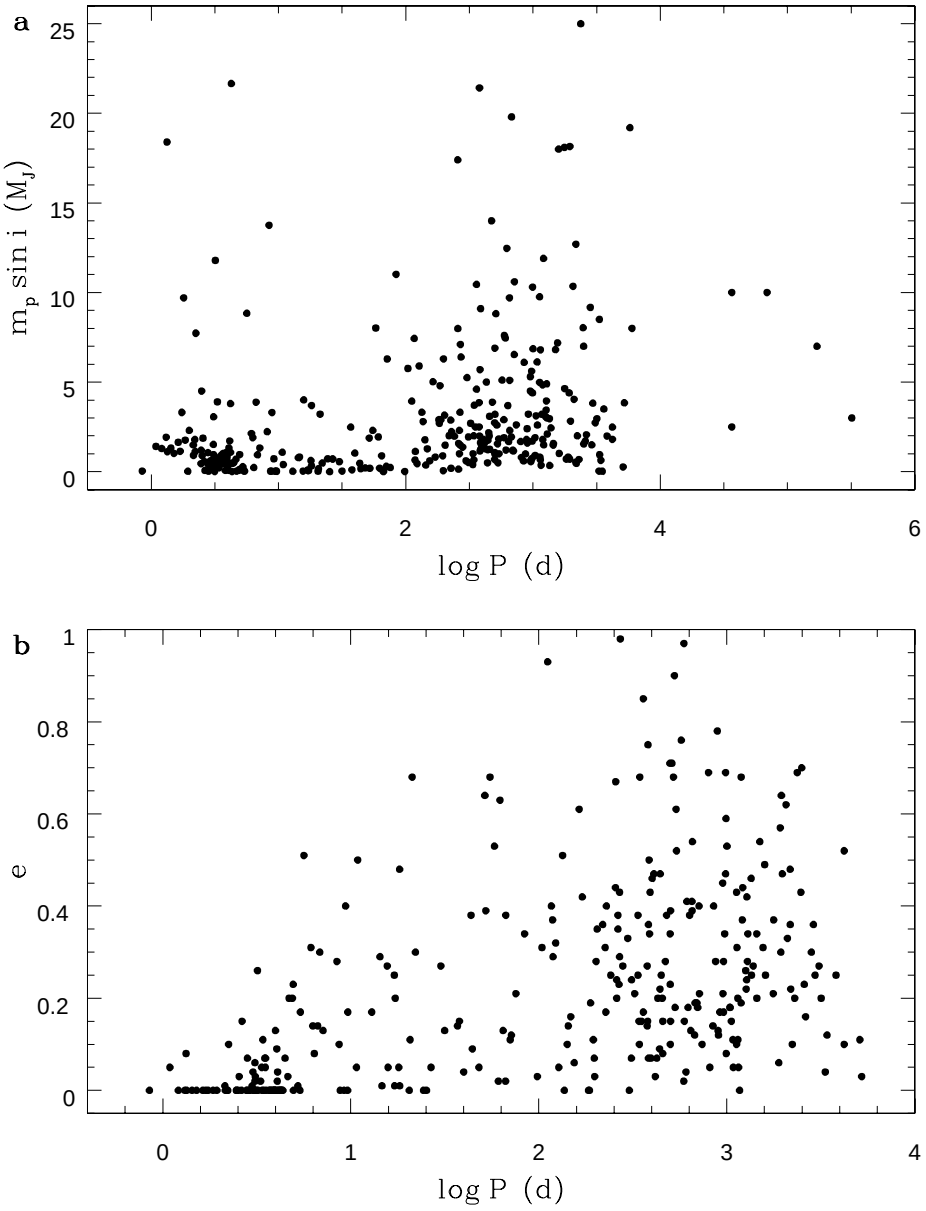

Figure 2: (a) Period-mass distribution shows a presence of planets with masses ≥ 2 M_J *and periods of a few days, and so the lack of massive planets on short-period orbits proposed by Udry & Santos (2007) is not confirmed. (b) Period-eccentricity diagram where planets with orbital periods longer than about 3 days have larger eccentricities than shorter period planets. Data were taken from J. Schneider's Extrasolar Planets Encyclopaedia and all extrasolar planets for which the corresponding quantities are known were included.*

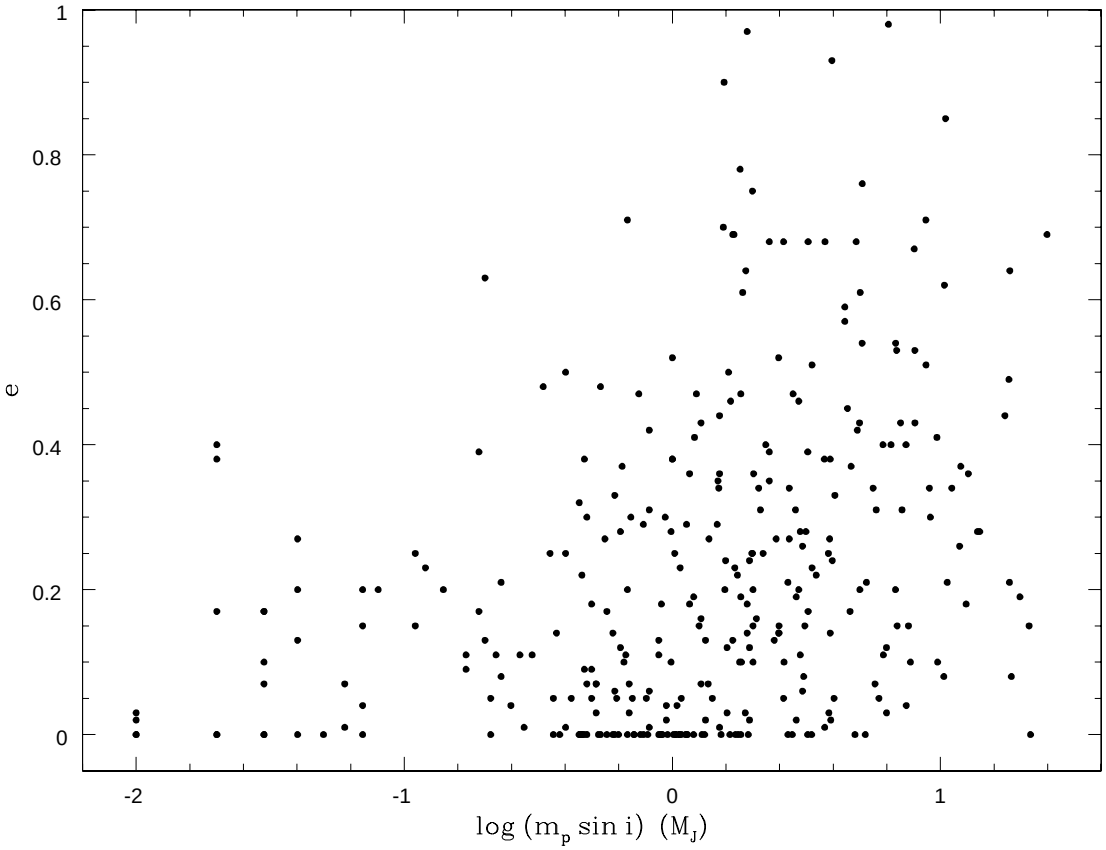

Figure 3: Mass-eccentricity diagram revealing that the more massive planets have higher eccentricities than planets with lower masses. Data were taken from J. Schneider's Extrasolar Planets Encyclopaedia and all extrasolar planets for which the corresponding quantities are known were included.

have higher eccentricities than planets with lower masses as presented in Fig. 3. Unfortunately, none of the so far proposed mechanisms inducing eccentricity has been able to explain the whole observed eccentricity distribution.

Udry & Santos (2007) explored statistical properties of multiplanet systems and concluded that they are the same as for single-planet systems. Therefore the idea that planets form naturally in multiplanet systems is supported.

The interesting finding that planet hosting stars are systematically metal-rich came soon after discoveries of first extrasolar planets (Gonzalez, 1997). First detailed spectroscopic studies (Santos et al., 2001) using the same spectroscopic-analysis technique for stars with and without planets confirmed the planet-metallicity correlation for the observed extrasolar systems. Nowadays, the metallicity excess for planet hosting stars is still observed (see Fig. 4) and its origin from a cloud of gas and dust forming a star and planetary system is preferred over the process of adding a metal-rich material onto a star once it is formed.

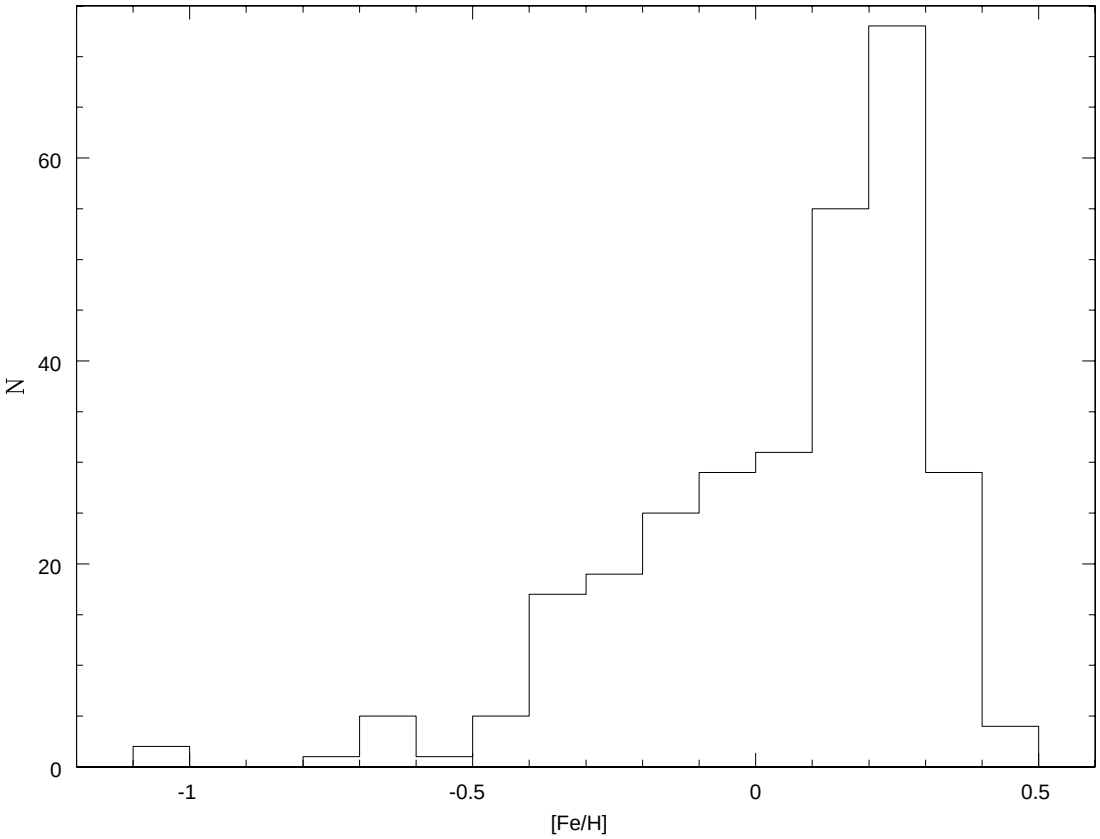

Figure 4: Stellar metallicity distribution with the rise toward the higher metallicities indicates that planet hosting stars are systematically metal-rich. N indicates the number of systems in each selected interval. Data were taken from J. Schneider's Extrasolar Planets Encyclopaedia and all extrasolar planets for which the corresponding quantities are known were included.

Observed planet-metallicity connection has an interesting impact on planet formation theories. According to the 'disk instability' model, planetary formation is independent of the star/disk metallicity, whereas the opposite is truth for the 'core accretion', for which it is easier to form planets from a metal-rich material.

The planet-metallicity correlation exists for stars hosting giant planets, but it seems not to be present for stars harbouring less massive planets. The explanation could be that a decrease of the disk metallicity will increase the time needed to form planetary cores and they may not reach enough mass to start a gas accretion. Exploring all these connections may thus help to understand how the planetary systems form and evolve.

2.3 Transiting exoplanets

Transiting extrasolar planets have their orbits oriented so that the Earth lies nearly in their orbital plane. Once during the planet's orbital period the exoplanet will transit in front of the stellar disk (primary transit) and/or will be occulted by the stellar disk (secondary transit or occultation).

2.3.1 Fundamental properties

When a planet transits, fits to the transit light curve provide the planetary orbital inclination, i, which is used to estimate the planetary mass, M_p, from the minimum mass value, $M_p \sin i$. This requires accurate RV measurements, as well as an estimate of the stellar mass, $M_\star$, which is often the largest source of uncertainties of system parameters derived from transits. From a transit light curve, the planetary radius, R_p, can be also fitted. Then the average density and surface gravity can be estimated, which in turn provides fundamental constraints on models of planet's physical structure. Particularly, determination of the planetary radius should indicate a presence (or absence) of a core of solid material, which would (or would not) indicate a gas accretion onto a core of ice and rock embedded in a protoplanetary disk.

Ignoring limb darkening, the four basic observables, displayed in Fig. 5, are the mid-transit time, T_c, the transit depth, δ, the full duration of the transit, D, and the duration of totality, d, which is the transit duration between ingress and egress when the whole planet is projected onto the stellar disk. Ingress (egress) is the time when the planet goes into (out of) the transit and the stellar disk is covered only partially. From multiple transits or from RV measurements, the orbital period, P, can be determined. If we adopt the physical constants recommended by Harmanec & Mayer (2008), the Kepler's third law becomes:

$$a^3 = 74.48358 P^2 (M_p + M_\star), \tag{1}$$

where a is the planetary orbital semi-major axis expressed in solar radii, $M_\star$ and M_p are in solar masses, and P is in days. Other parameters like planetary and stellar radius, R_p and $R_\star$, respectively, and impact parameter, b, defined as the projected distance between the planet and star centres in mid-transit time in units of $R_\star$ (see Fig. 5), can be determined using formulas given by Seager & Mallén-Ornelas (2003) for light curves of transiting systems with planets on circular orbits:

$$\delta = \left(\frac{R_p}{R_\star} \right)^2, \tag{2}$$

$$b = \frac{a}{R_\star} \cos i, \tag{3}$$

$$D = \frac{P}{\pi} \arcsin \left(\frac{R_\star}{a} \left[\frac{[1 + (R_p/R_\star)]^2 - [(a/R_\star) \cos i]^2}{1 - \cos^2 i} \right]^{1/2} \right). \tag{4}$$

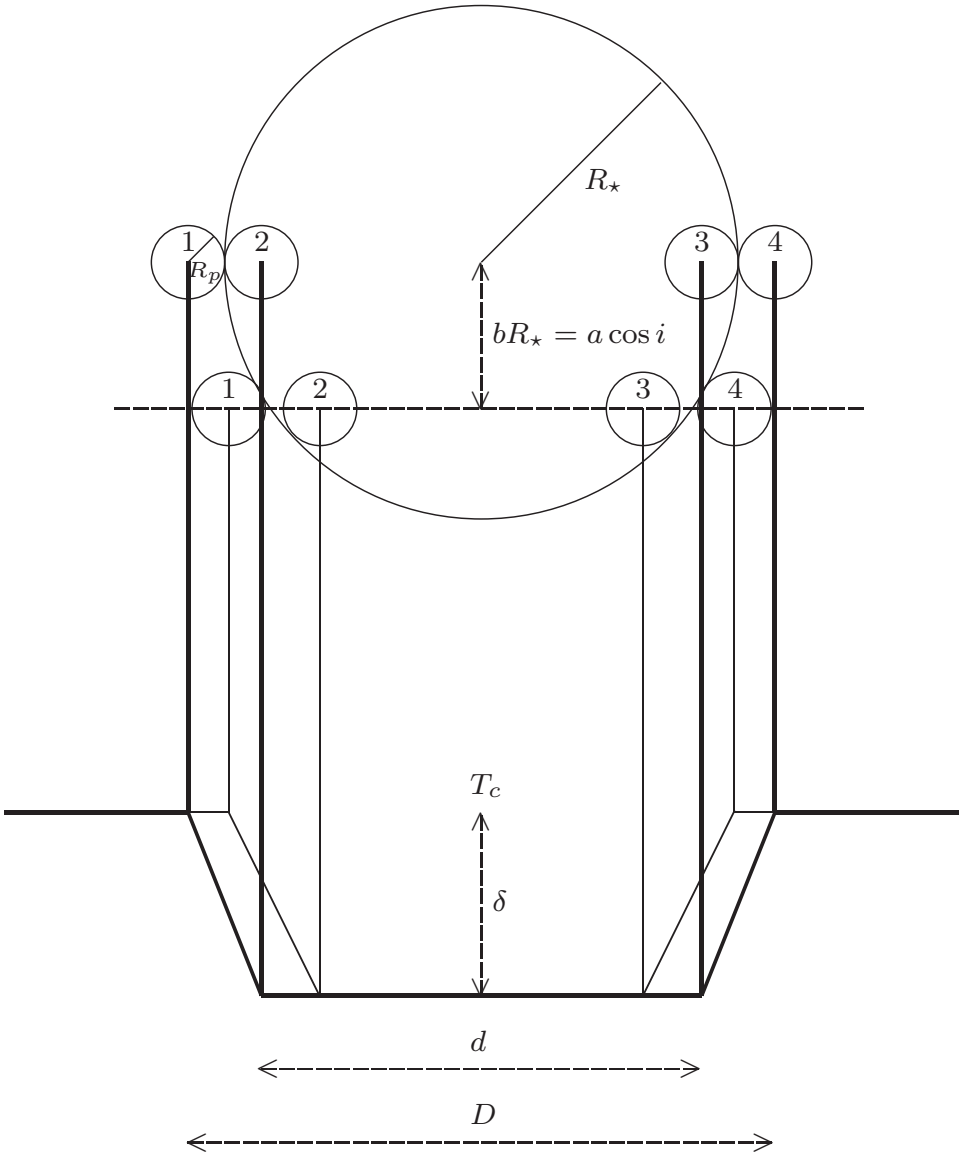

Figure 5: Transit light-curve parameters. For the corresponding geometry of the star and the planet shown on the top, two schematic light curves are shown on the bottom (thin and thick solid lines). For a planet moving from left to right, first, second, third, and fourth contacts are indicated with numbers. Displayed for the thick solid light curve are the transit depth, δ, the full duration of the transit, D, and the duration of totality, d. Also defined are planetary and stellar radius, R_p and $R_\star$, respectively, and impact parameter, b. Different impact parameters result in different transit shapes, as shown for two planet-star geometries.

However, systematic errors present in data or insufficient data accuracy can lead to a fundamental degeneracy between the parameters R_p, $R_\star$ and i. While the planet and stellar radii can be reduced to preserve the transit depth, the orbital inclination can be correspondingly increased to preserve the chord length across the star. To overcome this degeneracy high-accurate transit light curve or a good estimate of $R_\star$ is needed.

Transiting planets are uncommon; assuming a random orientation of planetary orbits, the probability, P_{tr}, that a planet with orbital eccentricity, e, and longitude of periastron, ω, produces transits visible from the Earth was given by Charbonneau et al. (2007) as follows:

$$P_{tr} = 0.0045 \left(\frac{1 \text{ AU}}{a}\right) \left(\frac{R_\star + R_p}{R_\odot}\right) \left[\frac{1 + e\cos\left(\frac{\pi}{2} - \omega\right)}{1 - e^2}\right], \tag{5}$$

which is inversely proportional to a. Therefore, 'hot Jupiters' have higher probability of transits visible from the Earth than the same mass planets on wider orbits, thus almost all of the known transiting planets to date are 'hot Jupiters'.

Among about 60 known transiting planets to date only a few least massive have masses similar to smaller giant planets in the Solar system. The least massive transiting planets discovered to date are the super-Earth mass planet CoRoT-7 b (Leger et al., 2009), then two Neptun-mass planets GJ 436 b (Gillon et al., 2007) and HAT-P-11 b (Bakos et al., 2009) and the Saturn-mass planet HAT-P-12 b (Hartman et al., 2009). The known transiting planets have radii 5 – 17 % of stellar radii, which leads to 0.3 – 3.0 % diminution of the stellar flux detected on the Earth. These transits last for 1 – 4 hours. The only exception is the recently discovered transiting planet HD 80606b known before from RV searches that transits in front of its parent star for 11.64 ± 0.25 hours (Winn et al., 2009a).

2.3.2 Detection methods

All transiting planets discovered to date have been detected either photometrically, with a subsequent confirmation of planetary mass via RV measurements, or by RV-detection of a planet with a subsequent discovery of photometric transits. The latter has the advantage that the planetary nature is immediately obvious, however, a considerable observing time on large telescopes is needed to identify each system. In contrast, transit searches monitor simultaneously fluxes of a large number of stars followed by search for photometric transits. Nevertheless, a substantial number of detections turns out to be astrophysical false alarms, results from transits of binary or multi-star systems. For example, an M-dwarf star eclipsing a main-sequence F star produces flat-bottomed transit with the duration and depth as for a transiting planetary system. However, already from low-precision spectra it is possible to distinguish between the planetary and stellar companion.

Most of the transiting planets have been discovered by small-aperture, wide-field photometric surveys. Among the most successful are the Wide Angle Search for Planets – SuperWASP (Pollacco et al., 2006), the Hungarian Automated Telescope Network – HAT (Bakos et al., 2004), XO (McCullough et al., 2005) and the Transatlantic Exoplanet Sur-

vey – TrES (Dunham et al., 2004). They typically monitor simultaneously a few hundred thousand of stars every night and use automatic procedures to detect transit events.

Nearly ten transiting planets have been detected by the Optical Gravitational Lensing Experiment (OGLE) survey (Udalski et al., 2002), which uses a 1.3-m telescope. The parent stars of these planets are usually faint (typically $V = 16$) and large telescopes are needed for follow-up RV measurements.

Recently, the number of transiting planets increased due to the successful space mission Convection, Rotation and Transits (CoRoT), that announced the detection of seven transiting planets to date. In a near future also transiting Super-Earth and Earth-mass planets are expected to be discovered with the Kepler spacecraft launched in March 2009.

2.3.3 The Rossiter-McLaughlin effect

A transiting system can be further characterized from high-resolution stellar spectra obtained during primary transits. As the planet passes in front of the star, the part of the rotating stellar disk is occulted which results in a characteristic time-dependent shift of the photospheric line profiles. The feature is known as the Rossiter-McLaughlin (RM) effect (McLaughlin, 1924; Rossiter, 1924) and was first observed in the spectra of eclipsing binaries. From a characteristic RV-curve distortion one can determine the angle between sky projections of the planet orbital axis and the stellar spin axis, λ (see Fig. 6). This has a great impact on theories of planet migration as different migration scenarios predict different λ. Whereas migration via tidal interactions with a protoplanetary disk is expected to result in a close spin-orbit alignment (Ward & Hahn, 2003), migration due to planet-planet scattering would magnify any initial misalignments (Chatterjee et al., 2008) and migration via Kozai cycles accompanied by tidal friction would produce a broad distribution of final inclination angles (Fabrycky & Tremaine, 2007).

However, observations of the RM effect provide only a lower limit on the spin-orbit alignment, λ, because it is the angle between sky projections of the orbital and rotation axis and inclinations with respect to the sky need to be determined with some other method. The orbital inclination is usually well known from a transit light curve, but the stellar spin axis inclination, $i_\star$, is generally unknown. However, if a parent star is chromospherically active and exhibits quasiperiodic flux variations, the rotational period, P_{rot}, can be determined. Using the stellar radius, $R_\star$, and a projected star rotation rate, $v \sin i_\star$, measured either from the observed spectral line broadening or from the amplitude of the RM effect, we can determine the unknown angle $i_\star$:

$$\sin i_\star = \frac{P_{rot} v \sin i_\star}{2\pi R_\star}. \tag{6}$$

The spin-orbit alignment λ was examined so far for 16 transiting exoplanet systems. They all were found to have a close spin-orbit alignment with few exceptions. One exception was the system HD 17156, for which Narita et al. (2008) measured $\lambda = 62 \pm 25$ deg, but Cochran et al. (2008) published measurements based on follow up data and found $\lambda = 9.4 \pm 9.3$ deg. Later Narita et al. (2009a) superseded the previous claim and published

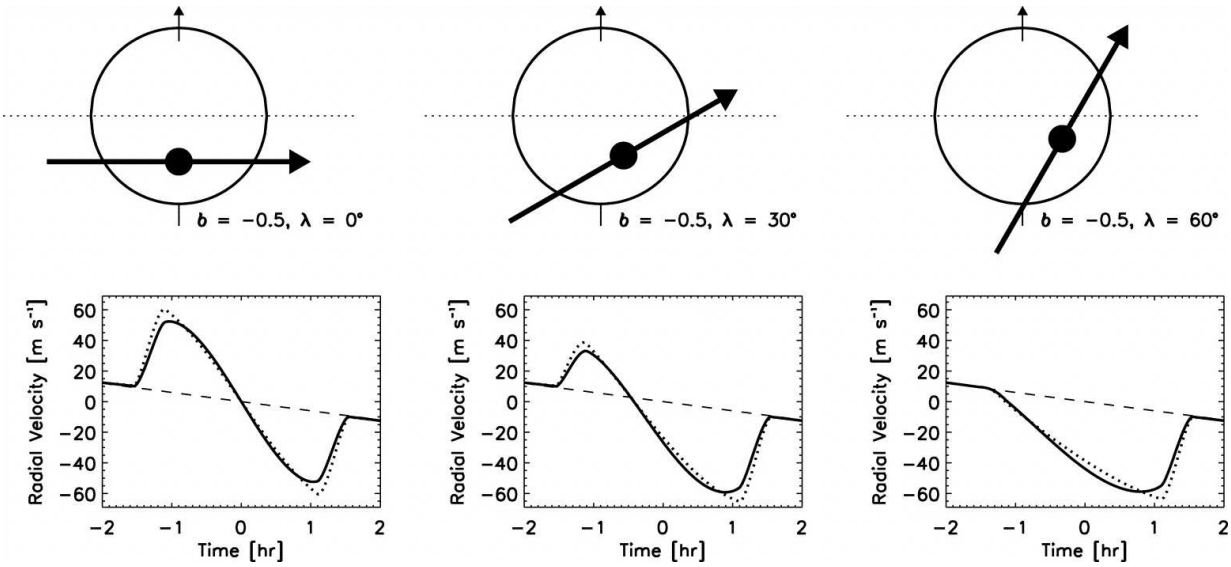

Figure 6: Three different cases of possible trajectories of a transiting planet are shown, with the corresponding RV-curve distortion. All trajectories have the same impact parameter and result in the same light curve, but they differ in λ, the angle between sky projections of the planet orbital axis and the stellar spin axis, and produce different RM waveform. The dotted line is for the case of no limb darkening ($\epsilon = 0$), the solid line is for $\epsilon = 0.6$. Adopted from Gaudi & Winn (2007).

a new value $\lambda = 10.0 \pm 5.1$ deg. The other exception is the system XO-3, for which two different values of λ were published. First, using SOPHIE spectrograph at the 1.93-m telescope of Haute-Provence Observatory Hébrard et al. (2008) measured $\lambda = 70 \pm 15$ deg, but cautioned that additional data were needed to exclude possible systematic errors in their measurements. Secondly, Winn et al. (2009c) published the value $\lambda = 37.3 \pm 3.7$ deg, based on measurements from HIRES spectrograph on 10-m Keck telescope. The spin-orbit misalignment was also published for the HD 80606 system (Gillon, 2009; Pont et al., 2009; Winn et al., 2009a) and the WASP-14 system (Johnson et al., 2009). All three exoplanetary systems with known spin-orbit misalignment have massive planets on eccentric orbits, which could be a consequence of a different migration mechanism than for lower-mass planets on circular orbits. In addition, the WASP-17 and HAT-P-7 systems were found to have planets on retrograde orbits (Anderson et al., 2009; Narita et al., 2009b; Winn et al., 2009b), suggesting that there indeed exist distinct modes of planetary migration.

2.3.4 Transit timing variations

Most of the exoplanets detected to date are of Jupiter mass, and neither ground-based photometric nor RV surveys have reached the accuracy needed to find Earth-mass planets. However, a chance to detect Earth-mass planets exists via detection of transit timing variations (TTVs) in the known transiting exoplanet systems. Namely, an additional planet in the transiting system will perturb the motion of the transiting planet, and the interval between the mid-eclipses will not be constant. Deviations from the predicted mid-

transit times can therefore reveal a presence of other bodies in the system, or place limits on their existence. Short-term variations can reveal the existence of other planets (Agol et al., 2005; Holman & Murray, 2005), moons (Sartoretti & Schneider, 1999; Kipping, 2009) and also Trojans (Ford & Holman, 2007), whereas long-term variations can result from orbital precession induced by another planet (Miralda-Escudé, 2002; Heyl & Gladman, 2007). Discovery of additional bodies further constrains theories of planetary system formation and evolution.

Several groups investigated how parameters of the perturbing planet can be determined from observed TTVs. Agol et al. (2005), Holman & Murray (2005) and Steffen (2006) used direct N-body integrations of a large sample of planetary systems to fit the observed TTV signal. However, this approach is computationally time consuming due to the high number of unknown parameters. Nesvorný & Morbidelli (2008) suggested an alternative method to solve for possible TTVs based on analytic perturbation theory. They calculate transit times as a sum over Fourier terms with amplitudes and phases that are explicit functions of the unknown parameters. The tests showed their approach is $\sim 10^4$ times faster than direct orbital integrations, but it is not suitable for systems where planets are in mean motion resonances. However, in the resonant cases Nesvorný & Morbidelli (2008) suggested to separate first the long-period term, then model the residual short-period signal using the perturbation theory method as in the nonresonant cases, and finally verify that identified solutions match both the short- and long-period TTVs.

Ford & Holman (2007) explored how to use TTVs to search for Trojans of transiting extrasolar planets. Trojans are bodies librating around the Lagrange points L4 or L5 of the planet that lead/trail the planet by $\simeq 60$ deg. If there are no other massive bodies in the system, then the L4/L5 fixed points are stable for circular orbits if the ratio, $\mu = (M_p + M_T)/(M_\star + M_p + M_T)$, where M_T is Trojan's mass, is less than a critical value, μ_c, where $0.03812 \leq \mu_c \leq 0.03852$ (Laughlin & Chambers, 2002). Transit times are the same for a system without a Trojan and for a system where the transiting planet and Trojan have equal eccentricities and the Trojan resides exactly at the Lagrange L4/L5 fixed point. Unless a clear variation is found, TTV analysis alone is not suitable for constraining the presence of Trojans in transiting systems. In this case, the better approach is to compare the photometrically observed transit time and the transit time calculated from the RV data assuming zero Trojan mass, which can reveal a Trojan or place upper limits on its mass (Ford & Gaudi, 2006b). In case there is a clear TTV caused by a Trojan body, according to Ford & Holman (2007) the variations would change on the secular timescale with a libration period $P_{lib} \simeq P(4/27)^{1/2}\mu^{-1/2}$ (Murray & Dermott, 2000), and most probably would have large amplitudes. TTVs caused by exomoons would have shorter periods due to a dynamical stability of such systems, and TTVs caused by other planets would have lower amplitudes unless the perturbing planet is massive and would have been detected from RV measurements.

The transit timing effect due to exomoons was explored by several different authors (Sartoretti & Schneider, 1999; Szabó et al., 2006; Simon et al., 2007). Recently, Kipping (2009) upgraded previous models including orbital eccentricity and introducing a new observable due to exomoons – the transit duration variation (TDV). According to Kipping

(2009) the orbital radius of a satellite must lie between the Hill radius, d_{max}, and the Roche limit, d_{min}, in order to maintain a stability. He estimated that the ratio of satellite to planet orbital period is:

$$\frac{P_s}{P} \simeq \sqrt{\frac{\chi^3}{3}}, \tag{7}$$

where χ is some fraction of the Hill radius, d_{max}, and therefore $\chi \leq 1$ and $P_s < P$. Assuming $\chi \sim 1/3$ (Barnes & O'Brien, 2002) gives a rough estimate of $P_s/P \sim 1/9$ and so the orbital frequency of the exomoon will always be higher than the sampling frequency and the period of the exomoon cannot be reliably determined from TTVs solely.

As already pointed out by Sartoretti & Schneider (1999), the TTV amplitude is $\propto M_s a_s$, where M_s and a_s are satellite's mass and orbital semimajor axis, respectively. The problem is that the mass cannot be determined without making an assumption on the distance at which the exomoon orbits the planet, and the period of the exomoon is not reliably determined from TTVs.

Kipping (2009) solved this problem by introducing the new observable, TDV. He showed that the TDV amplitude is $\propto M_s a_s^{-1/2}$, and therefore the ratio of TDV to TTV allows to determine M_s and a_s. Another benefit is that TDV has a $\pi/2$ phase difference to TTV signal, and thus is a complementary technique. In addition, Kipping (2009) derived that increasing the eccentricity of the exomoon's orbit decreases TTV amplitude, but increases TDV amplitude. He also derived TTV and TDV amplitudes predicted for a variety of known transiting systems, caused by an Earth-mass exomoon in a circular orbit about the transiting planet.

To date only a few studies provide evidence of TTV. Díaz et al. (2008) found TTVs for the transiting system OGLE-TR-111, suggesting a presence of an Earth-mass planet in an exterior orbit to the transiting planet, if the orbit of OGLE-TR-111b is eccentric. The eccentricity needed to explain the observations is not ruled out by the current RV data. Other evidence of TTV was found by Welsh (2009) for the HD 17156 transiting system suggesting the presence of a third body. Both discoveries originate from ground-based observations.

On the other hand, so far no significant TTVs has been found from space observations. Instead, strong limits were placed on the presence of other bodies in transiting extrasolar systems HD 209458 (Miller-Ricci et al., 2008a), HD 189733 (Miller-Ricci et al., 2008b) and CoRoT-2 (Alonso et al., 2009). In a near future, accurate long-time photometry of transiting extrasolar systems suitable for TTV analyses should be provided by CoRoT and Kepler space missions.

2.3.5 Planetary atmospheres

There are two main approaches how to study planetary atmospheres of transiting extrasolar planets. First is the transmission spectroscopy technique, where stellar spectra obtained during a primary transit, when a planet is transiting in front of its parent star, are divided by spectra taken just before or after a primary transit, the latter providing spectra of an

isolated star. The thin planetary atmosphere surrounding the optically thick planet disk and absorbing part of a star light can thus be indirectly observed. Second approach is the secondary transit technique, where we seek the difference between a combined spectrum of a star and a planet, and a stellar spectrum alone when a planet is hidden by stellar disk.

The transmission spectroscopy was first theoretically proposed by Seager & Sasselov (2000), and experimentally confirmed by Charbonneau et al. (2002), who observed sodium in the atmosphere of the transiting planet HD 209458b. With this technique, astronomers can learn about atomic and molecular abundances, but less about temperature variations in the planetary atmosphere.

Secondary transits of two 'hot Jupiters', TrES-1b and HD 209458b, were first observed by Charbonneau et al. (2005) and Deming et al. (2005), respectively, using the Spitzer Space Telescope in the infrared spectral range, where the ratio of the planet to star flux is the largest. Photons that are directly emitted or reflected by the planet are observed, which allows detecting molecular species, but also constraining the temperature and vertical thermal gradients. In the optical spectral range the planetary albedo can be measured.

Another way how to access temperature and albedo variations is to observe a light curve of a combined star-planet flux during the whole planetary orbit. However, this is feasible only with space-based telescopes.

Due to the Spitzer Space Telescope and the Hubble Space Telescope (HST) it was possible to explore extrasolar planetary atmospheres. However, a secondary transit in the near infrared was also observed from the ground (de Mooij & Snellen, 2009; Sing & López-Morales, 2009).

Very similar temperatures on the day and night sides were observed for some transiting extrasolar planets, while for others the opposite was true. A thermal inversion layer high in the atmosphere was detected for some of them, but not for others. It became obvious that at least two different classes of 'hot-Jupiter' atmospheres are observed. The explanation was given by Fortney et al. (2008). They suggested that the so called 'pM Class' planets that are warmer than required for condensation of TiO and VO will have an inversion layer at low pressure caused by the absorption of incident flux by these molecules. On the other hand, 'pL Class' planets have temperatures below the condensation temperature of Ti and V bearing compounds and alkalis become important optical absorbers. They have smaller day/night temperature differences and better energy redistribution.

2.3.6 Statistical properties

Transiting extrasolar planets are the only ones for which we know their masses and radii. Exploring their properties can thus reveal new interesting characteristics that are unavailable for the whole exoplanet sample. Interesting trends between planetary mass or gravity and orbital period for the known transiting planets were published by Mazeh et al. (2005) and Southworth et al. (2007). Two classes of 'hot Jupiters' were identified by Hansen & Barman (2007), based on their equilibrium temperatures and Safronov numbers which essentially measure how efficiently a planet scatters other bodies. We discovered an interesting correlation between the planetary radius and stellar metallicity, as shown in Fig. 7.

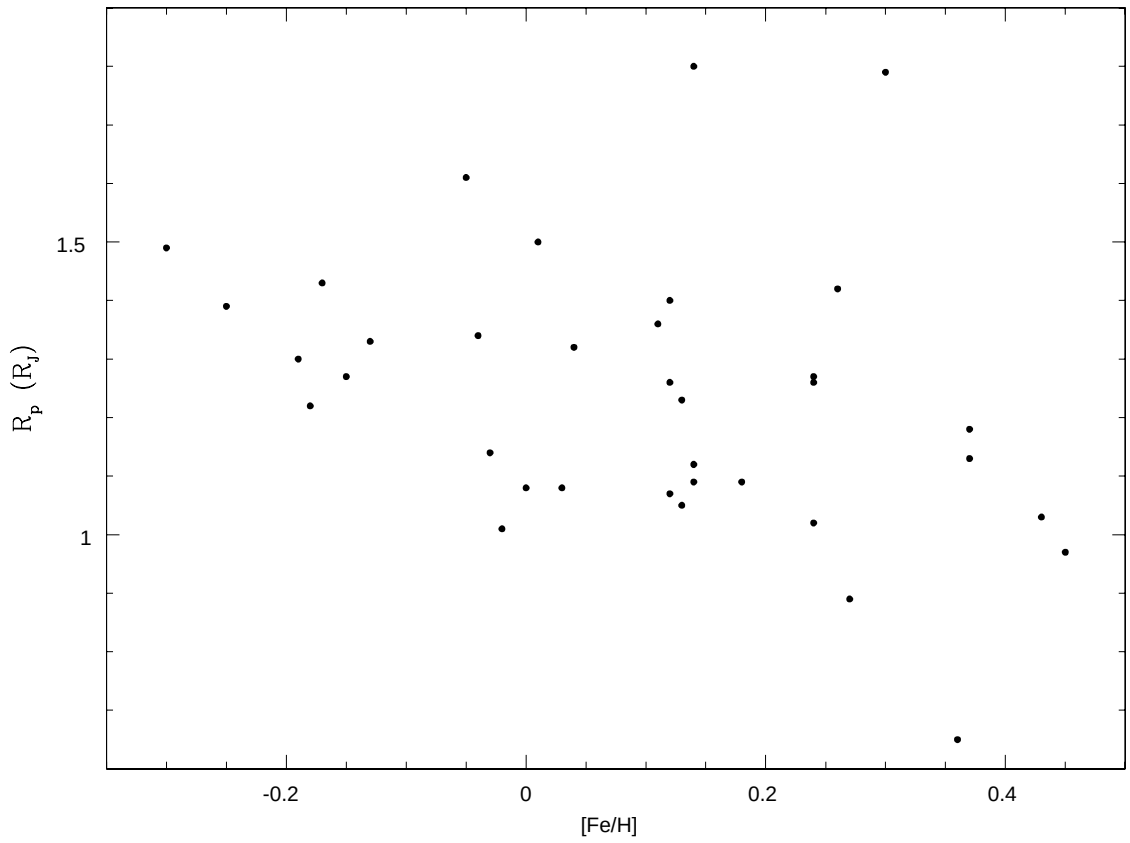

Figure 7: The correlation between the planetary radius and stellar metallicity reveals that stars with lower metallicities host planets with larger radii. Data were taken from J. Schneider's Extrasolar Planets Encyclopaedia. We included all transiting extrasolar planets of 'hot Jupiter' type for which the corresponding quantities are known.

Stars with lower metallicities host planets with larger radii, whereas the planetary mass remains constant. This might be a consequence of planetary formation and evolution processes. However, new discoveries are needed to show if these correlations are still valid with a larger sample of transiting exoplanets.

2.4 Radial-velocity measurements

If a planet is present in a system, a parent star will exhibit periodic RV changes due to its orbital motion about a common centre of gravity with the semi-amplitude, K, that is proportional to the minimum planet mass, $M_p \sin i$, and inversely proportional to the

planet period, P, its eccentricity, e, and the stellar mass, $M_\star$:

$$K = \left(\frac{2\pi G}{P}\right)^{1/3} \frac{M_p \sin i}{(M_p + M_*)^{2/3}} \frac{1}{(1-e^2)^{1/2}}. \quad (8)$$

The closer or more massive the planet, the larger the semi-amplitude of the RV variation. As only the velocity of a star along the line of sight is measured, we only have access to a minimum planet mass. In the Solar system, Jupiter causes RV changes of the Sun with the semi-amplitude $K = 12.5\ \mathrm{m\,s^{-1}}$, and the Earth only with the semi-amplitude $K = 0.1\ \mathrm{m\,s^{-1}}$. Therefore, to detect Earth-mass planets in habitable zones, very accurate RV measurements are essential.

To date, the most accurate instrument for RV measurements is the European Southern Observatory's (ESO's) spectrograph High Accuracy Radial velocity Planetary Search (HARPS) on the 3.6-m telescope at La Silla Observatory that became operational in 2003 (Pepe et al., 2003). It is a fibre–fed, cross–dispersed echelle spectrograph with two fibres, an object and a reference fibre, that feed the spectrograph with the light coming from the telescope and the calibration lamps. The fibres are reimaged by the spectrograph optics onto a mosaic of two CCDs, where two echelle spectra of 72 orders are formed for each fibre. The main characteristics of HARPS are its outstanding efficiency, spectral resolution of R=115,000 and its extraordinary stability. The stability is achieved by using the simultaneous ThAr-reference technique, and a strict pressure and temperature control. Since ambient pressure variations would produce drifts of the spectrograph, it operates in vacuum.

The HARPS spectrograph offers two options for accurate wavelength calibration: the default simultaneous ThAr-reference method and the use of the iodine absorption cell. When using the ThAr-reference method thorium and argon calibration lamps feed one fibre while object is observed with another fibre. This technique is able to track instrumental drifts at a level of $0.1\ \mathrm{m\,s^{-1}}$ rms. The latter method, based on a use of a iodine absorption cell, was first proposed by Marcy & Butler (1992) and Valenti et al. (1995). The superimposed iodine lines provide a highly accurate wavelength scale and the spectrograph point spread function (PSF) in situ over the entire echelle format. However, when a stellar spectrum is superimposed with iodine absorption features, a mean throughput is only about 50 % in average (Pepe et al., 2003). Therefore the ThAr-reference technique is more efficient and is highly preferred for the extrasolar planet searches with HARPS.

Until recently, the Doppler technique was thought to have reached its final limitations in measuring RVs and finding extrasolar planets. The intrinsic stellar variations were believed to be limiting the accuracy of RV measurements to $\sim 1\ \mathrm{m\,s^{-1}}$. However, HARPS demonstrated that stars with the intrinsic variability $< 1\ \mathrm{m\,s^{-1}}$ exist, and that their RVs can be measured at that level of accuracy. On real stars HARPS achieved short-term accuracy (one night) of 20 $\mathrm{cm\,s^{-1}}$ and long-term accuracy (years) of the order of $30 - 60\ \mathrm{cm\,s^{-1}}$, showing that RV method has still a great potential for the future (Pepe & Lovis, 2008).

Even better RV accuracy will be achieved with the new method using a single frequency source for a wavelength calibration. The method called 'astro-comb' is using an optically

filtered comb of evenly spaced frequency references, derived from a pulsed laser. In 2005 the Nobel Prize in physics was awarded for the idea, and the first application to astronomy was presented by Murphy et al. (2007). Laser frequency combs have good long-term stability, reproducibility and useful lines in the red to near-infrared range. Recent studies show that combining a laser frequency comb with a Fabry-Perot filtering cavity enables long-term RV accuracies of the order of 5 $\mathrm{cm\,s^{-1}}$, which could allow discoveries of Earth-mass planets in exoplanetary systems (Li et al., 2008; Walker, 2008). Such a calibration technique is expected to be deployed at the High Accuracy Radial velocity Planet Searcher of the New Earths Facility (HARPS-NEF) spectrograph in 2010 at the William Herschel Telescope on La Palma.

2.5 Other detection methods

Different detection methods allow discoveries of planets with variety of characteristics due to the fact that each method is sensitive differently to distinct planetary parameters. We discuss briefly detection methods other than RV measurements and photometric detections of transits in this section.

2.5.1 Direct imaging

The planets are detected directly using this method via special imaging techniques. The ratio of a planet to star flux given by Charbonneau & Noyes (2000b) is:

$$f_\lambda(\alpha) = p_\lambda \left(\frac{R_p}{a}\right)^2 \Phi_\lambda(\alpha), \tag{9}$$

where p_λ is the wavelength-dependent geometric albedo and $\Phi_\lambda(\alpha)$ is the phase function, for which by definition $\Phi_\lambda(0) = 1$. Scaling Eq. (9), Charbonneau & Noyes (2000b) found:

$$f_\lambda(\alpha) \simeq 9.1 \times 10^{-5} p_\lambda \left(\frac{R_p}{R_J}\right)^2 \left(\frac{0.05\ \mathrm{AU}}{a}\right)^2 \Phi_\lambda(\alpha). \tag{10}$$

The Jupiter/Sun reflected-light ratio in the V band viewed at opposition would be $f \simeq 4 \times 10^{-9}$. This ratio dramatically increases for 'hot Jupiters', due to their small semimajor axis. In addition, in a near-infrared or infrared band a planet has the maximum of its own radiation, and so the ratio of a planet to star flux is the highest.

To detect a faint planet light (reflected or emitted) requires special techniques. One possibility is the adaptive optics on ground-based telescopes where a wavefront of a natural or laser guide star's light is measured to correct an image blurring introduced by the Earth's atmosphere. Bracewell & MacPhie (1979) proposed the nulling interferometry technique where the planetary radiation relative to that from the star is enhanced by placing a null of an interference pattern on the star. Technique of the angular differential imaging is another high-contrast imaging method that reduces quasistatic speckle noise and facilitates

detections of nearby companions. Details can be found in Marois et al. (2006) or Lafrenière et al. (2007).

Recently, in three systems planets were detected using imaging methods. Smith & Terrile (1984) discovered a dusty disk by β Pic, and Lagrange et al. (2009) announced a probable giant planet resolved in this disk. Kalas et al. (2009) published a discovery of a debris disk and a planet by Fomalhaut and Marois et al. (2008) discovered three planets orbiting the star HR 8799 (see Fig. 8). This technique is capable to discover giant planets with large orbital separations, and thus is complementary to RV and photometric searches.

2.5.2 Gravitational microlensing

The effect of a gravitational lens occurs when background and foreground source objects are aligned. In case of a gravitational microlensing background source stars serve as a light source used to probe a gravitational field of foreground stars and any planets they host. This idea was first proposed by Einstein (1936). Due to a relative motion of source and lens objects a source magnification changes with time and thus a gravitational field of a foreground object can be explored.

A probability of a lens event is only $\sim 10^{-6}$ for background stars in the Galactic bulge, and therefore fluxes of millions of stars have to be observed every night in order to detect such events. There are several projects; two of them contributed with extrasolar planet detections – OGLE (Udalski et al., 2002) and the Microlensing Observations in Astrophysics (MOA) (Bennett et al., 2008; Dong et al., 2009).

Microlensing is a promising technique with a potential of detecting sub-Earth mass planets on long-period orbits, and thus is complementary to all the other detection methods.

2.5.3 Astrometric method

A planet can be deduced from changes of accurately measured star positions. This method is sensitive to longer-period systems and planets around targets not accessible with RV surveys, like A or B stars, can be found.

The only astrometric space mission to date, Hipparcos, reached accuracies of 1 mas[2] and provided upper mass constraints on several known extrasolar planets. However, for a long time, there was no planet detected by astrometric method. Only recently Pravdo & Shaklan (2009) announced a probable first astrometric discovery of an extrasolar giant planet around a main-sequence star with a mass near the lower limit for a star. They estimated the planetary mass $M_p = 6.4^{+2.6}_{-3.1}$ M_J and the period $P = 0.744^{+0.013}_{-0.008}$ years. Nevertheless, the accuracy of astrometric measurements needed to easily detect extrasolar planets is still not sufficient. Space missions like Gaia with expected accuracy of 1 μas[3] and a planned launch in 2011 should change the situation. The only remaining problem might

[2]The milliarcsecond, abbreviated mas, is a unit of angular measurement, equal to 1/1,296,000,000 of a unit circle.

[3]The microarcsecond is a unit of angular measurement, equal to 1/1,000 of 1 mas.

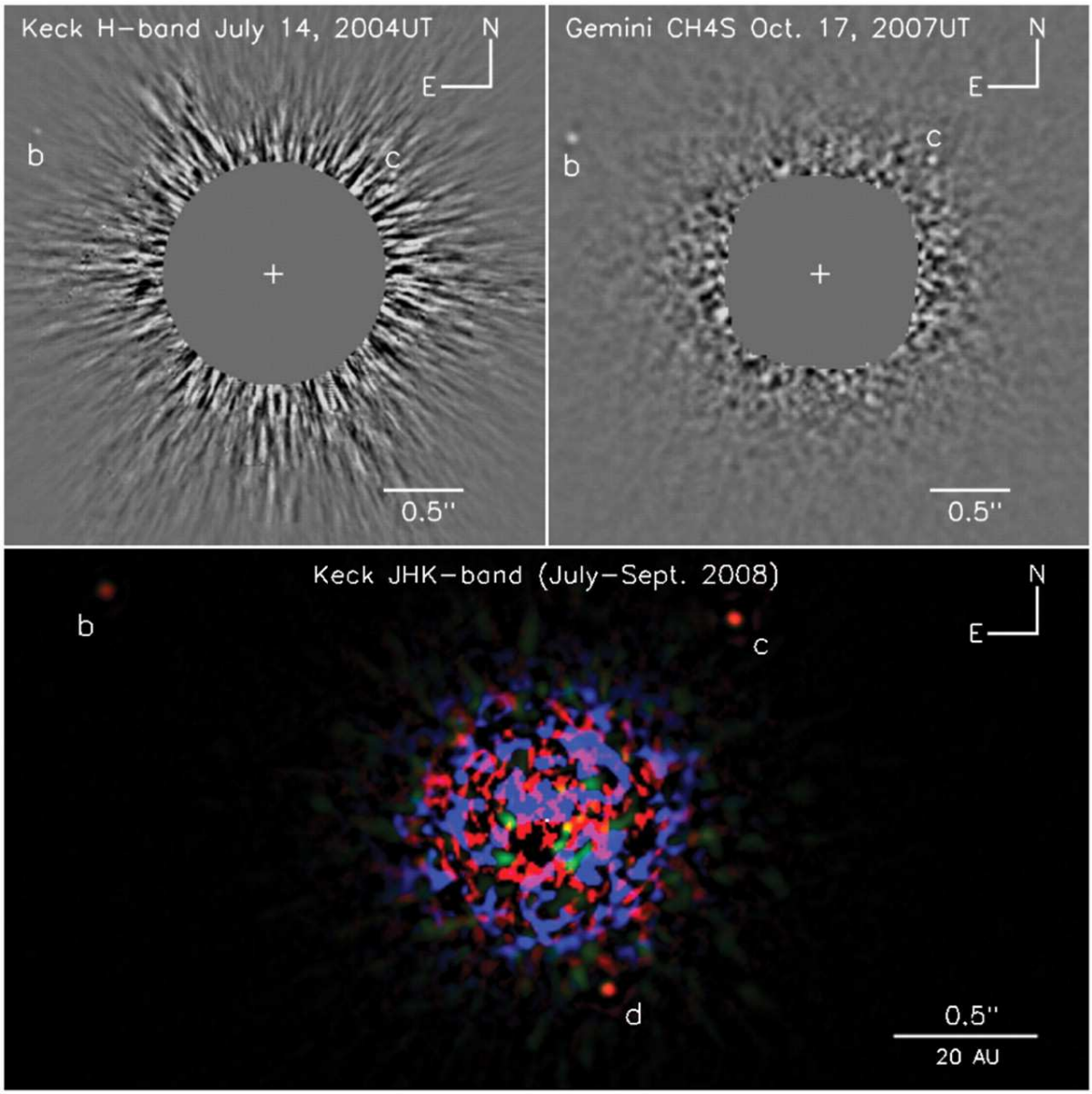

Figure 8: The discovery images of the HR 8799 planetary system after the light from the bright host star has been removed by angular differential imaging technique. Upper left: A Keck image acquired in July 2004. Upper right: Gemini discovery image from October 2007. Both planets b and c are detected at the two epochs. Bottom: A colour image of the planetary system produced by combining the J-, H-, and Ks-band images obtained at the Keck telescope in July (H) and September (J and Ks) 2008. The inner part of the H-band image has been rotated by 1 deg to compensate for the orbital motion of the planet d between July and September. The central region is masked out in the upper images but left unmasked in the lower to clearly show the speckle noise level near the planet d. Adopted from Marois et al. (2008).

be luminous inhomogeneities of a stellar disk causing apparent shifts of a light source, thus complicating the planet detections.

2.5.4 Planets by pulsars

Planets by pulsars, fast rotating neutron stars, can be revealed via changes of the pulsar signal arrival caused by a light-time effect due to a companion planet. The pulsar signal is emitted parallel to the magnetic axis and signal changes can be detected because the rotational and magnetic axis are not aligned. Normal pulsars have periods around 1 second, but millisecond pulsars rotate fast due to a material coming from their binary companion. The high accuracy of a signal timing allows detection of sub-Earth mass planets, or even moons and asteroids, in such systems. To date four planetary systems are known by pulsars, and the least massive planet PSR 1257+12b with a mass 0.02 $M_{\oplus}$ was found via pulsar timing measurements.

However, the origin of planets by pulsars is unknown. One possibility is that planets formed in original protoplanetary disk and survived the giant explosion. In binary pulsars, other explanation could be that planets were captured later by gravitational forces of pulsar, or created from the accretion disk.

3 BARCOR

To detect changes of tens $\mathrm{m\,s^{-1}}$ or even smaller in the RV curves high-quality observations and accurate barycentric RV corrections are needed. At the moment of a star-light arrival to the observer the Earth orbits the Sun and rotates around its axis, therefore the corrections for these movements has to be done. Simply, the observed RV is corrected for the motion of the observer in the direction of observation. Besides, also the time of the light arrival has to be related to the barycentre of the Solar system.

In 2006 the program BARCOR for computations of barycentric RV and time corrections written in Fortran 77 was finished. The program uses as an input positions and velocities of the Earth obtained from the JPL Planetary and Lunar Ephemerides DE405 (Standish, 1998a,b). For the given Julian Ephemeris Date (JED) positions and velocities are computed by differentiation and interpolation of a set of Chebyshev coefficients. Both positions and velocities are rectangular and are related to the Earth Mean-equator and dynamical equinox of the epoch J2000.0 of inertial reference frame. 'Mean' indicates that the effects of nutation are ignored in the definition of the reference frame. The orientation of the inner planet system of DE405 onto the International Celestial Reference Frame (ICRF) is accurately determined mainly by the VLBI observations. Compared to the origin of ICRF it is believed that the orientation of the whole inner planet ephemeris system of DE405 is accurate to about 0.001 arcseconds. On the other hand, ephemerides of the outer planets rely almost entirely upon optical observations.

The program BARCOR with some examples of input and output files is available online at http://sirrah.troja.mff.cuni.cz/~mary. The underlying physics is explained in the following sections.

3.1 The Earth flattening

The Earth is slightly flattened due to the rotation. The exact shape is complicated, but for most purposes it can be approximated by an oblate spheroid. In BARCOR the reference spheroid defined by the World Geodetic System WGS-84 is used. The equatorial radius, a, is defined as $a = 6378137.0$ m. The Earth's polar radius, b, is related to the equatorial radius by the term called Earth flattening, f:

$$f = \frac{a - b}{a}. \tag{11}$$

In WGS-84 the flattening is 1/298.257223563, which is a very small deviation from a perfect sphere. Using this value, the Earth's polar radius would be $b = 6356752.3142$ m.

It is convenient to define few terms shown in Fig. 9. The local horizon is a plane which is tangent to the Earth's surface at the observer's position. In the direction from the Earth's centre perpendicular to the local horizon at the observer's position is the local zenith. On the sphere, this direction is always directly away from the Earth's centre, however on the oblate spheroid the flowline of the Earth's centre and the observer's position would not point, except of the equator and the poles, to the local zenith. The geodetic latitude, ϕ, is

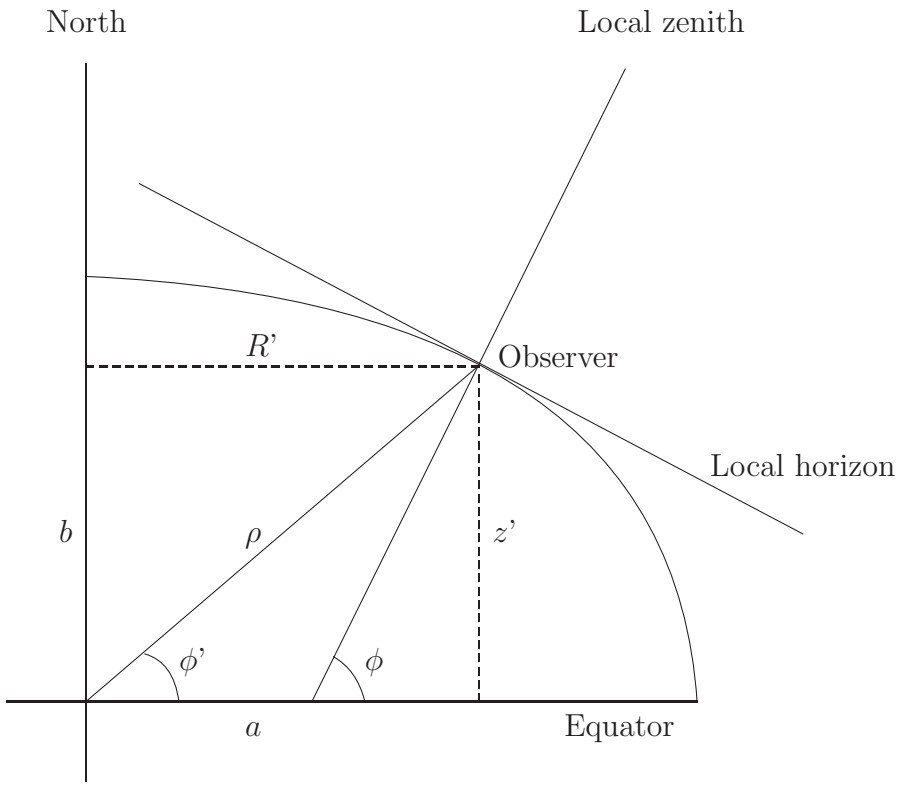

Figure 9: The cross-section of the oblate Earth, where the oblateness is exaggerated for clarity. ϕ and ϕ' is the geodetic and geocentric latitude, respectively, a is the equatorial and b is the polar radius, and ρ is the radius at the observer's place.

the angle between the local zenith direction and the Earth's equatorial plane. This angle is the latitude used on maps and sometimes is also called the geographic latitude. The geocentric latitude, $\phi^{'}$, is the angle between the line connecting the observer's position, the Earth's centre and the equatorial plane. The geocentric radius, ρ, is a distance of the observer from the Earth's centre.

The observer's coordinates are normally given in the geodetic latitude, ϕ, and we need to compute geocentric latitude, $\phi^{'}$, for the BARCOR usage. The conversion can be carried out using following expressions. The basic definition of an ellipse is:

$$\frac{(R^{'})^2}{a^2} + \frac{(z^{'})^2}{b^2} = 1, \tag{12}$$

where

$$R^{'} = \rho \cos \phi^{'} \tag{13}$$

and

$$z^{'} = \rho \sin \phi^{'}. \tag{14}$$

It is clear that

$$\tan \phi^{'} = \frac{z^{'}}{R^{'}}. \tag{15}$$

The direction of the normal to the ellipse is given by

$$\tan \phi = -\frac{dR^{'}}{dz^{'}}. \tag{16}$$

After differentiating the equation of the ellipse, we get:

$$\frac{2R^{'}dR^{'}}{a^2} + \frac{2z^{'}dz^{'}}{b^2} = 0 \tag{17}$$

and after rearranging the terms:

$$\frac{z^{'}}{R^{'}} = -\frac{b^2}{a^2}\frac{dR^{'}}{dz^{'}}, \tag{18}$$

which can be written as:

$$\tan \phi^{'} = \frac{b^2}{a^2} \tan \phi = (1-f)^2 \tan \phi = (1-e^2) \tan \phi, \tag{19}$$

where e is the eccentricity of the ellipse and $e^2 = 0.006694 = 2f - f^2$.

Now we have the geocentric latitude, but in fact we need to compute $R^{'}$ in terms of the angle ϕ. It can be shown that:

$$R^{'} = \rho \cos \phi^{'} = \frac{a \cos \phi}{\sqrt{1 - e^2 \sin^2 \phi}}, \tag{20}$$

where the term $1/\sqrt{1 - e^2 \sin^2 \phi}$ is the effect of the Earth flattening.

Karttunen (2003) indicates that the shape defined by the surface of the oceans, called the geoid, differs from the spheroid by at most 100 m and that the difference $\phi - \phi^{'}$ has a maximum value $11\farcm5$ at the latitude 45°. The maximum error resulting from omitting the Earth flattening in the RV correction is $\sim 0{,}5$ m s^{-1}.

3.2 Expressions for the precession quantities

To compare astronomical observations with calculated places of celestial objects one has to refer either the observed or the calculated position to the same reference coordinate system. The effects like precession, nutation, aberration and parallax need to be taken into account.

In Fig. 10 we display the celestial sphere with mean ecliptics and equators for two epochs. ε_F is an arbitrary fixed epoch or a basic epoch and ε_D is the mean epoch of date. $\overline{P}_0$ and P represent the mean pole of the Earth's equator at epochs ε_F and ε_D, respectively, while $\overline{C}_0$ and C represent the ecliptic pole at these two epochs. The vernal equinox at ε_F is denoted by $\overline{\Upsilon}_0$ and the mean equinox of date is denoted by Υ.

The equatorial precession quantities ζ_A, z_A and θ_A displayed in Fig. 10 are the most appropriate angles to precess from a fixed equinox and equator at epoch ε_F to the mean equinox and equator of date ε_D. The transformation in equatorial rectangular coordinates can be clearly seen from Fig. 10:

$$(x, y, z)_{\varepsilon_D} = (x, y, z)_{\varepsilon_F} R_z(\zeta_A) R_y(\theta_A) R_z(z_A) = (x, y, z)_{\varepsilon_F} A, \tag{21}$$

where

$$R_z(\alpha) = \begin{bmatrix} \cos\alpha & \sin\alpha & 0 \\ -\sin\alpha & \cos\alpha & 0 \\ 0 & 0 & 1 \end{bmatrix} \tag{22}$$

is a rotation by the angle α about z axis and analogically

$$R_y(\alpha) = \begin{bmatrix} \cos\alpha & 0 & \sin\alpha \\ 0 & 1 & 0 \\ -\sin\alpha & 0 & \cos\alpha \end{bmatrix} \tag{23}$$

is a rotation about y axis. After matrix multiplications the elements of the matrix A are obtained:

$$\begin{aligned}
a_{11} &= \cos\zeta_A \cos\theta_A \cos z_A - \sin\zeta_A \sin z_A \\
a_{12} &= \cos\zeta_A \cos\theta_A \sin z_A + \sin\zeta_A \cos z_A \\
a_{13} &= \cos\zeta_A \sin\theta_A \\
a_{21} &= -\sin\zeta_A \cos\theta_A \cos z_A - \cos\zeta_A \sin z_A \\
a_{22} &= -\sin\zeta_A \cos\theta_A \sin z_A + \cos\zeta_A \cos z_A \\
a_{23} &= -\sin\zeta_A \sin\theta_A \\
a_{31} &= -\sin\theta_A \cos z_A \\
a_{32} &= -\sin\theta_A \sin z_A \\
a_{33} &= \cos\theta_A .
\end{aligned} \tag{24}$$

The IAU precession-nutation model used before 2000 was composed of the IAU 1976 precession (Lieske et al., 1977) and IAU 1980 nutation (Wahr, 1981; Seidelmann, 1982). Lieske et al. (1977) developed expressions for the precession quantities at epoch J2000.0 as a function of the revised fundamental astronomical constants adopted by the International Astronomical Union at the XVI. General Assembly in Grenoble. The development of the usual precession quantities depends upon the dynamical motion of the ecliptic pole relative

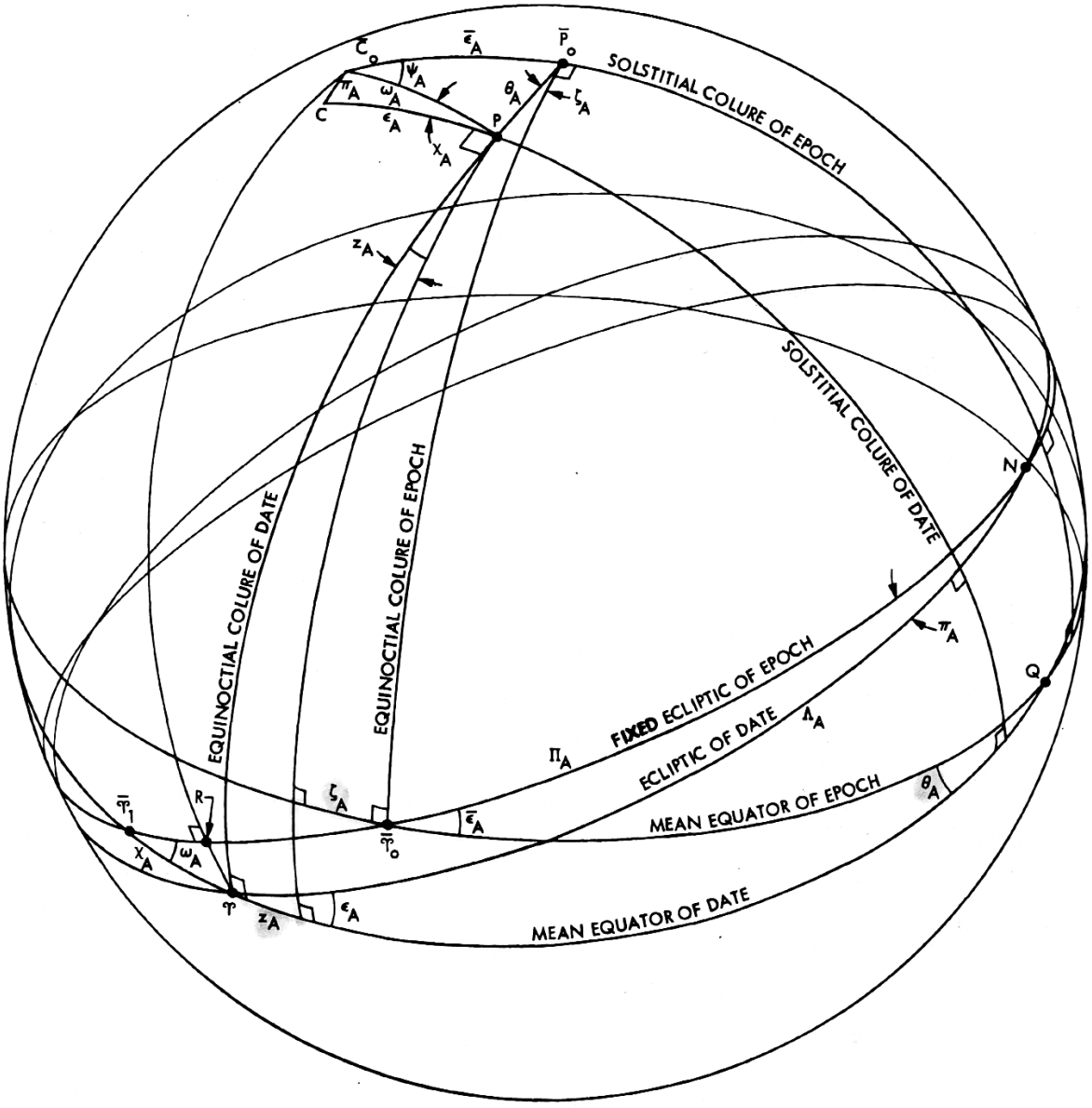

Figure 10: Celestial sphere with mean ecliptics and equators shown for two epochs, a fixed epoch ε_F and an epoch of date ε_D. $\overline{P}_0$ and P represent the mean pole of the Earth's equator and $\overline{C}_0$ and C represent the ecliptic pole at these two epochs. The vernal equinox at ε_F is denoted by $\overline{\Upsilon}_0$ while the mean equinox of date is denoted by Υ. Adopted from Lieske et al. (1977).

to a fixed ecliptic, due to planetary perturbations, and upon the dynamical motion of the celestial pole due to luni-solar torques on the oblate Earth. However, the IAU 1976 precession model has a number of limitations (Capitaine et al., 2003).

In 2000 IAU adopted new resolution and recommended previous models to be replaced since 2003 January 1 by the IAU 2000 precession-nutation model, specifically by the MHB 2000 model provided by Mathews et al. (2002). MHB 2000 model includes a new nutation series for the non-rigid Earth and corrections to the precession rates in longitude and obliquity. This model is oriented with respect to the International Celestial Reference System (ICRS) through a fixed 3D rotation between the mean equatorial frame at J2000.0 and the Geocentric Celestial Reference System (GCRS). This rotation, called the 'frame bias', includes the numerical values for the pole offset at J2000.0 that MHB 2000 specifies and the equinox offset at J2000.0 that MHB 2000 does not specify. The equinox offset has only a second-order effect on the final transformation between celestial and terrestrial coordinates, however, in fact, it is dynamically inconsistent and the theory suffers, except of the improvements in the precession rates, from the same limitations as the IAU 1976 precession. The only corrections that have been applied in the IAU 2000 model are the MHB corrections to precession rates in longitude and obliquity, but the expressions used for the motion of the ecliptic and other quantities of precession still remained the same as in Lieske et al. (1977). Woolard & Clemence (1966) remarked that the motion of the equator and ecliptic are *kinematically* independent, but the motion of the equator depends *dynamically* upon the variations of the disturbing forces caused by changes in the positions of the Sun, the Moon and other planets in the Solar system. Hence the improvement of the model for the precession of the equator requires also the use of an improved model for the ecliptic.

An improved IAU 2000 precession model was realized by Capitaine et al. (2003). They have clearly separated precession of the equator and precession of the ecliptic and obtained the developments of the quantities through two independent approaches. One of them uses the expressions for the primary precession angles to derive equatorial precession angles:

$$\begin{aligned}
\zeta_A &= 2''.650545 + 2306''.083227t + 0''.2988499t^2 \\
&\quad + 0''.01801828t^3 - 0''.000005971t^4 - 0''.0000003173t^5 \\
z_A &= -2''.650545 + 2306''.077181t + 1''.0927348t^2 \\
&\quad + 0''.01826837t^3 - 0''.000028596t^4 - 0''.0000002904t^5 \\
\theta_A &= 2004''.191903t - 0''.4294934t^2 - 0''.04182264t^3 \\
&\quad - 0''.000007089t^4 - 0''.0000001274t^5,
\end{aligned} \tag{25}$$

where t is the elapsed time in Julian centuries since J2000 of the Terrestrial time (TT) and is defined by:

$$t = (\text{ TT} - 2000 \text{ January 1d 12h TT})/36525, \tag{26}$$

with TT in days. It would be correct to use the Terrestrial dynamical barycentric time (TDB) instead of TT, but the difference TDB – TT is well below the required accuracy.

Another necessary quantity is an improved expression for the Greenwich Mean Sidereal Time (GMST), because it directly depends on the precession in right ascension. Capitaine

et al. (2003) derived the formula with a resolution of 0.1 microsecond:

$$\begin{aligned} \mathrm{GMST} &= \mathrm{UT1} + 24110.5493771 + 8640184.79447825t_u \\ &\quad + 307.4771013(t - t_u) + 0.092772110t^2 \\ &\quad - 0.0000002926t^3 - 0.00000199708t^4 \\ &\quad - 0.000000002454t^5 \text{ s}, \end{aligned} \tag{27}$$

where t_u is the UT1, the proper rotational time of the Earth, expressed in Julian centuries since J2000.

In 2006 the IAU recommended the precession theory of Capitaine et al. (2003) for the precession of the equator and the ecliptic, and it is the one used in BARCOR.

3.3 Radial-velocity correction

The equatorial coordinate system is defined by the xy plane which is consistent with the Earth Mean-equator related to the fixed epoch J2000.0 of inertial reference frame, so that x axis points to the vernal equinox of epoch J2000.0. Perpendicular to the xy plane is the Earth rotational axis z. The projected Earth velocity in the equatorial coordinate system is:

$$\begin{aligned} V_x &= V_x^{orb} + V_x^{rot} \\ V_y &= V_y^{orb} + V_y^{rot} \\ V_z &= V_z^{orb}, \end{aligned} \tag{28}$$

where V_x, V_y and V_z are sums of velocities V_x^{orb}, V_y^{orb} and V_z^{orb}, caused by the Earth orbital motion, and V_x^{rot}, V_y^{rot} and V_z^{rot}, caused by the Earth rotation. Since z axis is the Earth rotational axis, $V_z^{rot} = 0$.

The velocity of the observer due to the Earth rotation, V^{rot}, is:

$$V^{rot} = \frac{2\pi k}{24 \cdot 3600 \cdot 1000} \left(h + \frac{6378137}{\sqrt{1 - e^2 \sin^2 \phi}} \right) \cos \phi \ (\mathrm{km\,s^{-1}}), \tag{29}$$

where h is the altitude of the observatory above the sea level (in meters), ϕ is the geodetic latitude, and $e^2 = 2f - f^2$, where f is the Earth flattening (see section §3.1). k is the ratio of the mean solar to the mean sidereal day and equals:

$$k = 1.002737909350795 + 5.9006 \cdot 10^{-11} t - 5.9 \cdot 10^{-15} t^2, \tag{30}$$

where t was defined in Eq. (26). GMST is computed using Eq. (27) and the Local Mean Sidereal Time (LMST) is:

$$\mathrm{LMST} = \left(\frac{\mathrm{GMST}}{86400} - \frac{l}{360} \right) 2\pi \ (\mathrm{rad}), \tag{31}$$

where l is the longitude of the observatory (in degrees, positive to east).

The projected velocity of the observer due to the Earth rotation, V^{rot}, in the equatorial coordinate system is:

$$\begin{aligned} V_x^{rot} &= -V^{rot} \sin(\mathrm{LMST}) \\ V_y^{rot} &= V^{rot} \cos(\mathrm{LMST}) \\ V_z^{rot} &= 0. \end{aligned} \tag{32}$$

To compute the RV barycentric correction, RV_{corr}, the Earth velocities V_x, V_y and V_z in Eqs. (28) have to be projected to a line of sight of the observer. The simplest way is using spherical coordinates that are defined as following:

$$\begin{aligned} x &= \cos\alpha \cos\delta \\ y &= \sin\alpha \cos\delta \\ z &= \sin\delta, \end{aligned} \tag{33}$$

where α and δ are right ascension and declination of the object at the epoch of the coordinates and have to be corrected for the precession, as described in section §3.2. Then the projections p_1, p_2 and p_3, of the velocity V_x, V_y and V_z, respectively, to a line of sight of the observer, are:

$$\begin{pmatrix} p_1 \\ p_2 \\ p_3 \end{pmatrix} = \begin{pmatrix} a_{11} & a_{12} & a_{13} \\ a_{21} & a_{22} & a_{23} \\ a_{31} & a_{32} & a_{33} \end{pmatrix} \begin{pmatrix} x \\ y \\ z \end{pmatrix} = A \begin{pmatrix} x \\ y \\ z \end{pmatrix}, \tag{34}$$

where A is the precession matrix from Eq. (21), and the parameter t in Eqs. (25) is:

$$t = (\ \mathrm{TT} - \mathrm{EKV})/36525. \tag{35}$$

EKV is the epoch of the coordinates in time units (Julian Date) that can be generally different from J2000.0.

The Earth velocity components computed from the JPL's ephemerides are related to the epoch J2000.0, therefore they have to be precessed from the epoch J2000.0 to the time of the observation:

$$\begin{pmatrix} V_x^{orb} \\ V_y^{orb} \\ V_z^{orb} \end{pmatrix} = \begin{pmatrix} a_{11} & a_{12} & a_{13} \\ a_{21} & a_{22} & a_{23} \\ a_{31} & a_{32} & a_{33} \end{pmatrix} \begin{pmatrix} V_x^{JPL} \\ V_y^{JPL} \\ V_z^{JPL} \end{pmatrix}, \tag{36}$$

where V^{JPL} are velocities from JPL's ephemerides and the parameter t is the same as in Eq. (26). Finally, the RV barycentric correction, RV_{corr}, is:

$$RV_{corr} = V_x p_1 + V_y p_2 + V_z p_3 \tag{37}$$

with V_x, V_y and V_z defined in Eqs. (28).

3.4 Time correction

The geocentric Julian Date is computed using the modified function GEO written by J. Vondrák in 2001. Positions and velocities obtained from the JPL Planetary and Lunar Ephemerides DE405 are computed using a Julian Ephemeris Date, JED, which is based on the dynamic Terrestrial time, TT, and is defined as:

$$\mathrm{JED} = \mathrm{TAI} + \frac{32.184}{86400} = \mathrm{UT1} + \triangle\mathrm{T} + \frac{32.184}{86400}\ \mathrm{(d)}. \tag{38}$$

TAI is the Atomic time and $\triangle$T is a correction resulting from a non-uniformity of the Earth rotation. It is the difference between the uniformly passing time TT and the Earth rotational time UT1. $\triangle$T is determined from observations of the International Earth Rotation Service. UTC is the coordinated Universal time UT and the difference $\mathrm{TAI} - \mathrm{UTC} = n$ changes by adding leap seconds to ensure $|\ \mathrm{UT1} - \mathrm{UTC}| < 0.8$ s.

The barycentric coordinates of the Earth in the equatorial coordinate system computed from the JPL Planetary and Lunar Ephemerides are related to the epoch J2000.0 as well as the Earth velocity components. In case the star coordinates are given in the epoch other than J2000.0 the precession from that epoch to the epoch J2000.0 has to be done:

$$\begin{pmatrix} x_{2000} \\ y_{2000} \\ z_{2000} \end{pmatrix} = \begin{pmatrix} a_{11} & a_{12} & a_{13} \\ a_{21} & a_{22} & a_{23} \\ a_{31} & a_{32} & a_{33} \end{pmatrix} \begin{pmatrix} x \\ y \\ z \end{pmatrix}. \tag{39}$$

The formula is similar to Eq. (34), but here the parameter t is:

$$t = (\mathrm{J2000} - \mathrm{EKV})/36525 \tag{40}$$

with both J2000 and EKV expressed in Julian Dates. The barycentric correction of the time, T_c, is:

$$T_c = L(C_x x_{2000} + C_y y_{2000} + C_z z_{2000})\ \mathrm{(d)}, \tag{41}$$

where C_x, C_y and C_z are individual barycentric coordinates of the Earth computed from the JPL's ephemerides and L is a time that takes for a light to pass one Astronomical Unit in vacuum:

$$L = \frac{499.004782}{86400}\ \mathrm{(d)}. \tag{42}$$

3.5 Program tests and error estimates

There are two approaches how to compute barycentric corrections. One of them is an analytical theory using developments of series of many terms and another is numerical integration of N-body system. An analytical theory is used in the program BRVEL written by Yang & Amor in 1984, who utilized procedures of Stumpff (1977, 1979, 1980). Another procedure using an analytical theory is AABER1 written by Ron & Vondrák (1986) for the

	α (h)								
δ (°)	0	4	8	12	16	20	21	22	23
90	35 6/1985	39 7/1992	34 7/1992	36 7/1992	36 7/1992	37 7/1992	35 7/1992	39 7/1992	37 7/1992
-90	44 12/1994	43 12/1994	47 12/1994	47 12/1994	46 12/1994	45 12/1994	47 12/1994	42 12/1994	46 12/1994
70	33 5/2003	44 7/1992	46 8/2002	44 8/2002	25 8/2002	23 3/1998	25 3/1998	28 4/2002	31 5/2003
-70	51 2/1996	31 2/1996	35 12/1994	53 12/1994	64 12/1994	58 12/1994	56 2/1996	56 2/1996	54 2/1996
50	49 5/2002	52 5/1991	57 8/2002	59 9/2002	40 10/1997	38 1/1991	39 4/2002	45 4/2002	48 4/2002
-50	63 3/1988	32 2/2006	36 8/1994	59 11/2000	73 12/2000	69 2/1988	70 2/1988	69 2/1996	66 3/1988
30	61 5/2002	60 5/1991	61 8/2000	70 9/2002	51 10/1997	54 1/1991	55 2/1988	60 3/1988	61 4/2002
-30	74 3/1988	47 7/2000	51 8/2000	62 11/2000	77 12/2000	79 2/1988	80 2/1988	78 3/1988	78 3/1988
10	70 4/1988	61 7/2000	66 8/2000	72 9/2002	66 12/2002	71 2/1988	72 2/1988	75 3/1988	75 3/1988
-10	77 3/1988	58 7/2000	63 8/2000	65 9/2002	74 12/2002	79 2/1988	80 2/1988	81 3/1988	82 3/1988

Table 1: BARCOR testing. The two numbers for each α and δ are the value (in $\mathrm{cm\,s^{-1}}$) and the date of a maximum difference of RV corrections between the programs BARCOR and BRVEL.

computation of the Earth barycentric velocity components. However, the most accurate theory is the JPL Planetary and Lunar Ephemerides using numerical N-body integrations.

Stumpff (1980) compared the Earth barycentric velocity components computed using an analytical theory with the JPL's ephemeris DE96 and found a maximum error 42 $\mathrm{cm\,s^{-1}}$. Ron & Vondrák (1986) compared their velocity components with the JPL's ephemeris DE200 and declared the maximum error 17 $\mathrm{cm\,s^{-1}}$. Using JPL's Planetary and Lunar Ephemerides with the accuracy of the velocity components about few $\mathrm{cm\,s^{-1}}$, which is achieved by the continuous measurements of the Earth-Moon distance by the laser telemeter with the accuracy of 1 – 2 cm, makes BARCOR very accurate, with the accuracy of RV correction of few $\mathrm{cm\,s^{-1}}$.

To find out more details about the accuracy of RV corrections we compared results from BARCOR and BRVEL. We computed RV corrections using both programs over the complete range of right ascensions α from 0 to 24 h, and declinations from $-90°$ to $+90°$, for the first day of each month and years 1980 – 2006. In Table 1 the two numbers for each α and δ are the value and the date of a maximum difference of RV corrections between

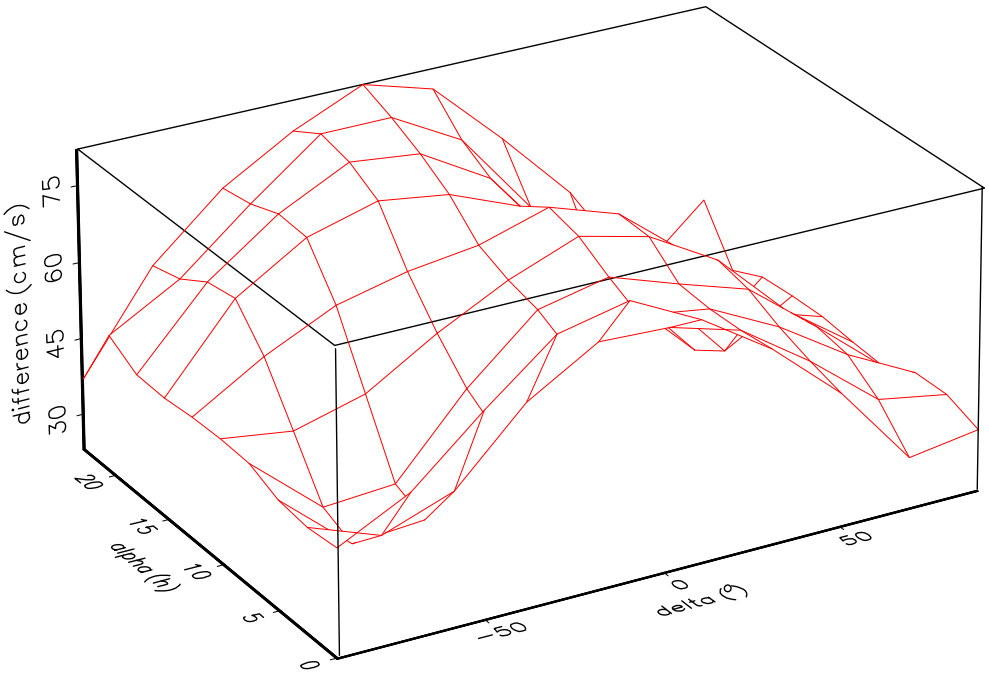

Figure 11: The graphical representation of the differences in RV corrections between the programs BARCOR and BRVEL.

the two programs. The RV corrections were computed for the Observatory Ondřejov in the Czech Republic (longitude $0^{\mathrm{h}}59^{\mathrm{m}}8\overset{\mathrm{s}}{.}1$, latitude $+49°54'38''$, altitude 528 m) and for the epoch of the coordinates J2000.0. In the epoch B1950.0 the differences between the two programs appears even smaller.

In Fig. 11 the results from Table 1 are displayed. The maximum difference between RV corrections from the programs BARCOR and BRVEL occurs near the celestial equator and right ascension 22 – 23 h. The differences correspond to the error estimates by Stumpff (1980). We found the discrepancy in differences at the declination $\delta = -90°$ and $+90°$. The differences should be the same for all values of right ascension, because it is always the same point – the Earth north or south pole. In this case BARCOR is consistent, but BRVEL is not.

To find out the barycentric time correction accuracy the Barycentric Julian Dates (BJD) computed by BARCOR and BRVEL were compared and the very small maximum difference of 0.0000003 d $\sim$ 0.03 s was found.

The BARCOR's accuracy of RV corrections of few $\mathrm{cm\,s^{-1}}$ is good enough for expected high accurate RV measurements obtained using the 'astro-comb' calibration technique in the future. However, apart of problems raising from the intrinsic variability of the target itself, there are few complications. First of all, the geographic position for the RV correction should be chosen carefully. The difference between RV corrections computed for the spectrograph position and the telescope tube position can be up to few tens of $\mathrm{cm\,s^{-1}}$ depending on the size of the telescope tube and telescope pointing. Second, due to changes in the Earth atmosphere it is difficult to determine accurately the mid-exposure time. In an extreme case when the mid-exposure time is off by one minute, the RV correction error can be 1 $\mathrm{m\,s^{-1}}$ for a star close to a horizon and 0.1 $\mathrm{m\,s^{-1}}$ for a star close to a meridian. One should be aware of all these issues when high accurate RV measurements are required.

4 Photometry of transiting exoplanets

When a new transiting extrasolar planet is discovered, system parameters can be determined from its light curve. Different combinations of system parameters result in a different shape of a light curve, and best-fitting parameters can be found from the best agreement between the data and the model. However, good quality light curves are needed and getting accurate photometry from the ground is not an easy task. Systematic errors in photometric measurements and also data reduction and light-curve modelling techniques have influence on resulting system parameters. In this chapter we discuss some aspects of accurate photometry in section §4.1 and show how to compute system parameters from a light curve in section §4.2.

4.1 Accurate photometry

Achieving photon-noise photometry is a difficult task as many systematic effects, or systematics, can disturb photometric measurements. The resulting photometric accuracy depends on a combination of two kinds of a noise. First, the photon noise, is always present and can be described by Poisson distribution. It is uncorrelated 'white' noise and averages down as $(1/N)^{1/2}$, where N is the number of measurements. The other noise component almost always present in transiting data is a correlated 'red' noise (low-frequency noise) which remains constant for specific N, corresponding to changes in airmass, seeing, temperature, telescope tracking, flat-field errors and/or other effects, varying gradually over timescales from one to a few hours, a typical transit duration. All these effects introduce some covariance between individual light-curve points.

4.1.1 Systematic noise

The detection-significance statistic for transit surveys in the presence of the 'red' noise was first presented by Pont et al. (2006). Pont et al. (2007a) examined a level of correlated noise for major photometric wide-field surveys and concluded that the 'red' noise causes the standard deviation of the mean to be 2 – 3 times larger than expected for only uncorrelated noise over transit-duration timescales. They also found that for larger telescopes the 'red' noise is independent of magnitude, whereas for small-aperture telescopes it is proportional to the photon noise. However, surprisingly they found no relation between the survey depth (deep or shallow surveys) and the 'red'-noise amplitude.

4.1.2 Astrophysical sources of systematics

In addition to instrumental and atmospheric sources of systematic noise other possible source is the influence of star spots. The light curve can be distorted if the planet transits in front of a spot or due to intrinsic variability of the star, which complicates any transit timing analysis. The system parameters and the mid-eclipse times derived can then be affected by an inappropriate fitting model. To overcome this problem, one needs to obtain

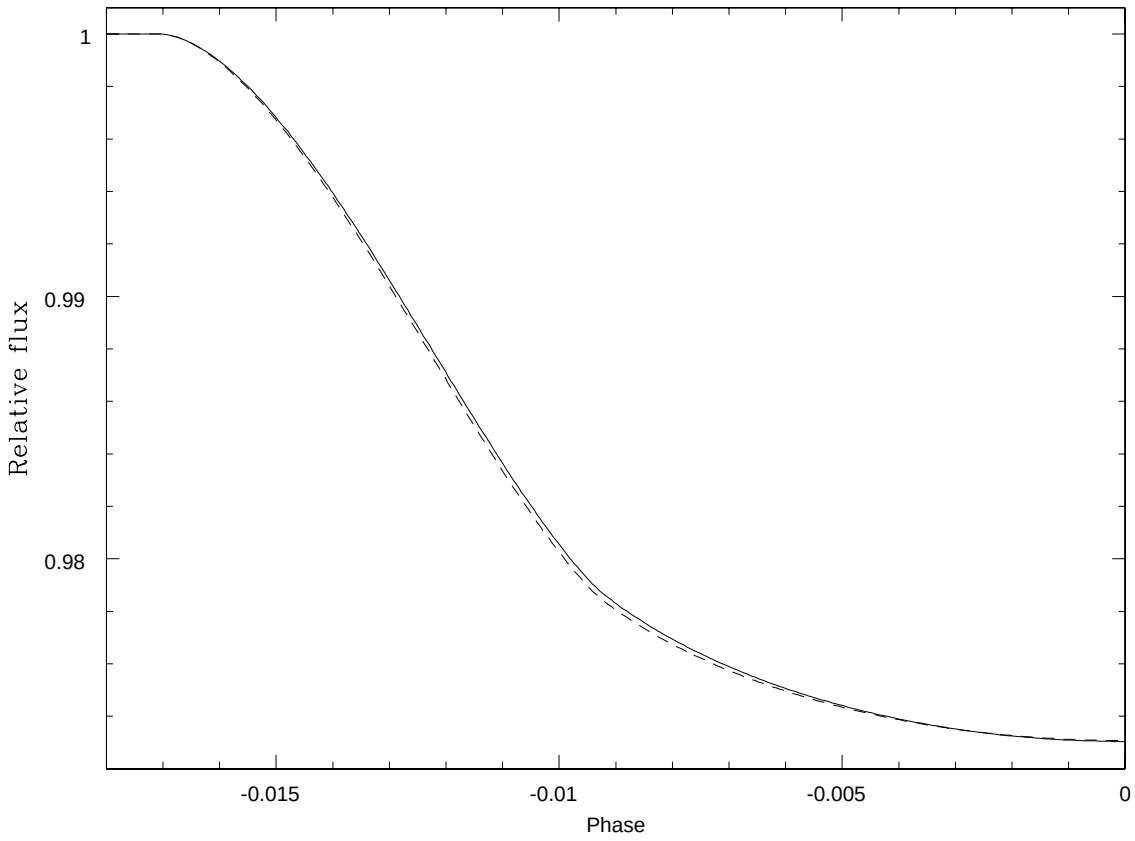

Figure 12: Theoretical ingress part of a light curve for HD 189733 transiting exoplanet system computed using formulas of Mandel & Agol (2002) and limb darkening coefficients for the Strömgren y filter from the tables of Claret (2000). The solid line corresponds to 5,000 K, a real estimated temperature of HD 189733 (Bouchy et al., 2005). If a planet during ingress transits a 'plage' region that is 250 K warmer than the surrounding photosphere, the shape of a light curve is slightly changed (the dashed line).

a light curve over the whole planet orbital period to reveal the presence of star spots. However, this can only be carried out from the space.

An accurate photometry can be also affected by regions on the stellar surface that are hotter than the surrounding, the so called 'plage' regions. If the planet would transit these regions during ingress or egress, a light curve would be asymmetric and one should use different limb darkening coefficients for different parts of the light curve. However, this subtle effect was not observed yet, or was not found due to noise and systematic errors in the data. For example, the Sun's 'plage' regions are only $\sim$ 100 K warmer then the nearby photosphere. In Fig. 12 we display theoretical light curves using limb darkening coefficients for two different temperatures of HD 189733, the star harbouring a transiting planet. The solid line corresponds to 5,000 K, whereas the dashed line to 5250 K. Despite of a subtle

difference, the effect might be observable with the Kepler satellite or future photometric missions.

4.2 Light-curve modelling

To estimate the system parameters we used a parametrized model where we assumed a circular orbit around the centre of mass to calculate the separation of the planet and star centres, z, normalised to stellar radius, as a function of time, t, that elapsed from the mid-transit time:

$$z = \frac{a}{R_\star}\sqrt{\sin^2\left(\frac{2\pi t}{P}\right) + \cos^2(i)\cos^2\left(\frac{2\pi t}{P}\right)}, \tag{43}$$

where a, $R_\star$, P and i were defined in section §2.3.1. We assumed a quadratic limb darkening law:

$$\frac{I_\mu}{I_0} = 1 - u_1(1-\mu) - u_2(1-\mu)^2, \tag{44}$$

where I is the intensity, μ is the cosine of the angle between the line of sight and the normal to the stellar surface, and u_1 and u_2 are the linear and quadratic limb darkening coefficients. Initially we used a non-linear limb darkening law in a form:

$$\frac{I_\mu}{I_0} = 1 - c_1(1-\mu^{1/2}) - c_2(1-\mu) - c_3(1-\mu^{3/2}) - c_4(1-\mu^2), \tag{45}$$

where c_1 to c_4 are four non-linear limb darkening coefficients. However, the computational time is higher when using non-linear limb darkening coefficients, and also the quality of ground-based photometry is not good enough to determine independently all four coefficients, c_1 to c_4.

The best-fitting light-curve parameters can be obtained via minimization of the function χ^2:

$$\chi^2 = \sum_{i=1}^{N}\left[\frac{f_i(obs) - f_i(theor)}{\sigma_i}\right]^2, \tag{46}$$

where $f_i(obs)$ is the flux observed at time i, σ_i is the corresponding flux uncertainty, and $f_i(theor)$ is the fraction of the stellar flux occulted by the planet calculated from the normalised separation, z, and the planet-to-star radius ratio, ρ, using the analytic formulas of Mandel & Agol (2002).

In our light-curve program parameters that can be derived are: planetary and stellar radius, orbital inclination and mid-transit times. For good-quality data it is also possible to obtain limb darkening coefficients. Another possibility is to fit for additional parameters related to the normalisation of each light-curve. Finally, using Eqs. (2), (3) and (4) additional parameters can be derived – a transit depth, duration and impact parameter.

The two studied transiting systems, HD 189733 in section §6 and TrES-1 in section §7, have the transiting planet on a circular orbit. However, $\sim 25\,\%$ of transiting planets found to date are on eccentric orbits for which Eqs. (2), (3) and (4) given by Seager &

Mallén-Ornelas (2003) are no longer valid. Moreover, Barnes (2007) computed that transit detection probabilities are higher by a factor of $(1 - e^2)^{-1}$ for eccentric systems, which means that analysing light curves for eccentric transiting planets will become common. The most elaborate model including planet's orbital eccentricity was presented by Kipping (2008). They derived projected star-planet separation, z, for an eccentric planetary orbit which can be directly used as an input into the equations of Mandel & Agol (2002), and so the limb darkening can be included. Seager & Mallén-Ornelas (2003) recommended to use an independent measurement of the stellar mass in order to determine the stellar radius. In addition, Kipping (2008) shown that eccentricity, e, and longitude of periastron, ω, must also be determined by an independent observation for eccentric systems, before the stellar radius can be determined. Using new analytic model for an eccentric orbit Kipping (2008) also investigated the asymmetry of the light curve, the shift in the mid-transit time and the effect of eccentricity on the ingress and egress slopes.

4.2.1 Uncertainty of best-fitting parameters

Methods to estimate uncertainties of best-fitting parameters are the following:

1. *Constant-$\Delta\chi^2$ boundaries* – First, χ^2 is evaluated at points on a grid in the parameter space near to the maximum likelihood estimate of the model parameters. Then confidence intervals are calculated by finding the boundary along which χ^2 is constant. However, many evaluations of χ^2 are needed, particularly when the number of parameters is large, and therefore this technique is not practical.

2. *Bootstrap resampling* – The fitting technique is applied repeatedly to many sets of simulated data, generated by adding Gaussian random values to the actual data points. Each set of simulated data represents a possible set of measured values. Applying the same fitting procedure to actual and simulated data provides the distribution of best-fitting parameter values. For each synthetic data set we need to determine best-fitting parameters, and therefore a computational time can be large. Moreover, resulting uncertainties depend on simulated data, which do not necessarily estimate the true distribution.

   Agol & Steffen (2007) used the Monte Carlo bootstrap simulation of the errors where the residuals between the model and the data are shifted by a random number of points for each transit so that the correlations are maintained. The shifted residuals are added to the best-fitting model and re-fitted, which is repeated many times to give an estimate of the errors including systematic effects and correlated noise.

3. *Markov-Chain Monte Carlo (MCMC)* – MCMC allows for correlated and non-Gaussian uncertainties in fitted parameters and it is more efficient computationally, particularly for high-dimensional parameter spaces. Moreover, calculating the next step in a chain is much faster than performing an additional minimization with resampled data.

4.2.2 Markov-Chain Monte Carlo simulations

Comparison of the bootstrap resampling and MCMC simulation gives similar results (Holman et al., 2006). We used MCMC simulations (Tegmark et al., 2004; Ford, 2005, 2006a; Holman et al., 2006) to estimate uncertainties of fitted parameters in our data. The goal of the MCMC method is to generate a chain of states sampled from a desired probability distribution. We used the Metropolis-Hastings algorithm (Ford, 2005) where chains are created as follows. First, each chain is initialized with parameters created by adding ± 1 – 5σ to their previously determined best-fitting values, where σ is a parameter uncertainty. A trial state, $\mathbf{x}^{new}$, is generated from the old state, $\mathbf{x}^{old}$, according to a candidate transition probability function, $q(\mathbf{x}^{new}|\mathbf{x}^{old})$. Then $\chi^2(\mathbf{x}^{new})$ for the trial state and $\chi^2(\mathbf{x}^{old})$ for the current state are calculated using the χ^2 fitting statistic according to Eq. (46). The new parameter set is accepted if $\chi^2(\mathbf{x}^{new}) < \chi^2(\mathbf{x}^{old})$, or accepted with a probability:

$$p = \exp\left[\frac{\chi^2(\mathbf{x}^{old}) - \chi^2(\mathbf{x}^{new})}{2}\right] \tag{47}$$

if $\chi^2(\mathbf{x}^{new}) > \chi^2(\mathbf{x}^{old})$.

We used a Gaussian distribution centred around $\mathbf{x}$ generated from the modification of the function GASDEV (Press et al., 1992). Our transition probability function is:

$$q(x_\mu^{new}|x_\mu^{old}) = \frac{1}{\sqrt{2\pi\beta_\mu^2}} \exp\left[-\frac{(x_\mu^{new} - x_\mu^{old})^2}{2\beta_\mu^2}\right], \tag{48}$$

where μ stands for one chosen parameter. The scale factors, β, has to be chosen individually for each parameter. If trial states are chosen with too large dispersion, a large fraction will be rejected, and the chain will remain at each state for several trials which will slow down the convergence. If trial states are chosen with too small dispersion, then the small step size will cause that the chain behaves like a random walk. Unfortunately, for multidimensional parameter spaces, it is not always obvious how to change scales to obtain a desired acceptance rate. Therefore, we used the Metropolis-Hastings algorithm within the Gibbs sampler, where the parameters are altered in the next trial state according to randomly generated permutations of the model parameters. Particularly, randomly chosen parameter at each step, x_μ, is altered according to Eq. (48) and all the other parameters are left unchanged. The scale factors, β, were chosen so that $\sim 44\,\%$ of parameter sets were accepted (Gelman et al., 2003; Ford, 2006a). For each night, 10 independent chains were created, with the length of at least 100,000 points per each chain to ensure the chain convergence. The first $20\,\%$ of each chain was discarded to minimize the effect of initial conditions.

We used MCMC simulations to determine both best-fitting parameters and their uncertainties. This was possible because we had observations of transiting extrasolar systems where the initial estimate of the orbital parameters was known. The best-fitting value was computed as the mean value of the probability distribution, $\bar{x}_\mu$, and the 1σ uncertainty according to the $68\,\%$ confidence limits:

$$(\bar{x}_\mu - 0.99446\,\sigma, \bar{x}_\mu + 0.99446\,\sigma), \tag{49}$$

where σ is the standard deviation and the number 0.99446 tells that 68 % of values lies closer than $0.99446\,\sigma$ from the mean value and can be derived using the theory of statistics and probability. Using the mean value and the standard deviation to estimate best-fitting parameters and their uncertainties is a good choice as the resulting probability distribution was always close to Gaussian distribution.

4.2.3 Gelman & Rubin R statistic

The convergence of generated chains was checked using the Gelman & Rubin (1992) R statistic, where the mean of the empirical variance of each parameter within each chain has to be close to the variance of the mean of the same parameter across the chains, which means that for a given fitted parameter all possible values in a parameter space are explored in each chain.

Following Gelman et al. (2003) and Ford (2006a), we denote our fitted parameter as x_{ic} at each iteration indexed by i of each chain indexed by c. We have N_c chains, each of the length L_c, that includes all the accepted parameter values without the first 20 %. The mean value of x_{ic} in each chain is:

$$\bar{x}_{.c} = \frac{1}{L_c} \sum_{i=1}^{L_c} x_{ic} \tag{50}$$

and the average of the variances of x_{ic} within each chain is:

$$W(x) = \frac{1}{N_c} \sum_{c=1}^{N_c} \frac{1}{L_c - 1} \sum_{i=1}^{L_c} (x_{ic} - \bar{x}_{.c})^2. \tag{51}$$

The mean value of the parameter from all the chains is:

$$\bar{x}_{..} = \frac{1}{N_c} \sum_{c=1}^{N_c} \bar{x}_{.c} = \frac{1}{L_c N_c} \sum_{c=1}^{N_c} \sum_{i=1}^{L_c} x_{ic} \tag{52}$$

and the variance of the single chain means is:

$$B(x) = \frac{L_c}{N_c - 1} \sum_{c=1}^{N_c} (\bar{x}_{.c} - \bar{x}_{..})^2. \tag{53}$$

Then the estimate of the variance of x_{ic} using a weighted average of $W(x)$ and $B(x)$ is:

$$\mathrm{var}(x) = \frac{L_c - 1}{L_c} W(x) + \frac{1}{L_c} B(x). \tag{54}$$

Using these quantities, we can write an estimate of $R(x)$ as:

$$R(x) = \sqrt{\frac{\mathrm{var}(x)}{W(x)}}. \tag{55}$$

When the individual chains approach convergence, $R(x)$ approaches 1 from above.

In our MCMC simulations we checked $R(x)$ for each fitted parameter regularly after first 100,000 steps in each chain to find out whether all chains converged, and the process was terminated when $R(x) < 1.01$. Usually the convergence was achieved after 100,000 steps in each chain.

4.2.4 Accounting for correlated 'red' noise

To estimate appropriate error bars in our data accounting for any correlated noise, we used a procedure similar to that of Gillon et al. (2006) and Narita et al. (2007). Initially we assigned the same error bars to all the data points including only Poisson noise. Then the differences between the data and the model were found and the data error bars were rescaled to satisfy the condition $\chi^2/N_{DOF} = 1.0$, where N_{DOF} is the total number of measurements in each light curve. We assumed that our initial model is a good description of a light curve. The amplitude of systematic trends in photometry was estimated from the standard deviation over one residual point, σ_1, and from the standard deviation of the average of the residuals over N successive points, σ_N. We solved the following system of two equations given by Gillon et al. (2006):

$$\sigma_1^2 = \sigma_w^2 + \sigma_r^2, \tag{56}$$

$$\sigma_N^2 = \frac{\sigma_w^2}{N} + \sigma_r^2, \tag{57}$$

to obtain the amplitude of the 'white' noise, σ_w, and the 'red' noise, σ_r. The error bars were then adjusted by multiplying by $[1 + N(\sigma_r/\sigma_w)^2]^{1/2}$ and these rescaled uncertainties were used for the subsequent fitting procedure. To account properly for the systematic errors, the resulting multiplying factor was computed as the average of values using different N in the range 15 – 30 minutes (the typical time scale of ingress and egress).

5 51 Peg

In my diploma thesis (Hrudková, 2005) we discovered possible changes in the observed minus calculated values ($O-C$) of the 51 Peg system. To verify these changes we needed more RV measurements of this system. They were collected using the coudé echelle spectrograph on the 2-m Alfred-Jensch Telescope in Thüringer Landessternwarte Tautenburg, Germany, in October and November 2007.

5.1 Iodine cell calibration technique

To calibrate stellar spectra Griffin & Griffin (1973) suggested to pass the star light through an absorbing medium before it enters the spectrometer, therefore superimposing reference absorption lines that have the same instrumental shifts and distortions as the stellar spectrum. Several groups tried this approach with different absorbing media, leaving the iodine absorption cell as the best candidate. Marcy & Butler (1992) and later Valenti et al. (1995) presented a method how to use a iodine absorption cell to determine accurately RV of each stellar spectrum. This method was incorporated in echelle spectrograph in Tautenburg and was used for 51 Peg observations.

As explained by Marcy & Butler (1992), a star light passes through the iodine absorption cell, superimposing iodine lines on the stellar spectrum. The resulting composite spectrum enters the echelle spectrometer where it is convolved with the instrumental profile. The principle of the method is based on the fact that the observed shift of a stellar spectrum consists of the actual Doppler shift and a small spurious shift due to instrumental effects. These spurious shifts appear in iodine lines as well, and can then be applied as a correction to the observed shift of a stellar spectrum. The spurious shifts can be caused by several reasons, e. g. movements of the photocentre of the telescope pupil at the spectrograph slit, mechanical instabilities of the spectrograph and/or thermal variations.

The method was incorporated in Tautenburg as follows. First, it is necessary to find the true intrinsic stellar spectrum of 51 Peg, $I_s(\lambda)$. For this reason we observed a stellar spectrum $I_{s,o}(\lambda)$ with a high signal-to-noise ratio and without a iodine cell. It can be considered as a template stellar spectrum. We get:

$$I_{s,o}(\lambda) = I_s(\lambda) \otimes PSF, \tag{58}$$

where PSF is the instrumental profile function in two-dimensional images, and the symbol $\otimes$ represents convolution. Right after this template observation one spectrum of the hot B star with a iodine cell is observed. Because the B star does not have any absorption lines in the wavelength range covered by iodine absorption lines, the B star light serves only as the light source and we get observed iodine spectrum $I_{I_2,o}(\lambda)$:

$$I_{I_2,o}(\lambda) = I_{I_2}(\lambda) \otimes PSF. \tag{59}$$

$I_{I_2}(\lambda)$ is the true intrinsic iodine spectrum. It was obtained using a iodine cell on the Fourier-Transform Spectrometer (FTS) on the Kitt Peak National Observatory and has a

Table 2: The list of observations of the 51 Peg system. The UT Date is the date of the beginning of each night. A number of observations is the total number of exposures made.

UT Date	N. of obs.	Exp. time (s)	Comment
2007 October 19	6	300	seeing 5 – 6 arcsec
2007 October 21	3	300	high humidity
2007 October 27	1	600	cloudy for most of the night
2007 October 28	3	450	seeing $\sim$ 2 arcsec
2007 October 29	6	600 – 900	cloudy for most of the night
2007 October 30	8	600	seeing $\sim$ 2 arcsec
2007 October 31	2	600	seeing $\sim$ 1.5 arcsec
2007 November 4	2	600	seeing $\sim$ 2.5 arcsec

resolution of 1,000,000. Knowing $I_{I_2,o}(\lambda)$ and $I_{I_2}(\lambda)$ we are able to determine PSF, and then using Eq. (58) we are able to determine $I_s(\lambda)$.

Each stellar spectrum observed with a iodine absorption cell $I_o(\lambda)$ can be written as:

$$I_o(\lambda) = k\,[I_s(\lambda + \Delta\lambda_s) I_{I_2}(\lambda + \Delta\lambda_{I_2})] \otimes PSF, \tag{60}$$

where $\Delta\lambda_s$ and $\Delta\lambda_{I_2}$ are the shifts of the star spectrum and a iodine transmission function. The constant k is proportional to the exposure time of the observation. Knowing $I_s(\lambda)$ from the template stellar spectrum and the FTS iodine spectrum the non-linear least-squares technique is employed to determine $\Delta\lambda_s$, $\Delta\lambda_{I_2}$, k and PSF. The final corrected Doppler shift $\Delta\lambda$ is given by:

$$\Delta\lambda = \Delta\lambda_s - \Delta\lambda_{I_2}. \tag{61}$$

Since the PSF may be a function of a wavelength, the analysis is done on small pieces of spectrum covering typically 2 – 4 Å at all locations over the echelle. Usually there are $\sim$ 120 chunks and the RV is determined in each chunk separately, by solving the Eq. (60). The resulting RV is determined using σ-clipping algorithm. It is worth mentioning that in Tautenburg PSF is modelled via the sum of five displaced Gaussians. The central Gaussian has three free parameters (its width, high and position) and the four satellite Gaussians have two free parameters (their positions). Therefore in each chunk there is in total eight free parameters to be solved – five to determine PSF and then $\Delta\lambda_s$, $\Delta\lambda_{I_2}$ and k.

5.2 Observations and data reduction

In total we got observations for 8 nights out of 14 in October and November 2007 – see Table 2 for the list of observations. We used coudé echelle spectrograph in Thüringer Landessternwarte Tautenburg (TLS) in VIS channel with a iodine cell inserted. The wavelength coverage of VIS channel is 4700 – 7400 Å, but when using a iodine cell the useful

area is only 5000 – 6300 Å due to the limited presence of iodine lines. The slit width was set to $1''.2$, providing a two-pixel resolution of about 67,000. The dispersion was 0.04 Å per pixel, and a resolution in RV ~ 2.2 km s^{-1}.

The Moon could affect observations for all the nights due to the scattered Moon light, unfortunately there is no way to see what effect the Moon light had. The exposure times were chosen so that the signal-to-noise ratio of at least 80 for each spectrum was achieved.

The data were reduced using a pipeline written by E. Guenther with the help of IRAF[4] procedures for overscan correction, bias subtraction, flat-field correction, wavelength calibration and spectral normalisation. The wavelength calibration was done using Thorium-Argon calibration images taken usually before and after the one night of observations.

RVs were computed using the program RADIAL used in Tautenburg based on the solution of Eq. (60) according to the procedure described in section 5.1. The accuracy of our RV measurements was 7 – 24 m s^{-1}, and the mean accuracy 14 m s^{-1} was achieved.

5.3 Results

We used the program FOTEL (Hadrava, 1990, 1998, 2004) to be consistent with the previous analysis (Hrudková & Harmanec, 2006). First we determined the epoch using all RV measurements from Tautenburg and fixed other system parameters according to Hrudková & Harmanec (2006). After the first FOTEL solution we excluded obvious outliers and determined the epoch again. The final RV curve is displayed in Fig. 13 and the resulting epoch is $T = 2454400.8625 \pm 0.0511$ d. Using the ephemeris given by Naef et al. (2004), the resulting $(O-C) = 0.0060 \pm 0.0511$ d. Including this additional value the analysis similar to Hrudková & Harmanec (2006) was done. The $(O-C)$ values were used as an input to FOTEL and two periods presented in Hrudková & Harmanec (2006) were tried in order to confirm or reject any $(O-C)$ variations. The following parameters were allowed to be free during the FOTEL solution: the orbital period, the epoch of periastron, eccentricity, the longitude of periastron and RV semi-amplitude. The resulting parameters were used to compute solutions plotted in Fig. 14.

In Hrudková & Harmanec (2006) we concluded that the interpretation of $(O-C)$ changes in terms of the light-time effect due to a presence of a distant third body can be safely excluded since the semi-amplitude of the $(O-C)$ deviations of $0^{\rm d}.063$ would imply an unrealistically large mass. Therefore, we examined the possibility that 51 Peg is a pulsating star.

If the 250-d period is a beat period of two close oscillations, then the candidate for the second oscillation period is either

$$4^{\rm d}.16032 \ (4^{\rm d}.16^{-1} = 4^{\rm d}.23^{-1} + 250^{\rm d}.00^{-1})$$
$$\text{or } 4^{\rm d}.30373 \ (4^{\rm d}.30^{-1} = 4^{\rm d}.23^{-1} - 250^{\rm d}.00^{-1}).$$

As non-radial pulsations were excluded by Hatzes et al. (1998) due to the lack of the spectral variability, the most likely explanation was that the $4^{\rm d}.23$ period is indeed the

[4]The Image Reduction and Analysis Facility (IRAF) is distributed by the National Optical Astronomy Observatories, which are operated by the Association of Universities for Research in Astronomy, Inc., under cooperative agreement with the National Science Foundation.

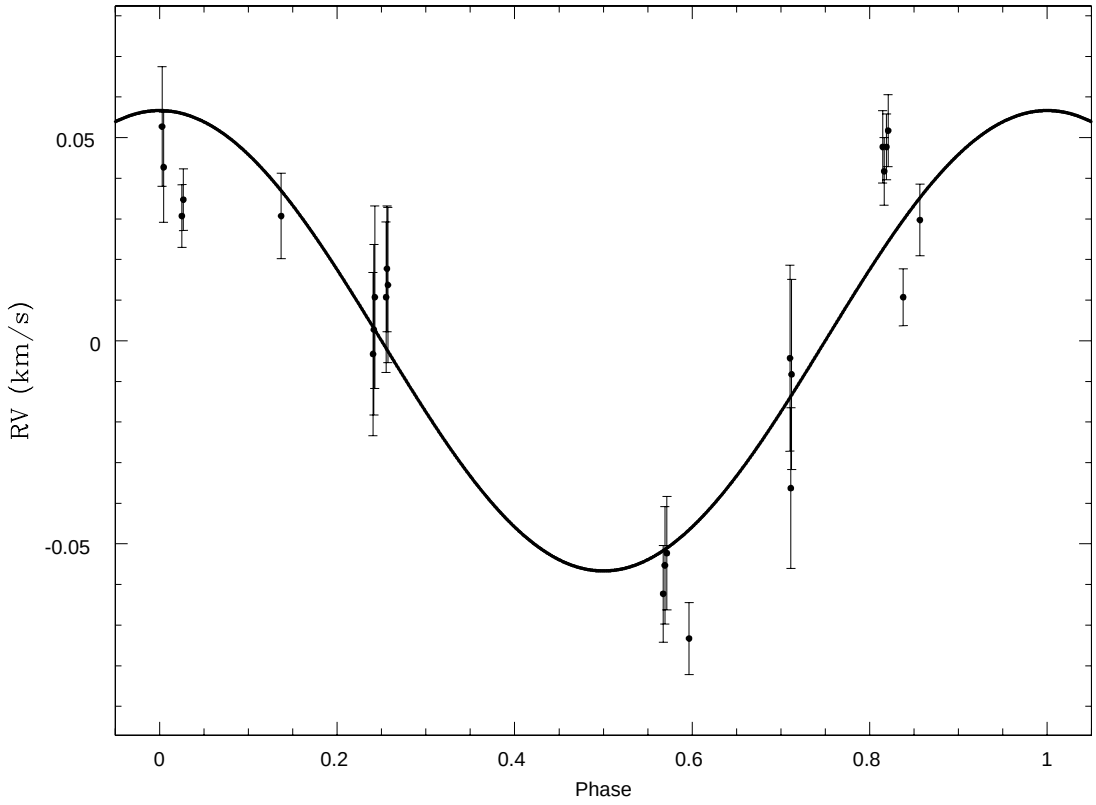

Figure 13: Individual RVs from Tautenburg with their uncertainties overplotted with the theoretical RV curve based on epoch $T = 2454400.8625 \pm 0.0511$ d *and system parameters determined by Hrudková & Harmanec (2006).*

orbital period of a planet and the $4^{\mathrm{d}}.16$ or $4^{\mathrm{d}}.30$ period is a multiple of a synodic period or a forced oscillation. However, combining different RV sets is quite tricky, because the velocity amplitudes can vary between the different sets and all RVs suffer from night corrections different for each instrument and season.

The resulting $(O-C)$ value determined using RVs from Tautenburg is too small to support any expected $(O-C)$ variations. Moreover, for both expected periods $P = 252$ and 829 d the $(O-C)$ from Tautenburg measurements is in a phase where one would not expect $(O-C)$ close to zero in case the signal is real. Summarizing all together, we did not find any evidence supporting the idea presented by Hrudková & Harmanec (2006).

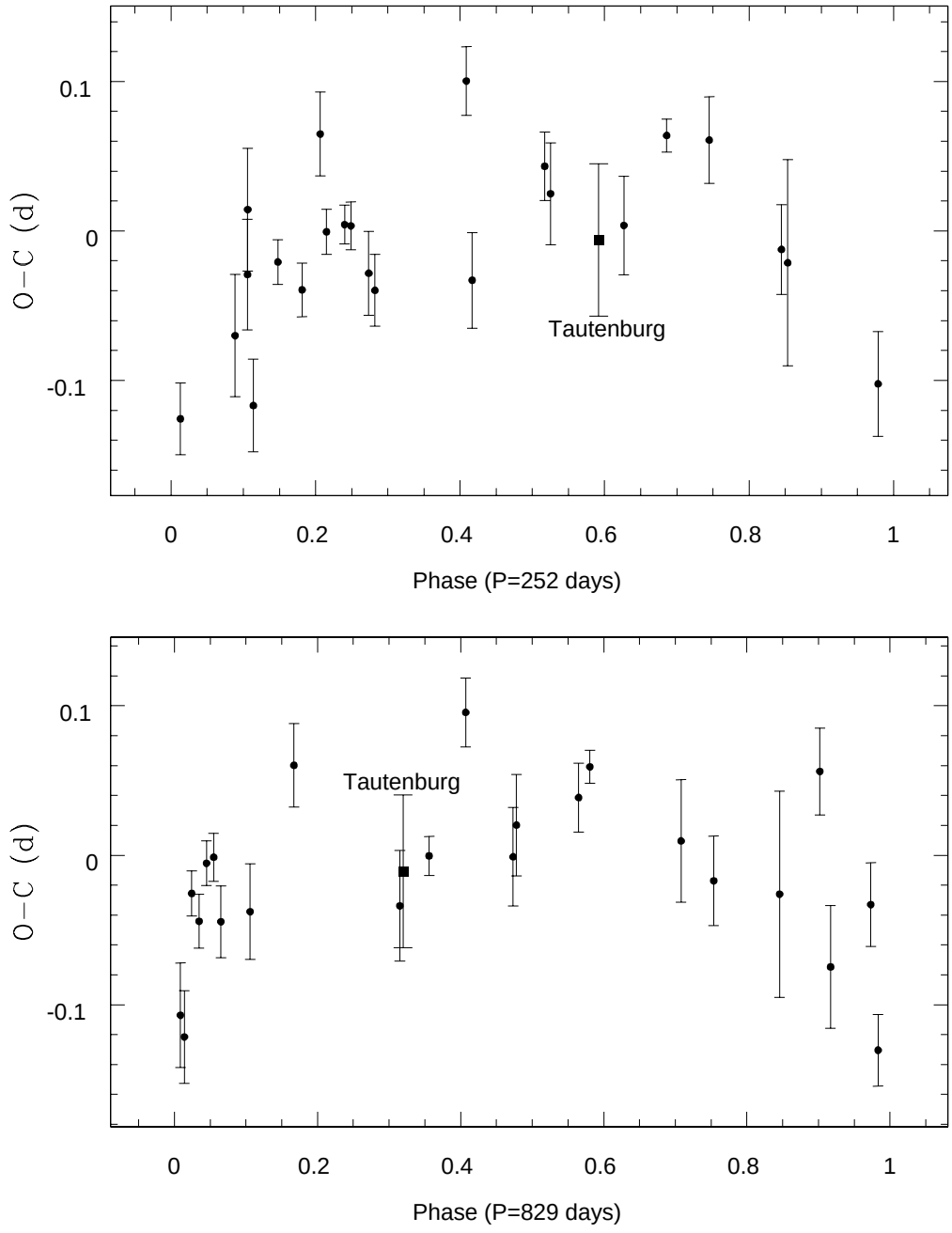

Figure 14: The resulting (O−C) folded using two periods: P=252 (top) and 829 d (bottom). The (O−C) determined using RVs from Tautenburg is displayed with the box symbol.

6 HD 189733

The HD 189733 transiting system is one of the best studied systems from the ground. HD 189733 is a bright star of spectral type K1.5 V with magnitude V=7.67 which is orbited by a transiting Jupiter-mass planet in a period of $\sim$ 2.22 days (Bouchy et al., 2005), and which also has a distant mid-M dwarf binary companion (Bakos et al., 2006a). In 2006 HD 189733 was observed with the *MOST* (Microvariability and Oscillations of STars) satellite and these data were used to search for the existence of other bodies in the system. First, Croll et al. (2007) searched for transits from exoplanets other than the known hot Jupiter, with the result that any additional close-in exoplanets on orbital planes near that of HD 189733b with sizes ranging from about 1.7 – 3.5 $R_\oplus$, where $R_\oplus$ is the Earth radius, are ruled out. Second, an analysis of transit timing variations (TTVs) in these data has been carried out by Miller-Ricci et al. (2008b) who found that there are no TTVs greater than $\pm$45 s, which rules out planets of masses larger than 1 and 4 $M_\oplus$, where $M_\oplus$ is the Earth mass, in the 2:3 and 1:2 inner resonances, respectively, and planets greater than 20 $M_\oplus$ in the outer 2:1 resonance of the known planet and greater than 8 $M_\oplus$ in the 3:2 resonance.

Analyses of transit times similar to Miller-Ricci et al. (2008b) have been carried out for other transiting planetary systems. Steffen & Agol (2005) found no evidence for a second planet in the TrES-1 system, excluding planets down to Earth mass near the low-order, mean-motion resonances of the transiting planet. Similarly, Gibson et al. (2009a) and Gibson et al. (2009b) found no evidence for additional planets down to sub-Earth masses in the interior and exterior 2:1 resonances of the TrES-3 and HAT-P-3 systems.

To measure times of mid-transits with sufficient accuracy to detect terrestrial mass planets requires high quality photometry, free of systematic effects. HD 189733 is known to have surface spots; Pont et al. (2007b) observed two spot events in *HST* data when the flux during the transit changed by 1 and 0.4 mmag. The presence of surface spots on HD 189733 complicates any transit timing analysis (Miller-Ricci et al., 2008b), as discussed in section §4.1.2.

Instrumental effects during transit ingress or egress can also influence the accuracy and determination of transit times. For example, if the transit light curve is not properly normalised so that all data points in egress have a flux level that is slightly too high, the transit time earlier than the correct one will be determined. Correct normalisation is especially problematic for partial transit light curves.

It is also important to have a light curve that is well-sampled during both ingress and egress, because the transit timing information is contained in these parts. When using large telescopes for such a bright star, only short exposure times are needed to get sufficient signal-to-noise and to avoid saturation, and so the cadence of observation is higher. For a given data accuracy, higher cadence leads to more accurately determined transit times.

Table 3: Observations of the HD 189733 system. The UT date is the date of the beginning of each night. The cycle number is in periods from the ephemeris given by Agol et al. (2009). For some nights the exposure time was changed during the observations; this is indicated by the second value in parentheses. The data rms is per exposure for the ratio of intensities of the target and comparison stars. The barycentric mid-transit times of the HD 189733 system are given with uncertainties defined as 68 % confidence limits.

Telescope	UT date	Cycle no.	CCD window (pixels)	Exposure (s)	Data rms (mmag)	Mid-transit time (BJD - 2450000)	$O-C$ (s)	Comment
NOT	2006 July 18	-155	[1040:200]	2.5	2.9	3935.55805 ± 0.00028	38 ± 25	
NOT	2006 August 07	-146	[1040:200]	2.5	2.6	3955.52509 ± 0.00014	26 ± 12	
NOT	2006 August 27	-137	[1040:200]	2.5 (3.0)	2.7	3975.49194 ± 0.00021	-2 ± 18	
WHT	2007 August 17	+23	[1071,546]	10.0	4.6	4330.46305 ± 0.00042	-79 ± 36	
WHT	2007 September 17	+37	[1071,546]	3.0 (3.5)	4.4	4361.52352 ± 0.00044	-43 ± 38	
NOT	2008 June 07	+156	[1040:200]	3.5 (3.0)	2.6	4625.53404 ± 0.00038	-35 ± 33	partial
NOT	2008 June 18	+161	[1040:200]	3.5	2.3	4636.62768 ± 0.00018	31 ± 15	
NOT	2008 July 08	+170	[1040:200]	3.5 (4.0)	2.4	4656.59451 ± 0.00012	1 ± 11	
NOT	2008 July 17	+174	[1040:200]	3.5 (3.0)	3.4	4665.46951 ± 0.00029	62 ± 25	
NOT	2008 July 28	+179	[1040:200]	3.0	2.3	4676.56188 ± 0.00019	18 ± 16	
NOT	2008 August 26	+192	[1655:200]	3.5	2.7	4705.40332 ± 0.00019	15 ± 16	
NOT	2008 September 15	+201	[1655:200]	2.5	2.9	4725.37064 ± 0.00053	28 ± 49	partial

6.1 Observations

We observed eight full and two partial transits of HD 189733 with the 2.6-m Nordic Optical Telescope (NOT), La Palma, Spain, using ALFOSC (the Andalucia Faint Object Spectrograph and Camera), and two full transits using the AG2 camera on the 4.2-m William Herschel Telescope (WHT) of the Isaac Newton Group (ING), La Palma, Spain (Table 3).

ALFOSC has a 2048×2048 back-illuminated CCD with scale 0.19 arcsec/pixel and field of view (FOV) 6.5×6.5 arcmin^2. To reduce the readout time of each exposure and the duty cycle of observation we windowed the CCD with the window sizes summarized in Table 3. We used a Strömgren y filter to minimize effects of colour-dependent atmospheric extinction on the differential photometry and the effect of limb darkening on the transit light curves. We defocused the telescope typically to 3.4 arcsec, spreading the light inside full width at half maximum (FWHM) of the PSF over ~ 250 pixels, in order to minimize the impact of pixel-to-pixel sensitivity variations, and to prevent saturation. Exposure times were chosen to keep counts below 50,000 per pixel to avoid saturation of features such as hot spots and speckles in the defocused stellar images, and to ensure data linearity. The typical exposure time for the NOT data was 3 s (Table 3).

AG2 is a frame-transfer CCD mounted at the folded Cassegrain focus, based on an ING-designed autoguider head. The FOV is 3.3×3.3 arcmin^2 and the scale is 0.4 arcsec/pixel. We used a Kitt Peak R filter and defocused the telescope to 10 and 12 arcsec for the two nights, spreading the FWHM-light over ~ 490 and 700 pixels, respectively. The corresponding exposure times were 10 and 3 s.

The mid-time of each exposure was converted to the BJD using the program BARCOR (see section §3). We use BJD, because for this system the Heliocentric Julian Date would accumulate an error of up to 4 seconds.

6.2 Data reduction

Bias subtraction, flat-field correction and aperture photometry was performed using standard IRAF procedures.

To ensure a signal-to-noise in excess of 1,000 in our Strömgren y-filter flat fields for the NOT data we generated a master flat field for each night using individually weighted normalised flat fields from the entire observing season combined with weights $W = 1-D/S$, where D is the time interval between each night and date of observation, and S is the season length. Applying flat-field corrections has only a minor effect on the resulting NOT photometry, because of the heavily defocused PSF.

We determined master flat fields with a signal-to-noise greater than 1,000 for both WHT nights. However, we identified a position-angle dependent scattered light component in the flat fields, which introduced systematic noise in our WHT photometry. Therefore we did not apply flat-field corrections.

We used the star 2MASS 20003818+2242065 as our comparison star for the WHT data. In our NOT data there are two available comparison stars, 2MASS 20003818+2242065 and 2MASS 20003286+2241118. We found the ratio of their measured intensities varies by a few mmag with time, as the telescope tracks across the meridian. This variation correlates with small drifts in the positions of the stars on the CCD, suggesting that some light is being lost from the aperture around one of the stars due to the wings of the PSF drifting out of that aperture. A similar variation is seen for the ratio of the intensities of 2MASS 20003286+2241118 and out-of-transit HD 189733, but not for 2MASS 20003818+2242065 and HD 189733, suggesting that it is light from 2MASS 20003286+2241118 which is being lost. This star is the farther of the two from HD 189733, and we conclude that the variation in measured intensity is due to a combination of the small drifts in stellar position on the CCD, and the variation of the defocused PSF across the FOV. We therefore used only the comparison star which is closer to HD 189733.

We used circular, equal diameter, photometric apertures for both HD 189733 and the comparison star. A range of aperture sizes was tried and that producing the minimum noise in the out-of-transit data was adopted and fixed during each night. The aperture radius for all stars ranged from 18 – 29 pixels for different NOT nights and the typical FWHM was around 18 pixels (3.4 arcsec). For the two WHT nights the aperture radius was 28 and 30 pixels, respectively, and the corresponding FWHM was 25 and 30 pixels (10 and 12 arcsec).

We ensured the apertures tracked small drifts in the stellar positions on each image by using a large centroiding box of size $4\times$ FWHM. During each night drifts in the stellar positions on the CCD were less than 7 (NOT) and 4 pixels (WHT). The sky background was subtracted using an estimate of its brightness determined within an annulus centred on each star with a width of 10 pixels. For each night, differential photometry was computed by taking the ratio of counts from HD 189733 to the counts from the comparison star. We normalised our data using linear fits that were computed together with other system parameters as described in section §6.3.

The normalised unbinned NOT light curves and binned WHT light curves, averaged into 10-second bins to have the same cadence as the NOT data, are shown in Fig. 15 along with their best-fitting models, residuals and data error bars, as derived in section §6.3.

6.3 Light-curve modelling

To estimate the system parameters we used a parametrized model described in section §4.2. For the NOT data we allowed the limb darkening coefficients to be free parameters, in order to include possible errors in the limb darkening coefficients into our final system parameters and mid-transit times. For the WHT data we adopted values $u_1 = 0.4970$ and $u_2 = 0.2195$ from the tables of Claret (2000) and fixed them in the subsequent analysis. These correspond to the Johnson R filter which has similar characteristics as the Kitt Peak R filter used.

To compute our model we folded all the NOT light curves of full transit except for the night 2008 July 17 which displays obvious systematic changes during transit. In our photometry we cannot easily distinguish spot effects from systematic instrumental errors; to do so would require the instrumental systematic noise to be much less than the predicted spot signatures. We fitted simultaneously planetary and stellar radius, R_p and $R_\star$, respectively, the orbital inclination, i, two limb darkening coefficients, u_1 and u_2, transit time, $T_{0,n}$, and additional two parameters for each night n – the out-of-transit flux, $f_{oot,n}$, and a time gradient, $t_{Grad,n}$. These two parameters were allowed to be free to account for any normalisation errors in the data. For each change of $R_\star$, the stellar mass, $M_\star$, was recomputed using the scaling relation $R_\star \propto M_\star^{1/3}$. We fixed the planetary mass value $M_p = 1.15 \pm 0.04$ M$_\mathrm{J}$ (Bouchy et al., 2005), adopted a period $P = 2.21857503 \pm 0.00000037$ d (Agol et al., 2009), and using Kepler's third law we updated the orbital semi-major axis for each choice of $M_\star$.

We ran MCMC simulations with the Metropolis–Hastings algorithm to estimate the best-fitting parameters and their uncertainties (see section §4.2.2). We added a Gaussian prior placed on $M_\star$ into Eq. (46):

$$\chi^2 = \sum_{i=1}^{N} \left[\frac{f_i(obs) - f_i(theor)}{\sigma_i} \right]^2 + \frac{(M_\star - M_0)^2}{\sigma_{M_0}^2}. \tag{62}$$

Here we adopted the stellar mass $M_0 = 0.82$ M$_\odot$ and its uncertainty $\sigma_{M_0} = 0.03$ M$_\odot$, estimated from stellar spectra by Bouchy et al. (2005). Adding the Gaussian prior on $M_\star$ ensures that errors in the stellar mass, which are the greatest source of uncertainty when deriving the system parameters and transit times, are taken into account.

To estimate appropriate error bars in our data we proceeded as described in section §4.2.4. We assigned the same error bars to all the data points including only Poisson noise. An initial MCMC analysis of the folded NOT light curves was used to estimate the parameters R_p, $R_\star$, i, u_1, u_2, $T_{0,n}$, $f_{oot,n}$ and $t_{Grad,n}$. The first model light curve was used to find the differences between the data and the model for each individual night. Then we rescaled the error bars to satisfy the condition $\chi^2/N_{DOF} = 1.0$, where N_{DOF} is the number

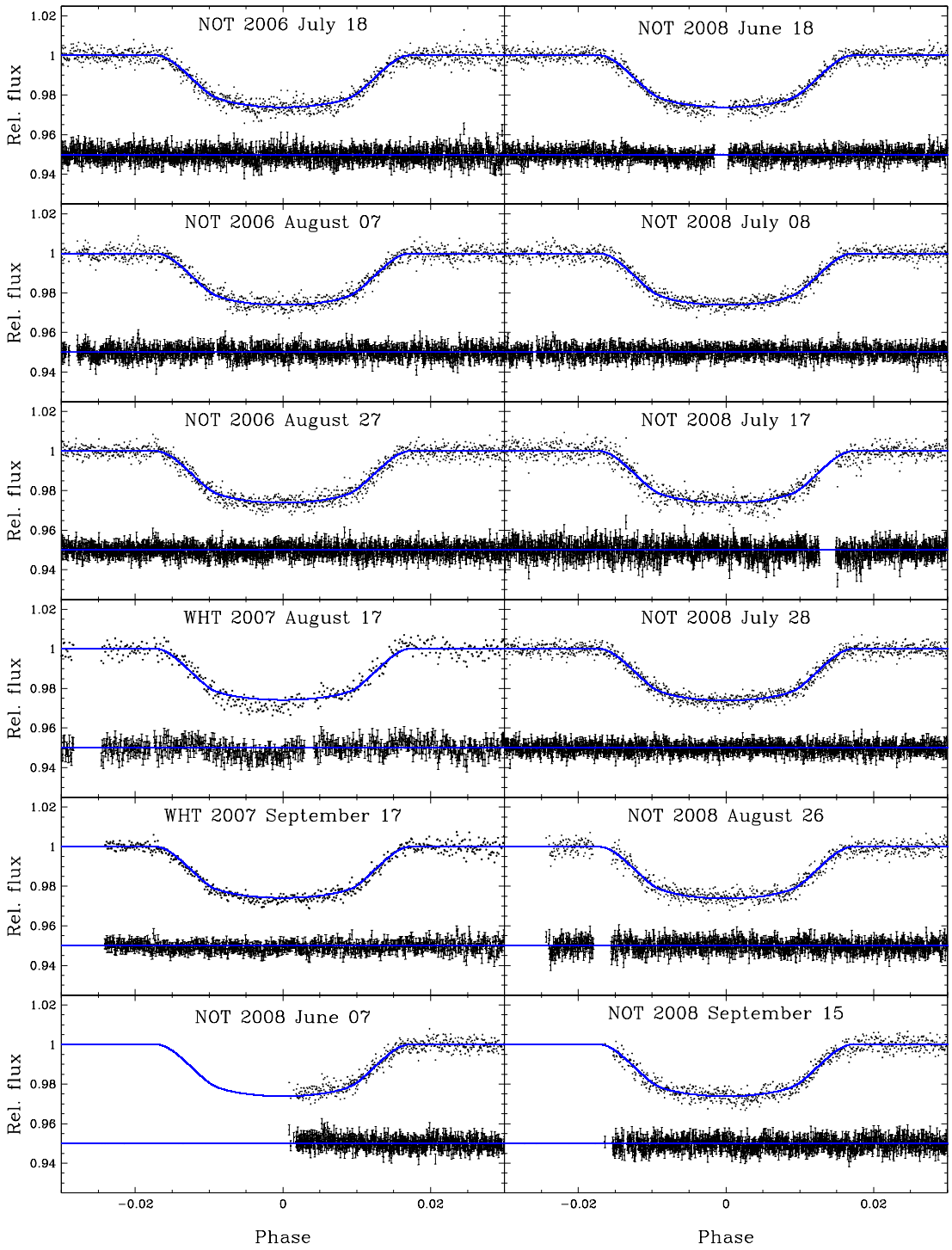

Figure 15: Differential photometry of the HD 189733 system over-plotted with the best-fitting model (solid line) from the MCMC fit. The residuals and 1σ *error bars are also plotted, offset by a constant flux for clarity. The phase was computed using best-fitting transit times presented in Table 3. The photometry for NOT data is unbinned and for WHT is binned in time with 10 second bins to give the similar cadence as for NOT data for clarity.*

of measurements in each light curve. For the night of 2008 July 17, the nights of the two partial transits (2008 June 07 and 2008 September 15) and for the WHT light curves (2007 August 17 and 2007 September 17) we adopted our first model and ran MCMC analysis to find initial parameters T_0, f_{oot} and t_{Grad} for each night independently. Then we rescaled the error bars similarly as before. Compared to the initial model, we found that for the NOT data errors are higher by factors of 2.3 – 3.4 than errors including only Poisson noise, and for the WHT data by factors of 4.6 and 4.4 for the two nights, respectively. The data rms errors per exposure are presented in Table 3. The predicted rms due to photon noise, which is dominated by the fainter comparison star, and to atmospheric scintillation, is ~ 2.5 mmag for the NOT data and ~ 3 mmag for the WHT data.

To create our final model, we proceeded as before but this time including systematic noise in our data according to section §4.2.4 and therefore properly estimating parameter uncertainties. We ran MCMC using the folded NOT light curves and fitting the parameters as described earlier. We created 10 chains, each with length 2,000,000 points in order to achieve convergence. Ultimately, we used our final model to find individual mid-eclipse times and two normalisation parameters for the night of 2008 July 17, the nights of the two partial transits (2008 June 07 and 2008 September 15) and for the WHT light curves (2007 August 17 and 2007 September 17).

6.4 Results

The final system parameters are presented in Table 4 and are consistent within $\sim 2\sigma$ error bars with the previously published values (Bakos et al., 2006b; Pont et al., 2007b; Winn et al., 2007a; Miller-Ricci et al., 2008b). The resulting limb darkening coefficients for the NOT data were $u_1 = 0.46 \pm 0.10$ and $u_2 = 0.35 \pm 0.13$.

The resulting barycentric transit times can be found in Table 3. The uncertainties are defined as 68 % confidence limits. To compute the observed-minus-calculated values ($O-C$) we used the ephemeris given by Agol et al. (2009):

$$T_c(E) = \mathrm{HJD}\,(2454279.436741 \pm 0.000023) + (2\overset{\mathrm{d}}{.}21857503 \pm 0\overset{\mathrm{d}}{.}00000037) \times E. \qquad (63)$$

The resulting $O-C$ residuals together with all the other previously published values (Bakos et al., 2006b; Pont et al., 2007b; Winn et al., 2007a; Miller-Ricci et al., 2008b; Knutson et al., 2009) are plotted in Fig. 16. Our observations did not bring any refinement of the ephemeris and we confirm that presented by Agol et al. (2009). For the night 2006 August 07 a transit timing measurement of HD 189733 was also presented by Miller-Ricci et al. (2008b) from the *MOST* data and it is consistent within 2σ error bars with our measurement.

6.4.1 Transit timing variations analysis

The mean $O-C$ for all our observations which span more than two years is 5 ± 38 s, where the quoted error is the rms scatter in the $O-C$ values and is slightly larger than the average $O-C$ uncertainty ~ 25 s. None of our $O-C$ measurements is a significant outlier.

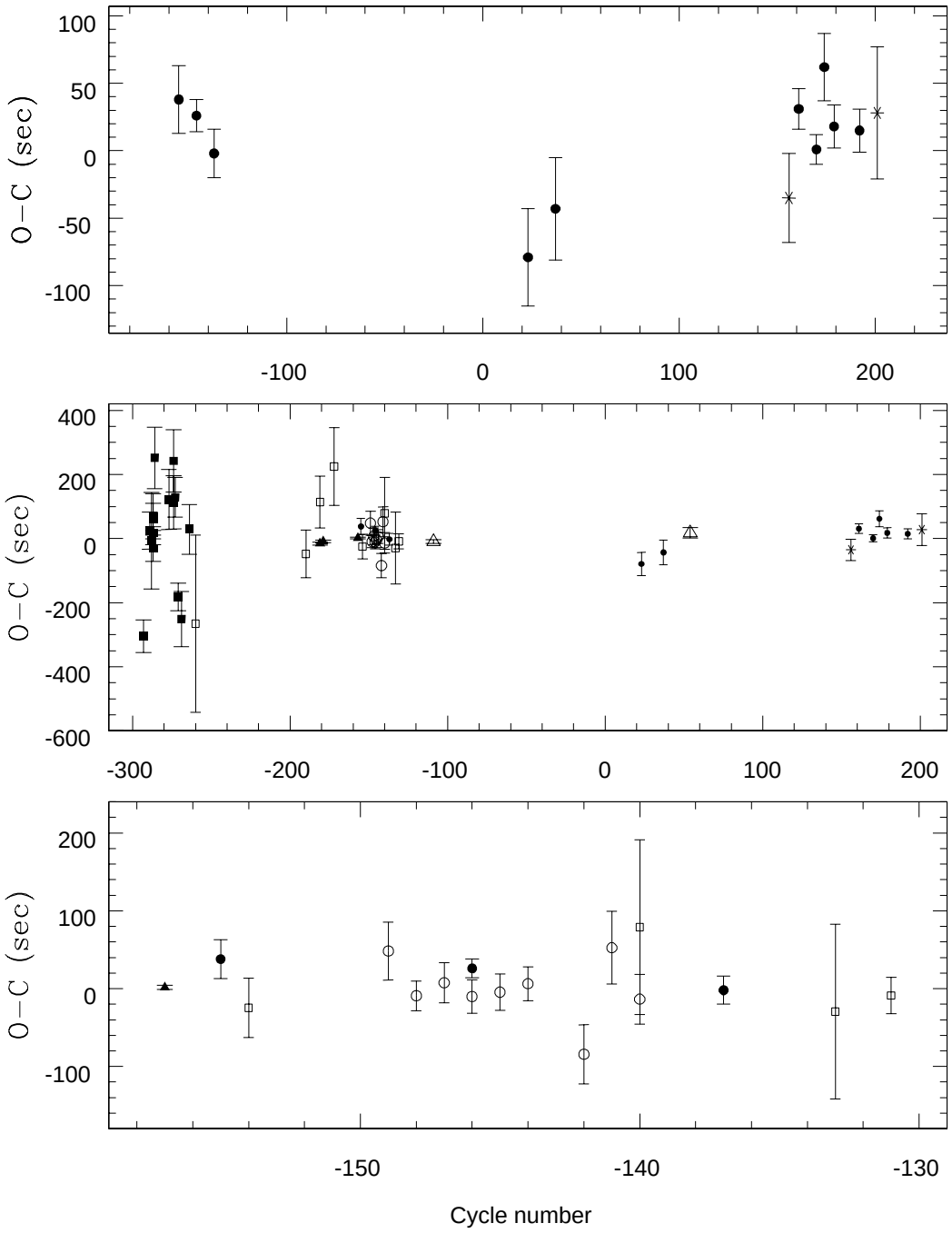

Figure 16: Top: NOT and WHT $O-C$ residuals of mid-transit times of the HD 189733 system including both partial (star symbol) and full transits (filled circle symbol). Middle: Previously published values plotted together with NOT and WHT results. Filled squares: Bakos et al. (2006b), ground-based; filled triangles: Pont et al. (2007b), HST; open squares: Winn et al. (2007a), ground-based; open circles: Miller-Ricci et al. (2008b), MOST; open triangles: Knutson et al. (2009), Spitzer; filled circles and stars: this work. Bottom: The same as the middle but zoomed for clarity. The cycle number is in periods from the ephemeris given by Agol et al. (2009). Our timing measurements are the most accurate from known ground-based observations of the system.

Table 4: System parameters of HD 189733. The uncertainties are 68 % confidence limits.

Parameter	**Symbol**	**Value**	**Units**
Planet radius	R_p	1.142 ± 0.014	R_J
Star radius	$R_\star$	0.755 ± 0.009	$R_\odot$
Orbital inclination	i	85.70 ± 0.03	deg
Planet/star radius ratio	ρ	0.1556 ± 0.0027	
Total transit duration	T_d	1.807 ± 0.023	h
Impact parameter	b	0.667 ± 0.009	

The two largest $O-C$ values for the nights 2007 August 17 and 2008 July 17 coincide with obvious systematic changes during the transit (see Fig. 15) and both have the same or larger uncertainty than the average value. Therefore the rms scatter in the $O-C$ values of 38 s is a good estimate for placing limits on the presence of other planets in the system.

This conclusion was used to place mass limits on the existence of planets on orbits interior and exterior to HD 189733b. First, the mass, semimajor axis and eccentricity of the putative perturbing planet was selected. The orbital inclination was set so that HD 189733b and the perturbing planet have coplanar orbits. The two-planet system was then numerically integrated by D. Nesvorný using the Bulirsch-Stoer integrator (Press et al., 1992). He determined all mid-transit times of HD 189733b over a time-span of 500 days, an interval long enough to cover at least 14 orbits of all perturbing planets we can exclude, and used these data to estimate TTVs. The mass, initial semimajor axis and initial eccentricity of the perturbing planet were varied to determine the TTV amplitude for different planetary configurations.

Fig. 17 shows the range of the inner and outer planet's orbits that produce TTVs smaller/larger than ±38 s and are thus compatible/incompatible with our TTV observations of the HD 189733 system. The shaded area in Fig. 17 excludes a range of possible eccentricities and semimajor axes for a putative 1 Earth-mass (top) and 2 Earth-masses (bottom) inner (left) and outer (right) planet in the system. Our observations of the HD 189733 system show no evidence for the presence of planets down to 1 Earth mass in the 2:1, 3:2 and 5:3 exterior resonance orbits, planets down to 1 Earth mass in the 1:2, 1:3, 2:3 and 2:5 interior resonance orbits, and planets down to 2 Earth masses in the 1:4 interior resonance orbit with HD 189733b. However, not all of these resonant orbits are Hill stable. We computed Hill stability according to Eq. (21) of Gladman (1993) for both inner and outer perturbing planet and displayed the result in Fig. 17 using thin solid line. For the inner/outer perturbing planet all the orbits on the left/right to the thin solid line are Hill-stable, which means that close approaches between two planets are forbidden. For the rest of the parameter space the Hill stability of the system is unknown; the system still may be Hill-stable.

Nesvorný (2009) showed that the TTV signal can be significantly amplified for planetary systems with substantial orbital inclinations of the transiting and perturbing planet and/or in the case of transiting planet in an eccentric orbit with an anti-aligned orbit of the

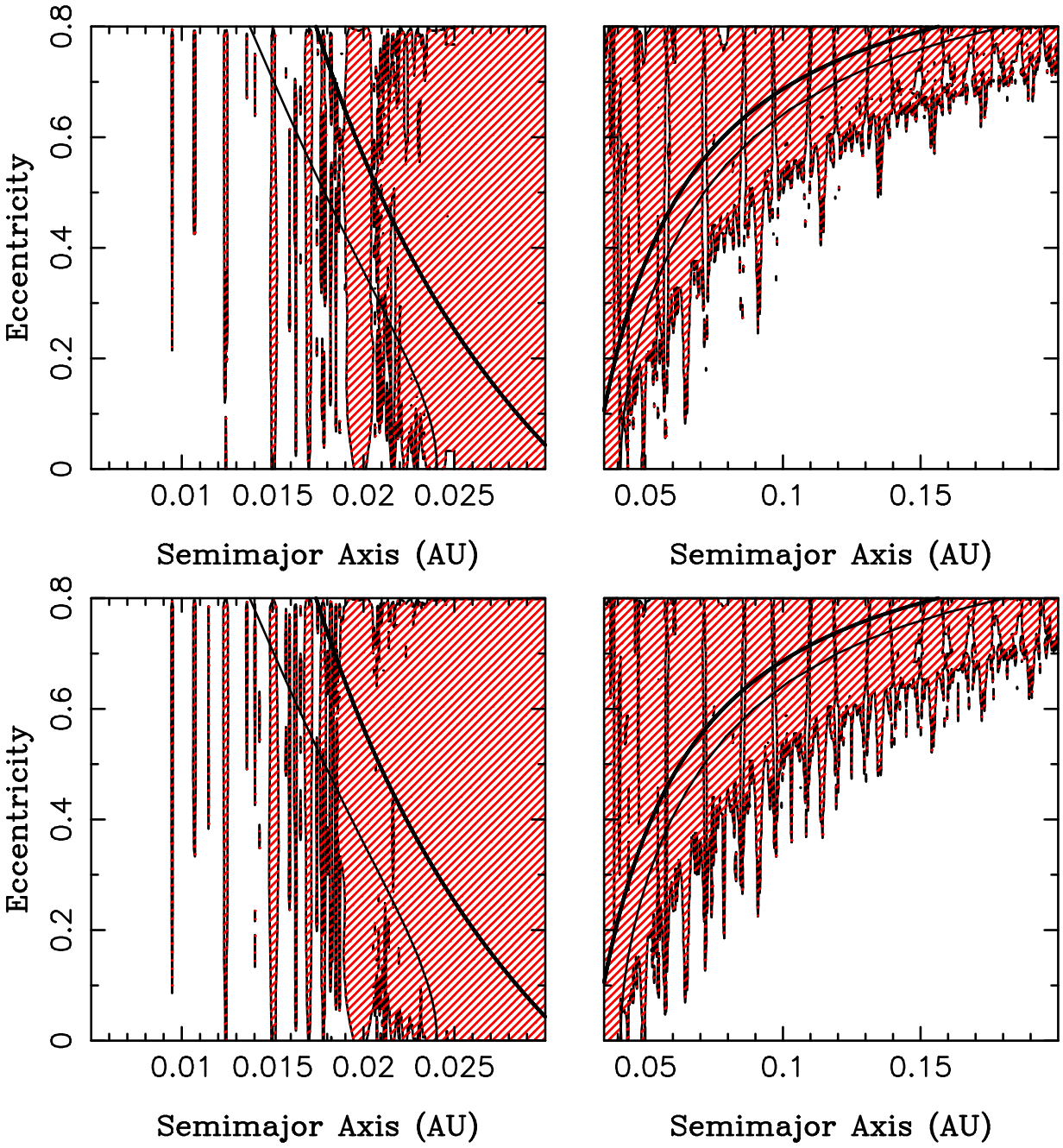

Figure 17: A numerical survey of the HD 189733 system showing 38-s TTVs caused by an inner (left plots) and outer (right plots) 1 Earth-mass planet ($m_2 = 3 \times 10^{-6}$ $M_\odot$, top) and 2 Earth-masses planet ($m_2 = 6 \times 10^{-6}$ $M_\odot$, bottom) was carried out by D. Nesvorný. The shaded area excludes a range of possible eccentricities and semimajor axes for a putative 1 and 2 Earth-masses inner/outer planet in the system based on our observational non-detection of TTVs greater than ± 38 s. *We do not display plots for Jupiter-mass planets as these would easily be detected in radial velocity searches. The thick solid line shows a boundary where a collision between the two planets can occur. It is defined so that the apocentre/pericentre of the inner/outer perturbing planet equals to the semi-major axis of the transiting planet. The thin solid line represents a Hill stability computed according to Gladman (1993). Credit Nesvorný.*

perturbing planetary companion. Therefore for most orbital architectures of exoplanetary systems we determine the perturber's upper mass from our TTVs under the assumption of coplanar orbits of transiting and perturbing planets.

Madhusudhan & Winn (2009) found an upper limit of 22 $M_\oplus$ for a Trojan in the HD 189733 system. In addition, Croll et al. (2007) searched for Trojan transits in *MOST* photometry, assuming similar inclinations of the Trojan's and transiting planet's orbits, and concluded that Trojans with a radius above 2.7 $R_\oplus$ should have been detected with 95 % confidence. Using a mean density of $\rho \sim 3\,000$ kg m^{-3}, this corresponds to 11 $M_\oplus$. Our TTVs show no evidence for Trojans with masses higher than 5.3 $M_\oplus$ if their libration amplitudes are similar as for Trojans orbiting near the Sun-Jupiter Lagrange points (Ford & Holman, 2007).

Kipping (2009) predicted TTV amplitude of 1.51 s and TDV amplitude of 2.94 s for an Earth-mass exomoon in a circular orbit about HD 189733b. Increasing the eccentricity of the moon's orbit decreases TTV amplitude, but increases TDV amplitude. However, for the HD 189733 system these variations are too small to be detectable in our data.

6.5 Conclusions and discussion

Miller-Ricci et al. (2008b) found no TTVs greater than ±45 s in *MOST* data, and excluded super-Earths of masses larger than 1 and 4 $M_\oplus$ in the 2:3 and 1:2 inner resonance, respectively, and planets greater than 20 $M_\oplus$ in the outer 2:1 resonance of the known planet and greater than 8 $M_\oplus$ in the 3:2 resonance. Miller-Ricci et al. (2008b) assumed that the orbit of the perturbing planet is circular and that additional planets in eccentric orbits would produce stronger perturbations. However, Nesvorný (2009) showed that an eccentric planet can produce stronger or weaker perturbations depending on the relative angular position of its orbital pericentre. Therefore we did not assume the circular orbit for the perturbing planet and our approach is more rigorous.

Our observations of the HD 189733 system spanning more than two years show no evidence for the presence of planets down to 1 Earth mass in the 2:1, 3:2 and 5:3 exterior resonance orbits, planets down to 1 Earth mass in the 1:2, 1:3, 2:3 and 2:5 interior resonance orbits, and planets down to 2 Earth masses in the 1:4 interior resonance orbit with HD 189733b. Our results place the strongest limits to date on the presence of other planets in this system. We also discuss the possible presence of Trojans in the system, and conclude that the highest limit on a Trojan mass is 5.3 $M_\oplus$ if its libration amplitude is similar as for Trojans orbiting near the Sun-Jupiter Lagrange points.

7 TrES-1

Alonso et al. (2004) reported a detection of a transiting Jupiter-sized planet orbiting TrES-1, a relatively bright (V=11.79 mag) K0 V star. First TTV analysis of this system was carried out by Steffen & Agol (2005), who analysed the set of transit times given in Charbonneau et al. (2005). They found no evidence for a second planet in the system, and excluded planets down to Earth mass near low-order, mean-motion resonances with the transiting planet. In 2006 Winn et al. (2007b) used KeplerCam on the 1.2-m telescope at the Fred L. Whipple Observatory (FLWO) on Mt. Hopkins, Arizona. They observed three full transits of TrES-1 and improved the ephemeris given by Alonso et al. (2004). Another full transit observation was reported by Narita et al. (2007) together with measurements of the Rossiter-McLaughlin effect from the RV curve. Three transits of Winn et al. (2007b) and one of Narita et al. (2007) show the possible TTV trend, which led us to observe TrES-1 in 2007. The results were reported by Hrudková et al. (2009). In this section, we present a new analysis of 2007 data together with data taken in 2006.

Rabus et al. (2009) presented features on light curves of the TrES-1 system that can be explained by the presence of star spots on TrES-1 surface or a second transiting planet in the TrES-1 system. If TrES-1 is an active star the light curve can be distorted if the planet transits in front of a spot or due to intrinsic variability of the star. In case a second transiting planet is present in the TrES-1 system, the light curve is affected if the two transiting planets have the same or similar orbital inclination and one transits the other. The system parameters and derived mid-eclipse times can then be affected by an inappropriate fitting model. Dittmann et al. (2009) published a tentative detection of a starspot on TrES-1 during two consecutive transits and concluded that the brightening anomalies they observed are unlikely due to a double transiting planet as suggested by Rabus et al. (2009).

Gillon et al. (2008) presented several well known 'rules of thumb' for an accurate differential CCD photometry. Their main points for observational and reduction strategy are following:

1. The good basic calibration of raw images is important. A major issue is the quality of flat fields.
2. Good choice of a reduction method is essential.
3. In order to minimize an effect of inter-pixel variability, it is required to keep stars at the same pixel positions during observations, therefore a good guiding is necessary.
4. It is important to choose properly an optimal pointing because a flux of reference stars is a key factor in a differential photometry.
5. One should properly estimate sources of a noise in order to optimize the duty-cycle of observations.

In addition to Gillon et al. (2008) we present new 'rules of thumbs' in section §7.2.1 based on our data analysis.

Table 5: Observations of the TrES-1 system. The UT date is the date of the beginning of each night. The cycle number is in periods from the epoch given by Eq. (65). The data rms is per exposure for the ratio of intensities of the target and comparison stars. The barycentric mid-transit times are given with uncertainties defined as 68 % confidence limits.

Instr.	UT Date	Cycle	Exp. (s)	No. Comp.	Data rms (mmag)	Mid-transit time (BJD)	$O-C$ (s)	Comment
AG3	2006 May 12	-9	1	3	3.5	$2453868.57234 \pm 0.00027$	3 ± 23	
AG3	2006 May 15	-8	1	3	3.5	$2453871.60224 \pm 0.00035$	-12 ± 30	
AG3	2006 May 18	-7	1	1	3.0	$2453874.63263 \pm 0.00037$	15 ± 32	
AG3	2006 August 08	+20	1	1	3.4	$2453956.44553 \pm 0.00023$	94 ± 20	
AG3	2006 August 11	+21	1	1	2.5	$2453959.47530 \pm 0.00044$	67 ± 38	CCD problem
AG2	2007 September 12	+152	5	3	2.3	$2454356.41480 \pm 0.00037$	55 ± 32	
AG2	2007 September 15	+153	10	1	1.6	$2454359.44415 \pm 0.00045$	-8 ± 39	
AG2	2007 September 18	+154	10	1	1.5	$2454362.47360 \pm 0.00027$	-62 ± 23	

7.1 Observations

We observed eight full transits of TrES-1 with frame-transfer CCDs AG2 and AG3 on the 4.2-m William Herschel Telescope (WHT) of the Isaac Newton Group (ING), La Palma, Spain (Table 5). Five transits were observed in 2006 and three transits in 2007. AG3 and AG2 are ING-designed autoguider heads with E2V CCD, the field of view 3.3×3.3 arcmin^2 and the scale 0.4 arcsec/pixel.

AG3 is mounted at the Nasmyth focus of the WHT. During observations it was not possible to guide and therefore drifts in the stellar positions on the CCD were 10 – 20 pixels. We used a Wratten 25 R filter to minimize colour-dependent atmospheric extinction on the differential photometry and an effect of limb-darkening on transit light curves. The FWHM of stellar images ranged from 4 – 7 pixels. The exposure time for all images was 1 second.

AG2 is mounted at the folded Cassegrain focus of the WHT. Autoguiding ensured that during each night drifts in the stellar positions on the CCD were less than 3 pixels. We used a Kitt Peak R filter. We defocused the telescope typically to 4 arcsec, spreading the FWHM-light over more than 300 pixels, in order to minimize the impact of pixel-to-pixel sensitivity variations, and to prevent saturation. We acquired 5 and 10 second exposures (Table 5).

The mid-time of each exposure was converted to BJD using the program BARCOR (see section §3).

7.2 Data reduction

Bias subtraction, flat-field correction and aperture photometry was carried out using standard IRAF procedures.

We applied a master flat field created for each night separately to the AG3 data. For the AG2 data we did not apply flat-field corrections due to a position-angle dependent scattered light component, which introduced noise in our photometry.

In order to include all the stellar light into the aperture we ensured the apertures tracked drifts in the stellar positions on each image by using a large centroiding box of size $4 \times$ FWHM.

A differential photometry was obtained using circular apertures. Different aperture sizes were tried; that producing the minimum noise in the out-of-transit data was adopted and fixed during each night. For the AG3 data the aperture radius ranged from 18 – 29 pixels for TrES-1, and 13 – 19 pixels for the comparison stars. We included the nearby faint stars into the aperture of TrES-1. The brightest star included is ~ 5 mag fainter than TrES-1, and as we did not see any influence on the resulting light curves, we assumed all the light coming from TrES-1 itself. For the AG2 data we used circular, equal diameter, photometric apertures for both TrES-1 and the comparison stars. The aperture radius was 30, 29 and 29 pixels for the three nights, respectively. Our comparison stars were 2MASS J19041058+3638409, 2MASS J19040934+3639195 and 2MASS J19040792+3640116. It was 2MASS J19041058+3638409 when only one comparison star was used for a differential photometry (see Table 5 and section §7.2.1). The sky background was subtracted using an estimate of its brightness determined within an annulus centred on each star with a width of 5 – 10 pixels. For each night, a differential photometry was obtained by taking the ratio of counts from TrES-1 to the mean counts (the counts) from the comparison stars (the comparison star). The light curves were normalised using a polynomial function of low degree (up to third degree).

The normalised light curves, averaged into 0.5-minute bins for clarity, are shown in Fig. 19 along with their best-fitting models, residuals and data error bars, as derived in section §7.3.

7.2.1 Photometry

To obtain an accurate photometry a master bias reproducing correctly bias level changes and a good quality master flat field is needed. If the bias is not subtracted from an image thoroughly, a residual bias, $\delta_{\text{bias}(x,y)}$, is left and the de-biased flat-fielded image is:

$$I(x,y) = T(x,y) + B(x,y) + \frac{\delta_{\text{bias}(x,y)}}{QE(x,y)}. \tag{64}$$

Here $I(x,y)$ is the image, $T(x,y)$ is a target, $B(x,y)$ is a background and $QE(x,y)$ is a quantum efficiency, all quantities depending on spatial coordinates x and y on the CCD. Provided the bias error is constant, that is $\delta_{\text{bias}(x,y)} = constant(x,y)$, and quantum efficiency is flat, the effect of the residual bias should be taken out in the background subtraction when performing a differential photometry. On the other hand, if the background changes, that is $\delta_{\text{bias}(x,y)} \neq constant(x,y)$, a differential photometry can be affected.

In our differential photometry we identified features with sizes of up to few mmag lasting for up to few tens of minutes. To verify if these features could be caused by background changes, we summed all images over the typical feature duration to get a high signal-to-noise image. These 'superflat' images were then compared and we concluded that we do not see background changes big enough to explain features with sizes of up to few mmag.

In addition to short time-scale features, slow variations are evident for nearly all transits. An example can be seen in Fig. 18, where we display a photometry for the AG3 night 2006 August 11. A different raw flux behaviour of different comparison stars is obvious. Particularly, the comparison star No. 1 (2MASS J19041058+3638409), the closest to TrES-1 on the CCD, has a different raw flux course during the night than comparison stars No. 2 and 3 (2MASS J19040934+3639195 and 2MASS J19040792+3640116), which are on the other half of the CCD than TrES-1. The ratio of fluxes of comparison stars No. 2 and 3 is flat, therefore we can rule out a variability of these two stars. We rule out the variability of the comparison star No. 1 as we did not see any signs of variability on any of the nights. However, the ratio of fluxes of the comparison star No. 1 to comparison stars No. 2 and 3 is not constant and the change corresponds to a mount position angle (MNTPA) of the field rotator.

In Fig. 18 we plot vertical lines when changes in the photometry coincide with drifts in the stellar positions. When the field shifts on the CCD, it implies a movement of the beam relative to reflecting surfaces in a light path. This may induce small changes in the measured relative brightness of two stars, if there is a flexure of the light inside the optical system. In case of AG3, both short and long-term systematics can be explained by a combination of optical imperfections of a field rotator consisting of five optical elements, two lenses and three mirrors formed in a K-shape, and the drifts in stellar positions during the night. We used only one comparison star for our differential photometry when different comparison stars had different flux behaviour (see Table 5).

Based on our experience, we recommend additional 'rules of thumb' to these of Gillon et al. (2008):

1. Field rotator is needed for instruments on telescopes with an altazimuth mount. To avoid rotator optical imperfections instruments on telescopes with an equatorial mount should be preferred.

2. To avoid a use of mirrors with a non-uniform reflectivity over the surface instruments placed in a direct Cassegrain focus should be favoured.

7.3 Light-curve modelling

To estimate mid-transit times we used a parametrized model described in section §4.2. We adopted a stellar mass $M_\star = 0.89 \pm 0.05$ $M_\odot$ and a planetary mass $M_p = 0.76 \pm 0.05$ M_J, estimated from stellar spectra by Sozzetti et al. (2004). We assumed a period $P = 3.0300737 \pm 0.0000026$ d (Winn et al., 2007b) and using Kepler's third law we computed and in a subsequent analysis fixed the orbital semi-major axis.

We did not find any suitable tabulated limb darkening coefficients for the Wratten 25 R filter. We used values $a = 0.28$ and $b = 0.21$ (see below). For AG2 data we used $a = 0.4396$ and $b = 0.2598$ from the tables of Claret (2000), corresponding to the Johnson R filter which has similar characteristics as the Kitt Peak R filter used.

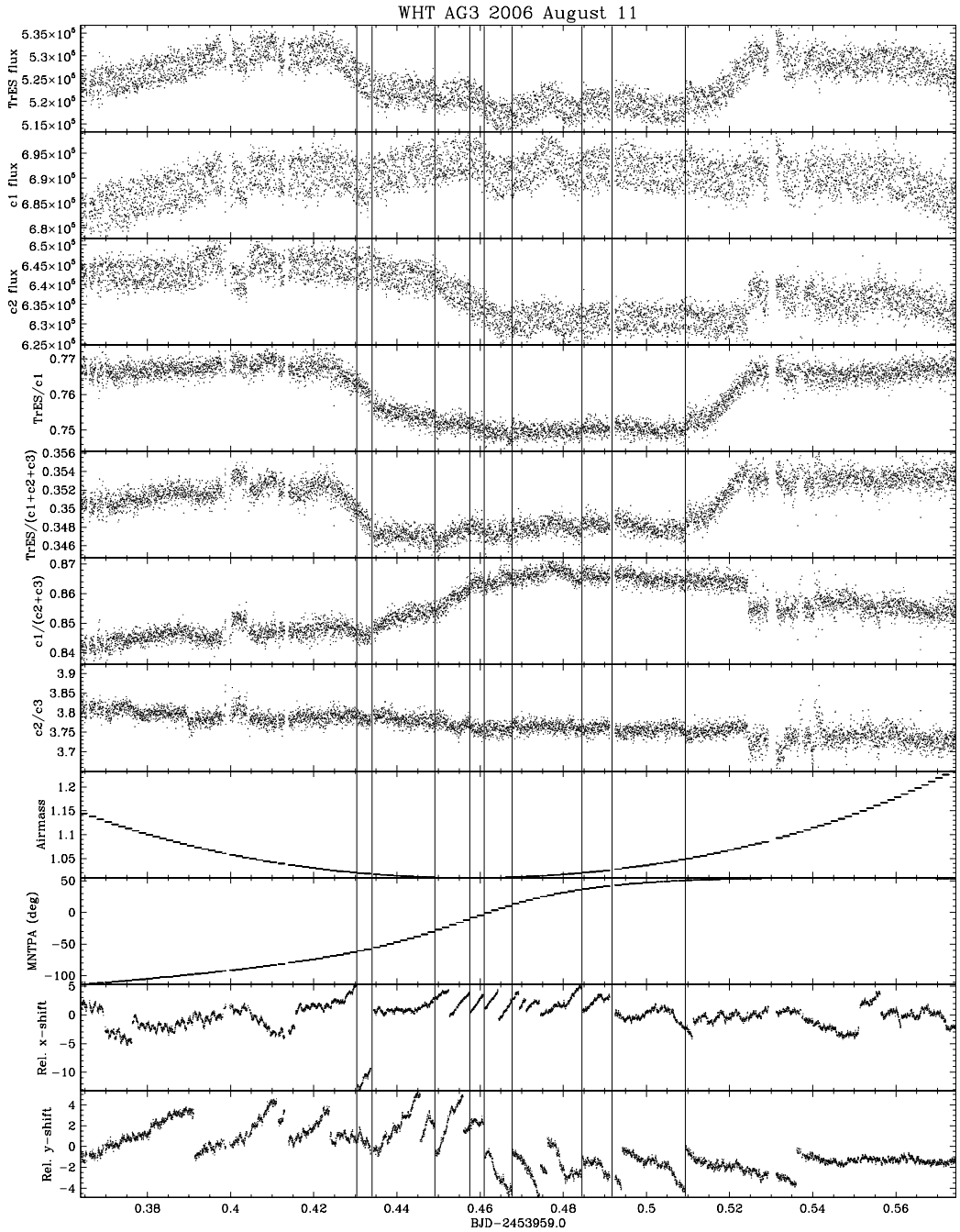

Figure 18: Photometry for the night 2006 August 11. From top to bottom: raw flux of TrES-1, comparison star No. 1 (2MASS J19041058+3638409), comparison star No. 2 (2MASS J19040934+3639195), relative flux of TrES-1 to comparison star No. 1, relative flux of TrES-1 to flux of all three comparison stars, relative flux of comparison star No. 1 to No. 2 and 3, relative flux of comparison star No. 2 to 3, airmass, mount position angle (MNTPA) and drifts in the stellar positions on CCD during the night. We plot vertical lines when changes in the photometry coincide with drifts in the stellar positions (see section §7.2.1 for an explanation).

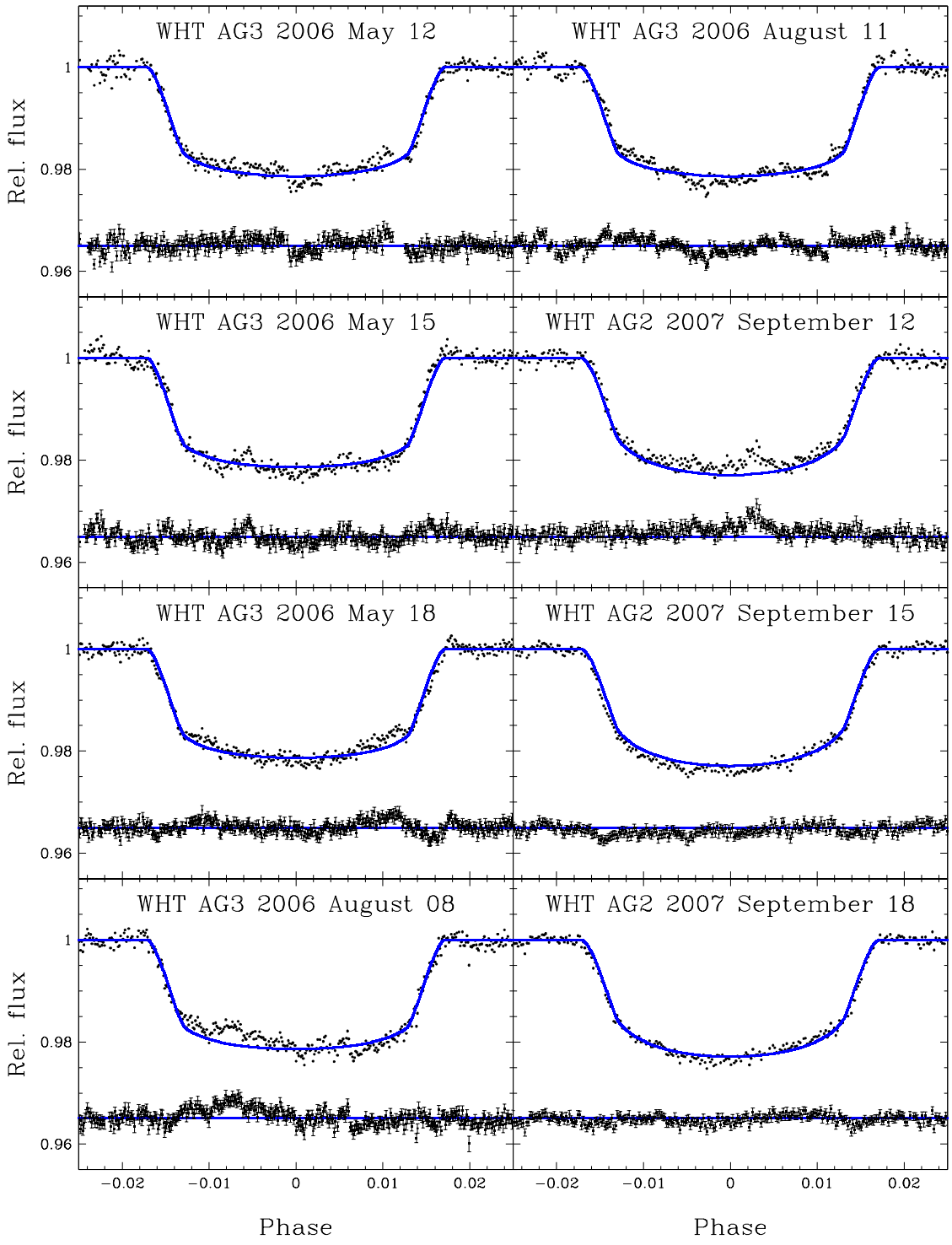

Figure 19: Differential photometry of the TrES-1 system. WHT AG3 and AG2 light curves of the TrES-1 system after binning in time with 0.5 minute bins are over-plotted with the best-fitting model (solid line) from the MCMC fit. The residuals and 1σ *error bars are also plotted, offset by a constant flux for clarity. The phase was computed using best-fitting transit times presented in Table 5.*

We ran MCMC simulations with the Metropolis–Hastings algorithm as described in section §4.2.2 to estimate the best-fitting mid-transit times and their uncertainties. The scale factors were chosen so that $\sim 43-46\,\%$ of parameter sets were accepted.

We used system parameters derived by Winn et al. (2007b) to create our model light curve. Initially we fitted limb darkening coefficients for our AG3 data, as we did not find any suitable tabulated values for the Wratten 25 R filter. Unfortunately, data were not of a quality sufficient to fit a and b independently, and generated chains did not converge. We used values $a = 0.28$ and $b = 0.21$ for z band filter presented by Winn et al. (2007b). However, the light-curve shape is very sensitive to a choice of limb darkening coefficients, which in turn has the influence on the derived mid-transit times. Therefore we computed mid-transit times for few different values of limb darkening coefficients, and found differences between new and originally derived times of up to 8 seconds. We accounted for this error in the resulting transit time uncertainties presented in Table 5.

To account for any normalisation errors in the data we allowed the parameters of the polynomial function to be free in our MCMC simulations. However, except of the night 2006 May 18, the chains did not converge ($R(x) < 21$; see section §4.2.3). Thus the only free parameter in the subsequent analysis was the mid-transit time for each night and two parameters of the linear fit for the night 2006 May 18, the out-of-transit flux, $f_{oot,n}$, and a time gradient, $t_{Grad,n}$.

To estimate appropriate error bars in our data we proceeded as in section §4.2.4. Compared to the model we found that errors are higher by factors of 1.5 – 2.3 for AG2 and 2.5 – 3.5 for AG3 than errors including only Poisson noise. The data rms errors per exposure are presented in Table 5 and due to the presence of systematic errors they are higher by 0.5 – 1.5 mmag than errors expected from predicted sources of noise.

7.4 Results

The resulting barycentric transit times can be found in Table 5. The uncertainties are 68 % confidence limits plus errors accounting for a priori choice of limb darkening coefficients. To compute the observed minus calculated values ($O-C$) we used the epoch given by Winn et al. (2007b):

$$T_c(E) = \mathrm{HJD}\,(2453895.84297 \pm 0.00018) + (3\overset{\mathrm{d}}{.}0300737 \pm 0\overset{\mathrm{d}}{.}0000026) \times E. \qquad (65)$$

The resulting $O-C$ residuals together with all the other previously published values (Charbonneau et al., 2005; Narita et al., 2007; Winn et al., 2007b) are plotted in Fig. 20.

Using our data and the data by Charbonneau et al. (2005), Narita et al. (2007) and Winn et al. (2007b)[5] we are able to determine the most accurate ephemeris to date. We fitted a weighted linear fit to the transit times as a function of epoch where weights were inversely proportional to the squares of rms errors of individual transit times. Our ephemeris is:

$$T_c(E) = \mathrm{HJD}\,(2453895.84327 \pm 0.00011) + (3\overset{\mathrm{d}}{.}0300727 \pm 0\overset{\mathrm{d}}{.}0000012) \times E. \qquad (66)$$

[5]We excluded the same 2 timing measurements as Winn et al. (2007b) that were based on observations of only part of the transit.

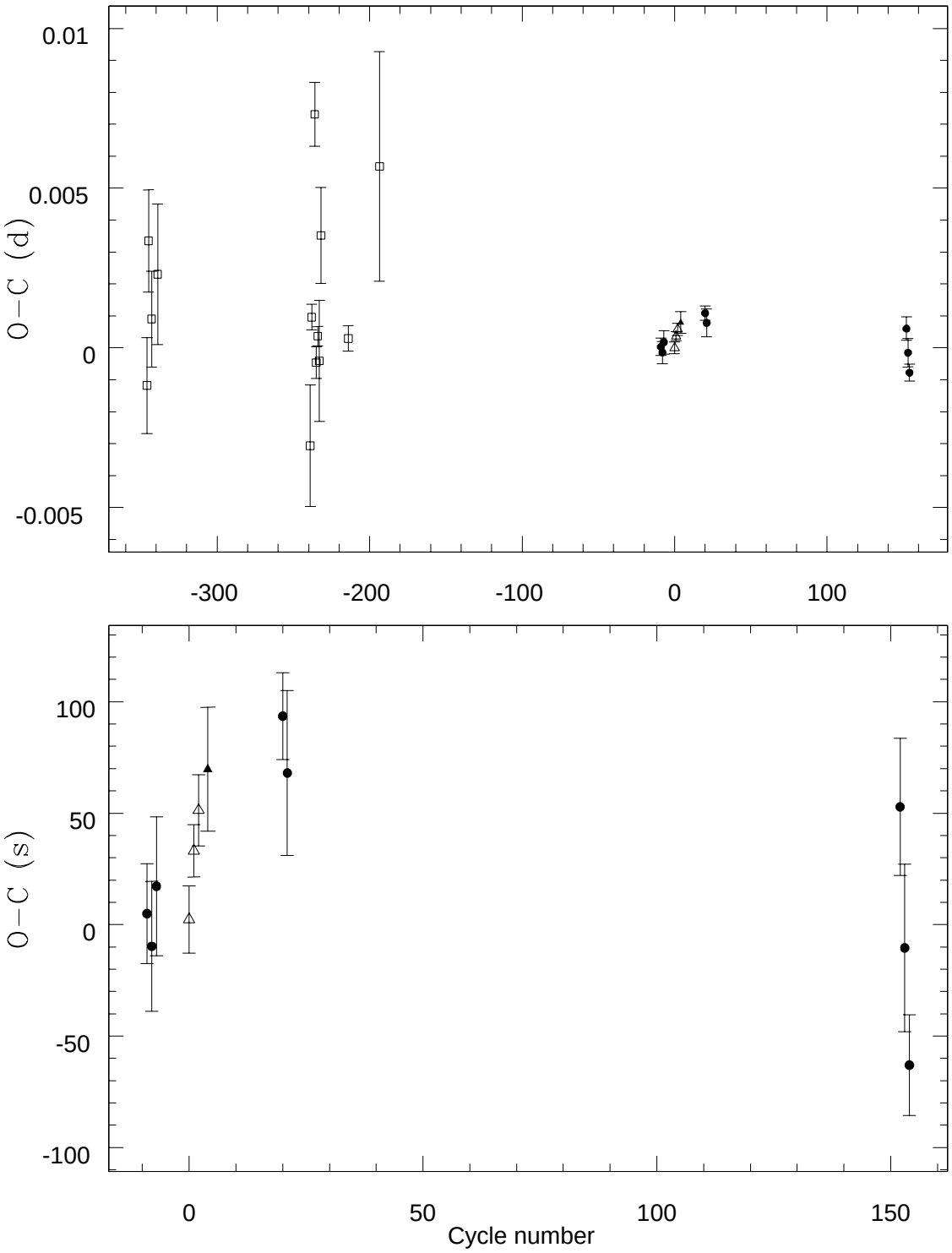

Figure 20: Top: $O-C$ residuals of mid-transit times of the TrES-1 system including all the previously published data and WHT data. Open squares: Charbonneau et al. (2005); filled triangles: Narita et al. (2007); open triangles: Winn et al. (2007b); filled circles: this work. Bottom: The same as the top but zoomed for clarity. The cycle is in a number of periods from the epoch given by Eq. (65).

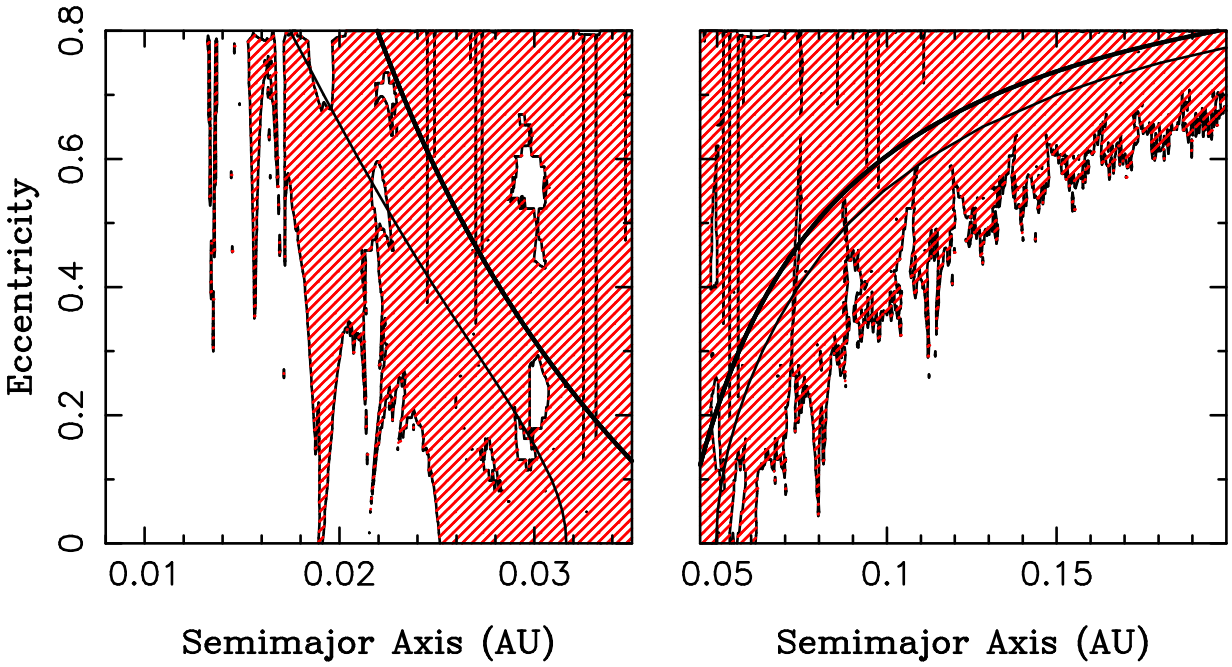

Figure 21: A numerical survey of the TrES-1 system carried out by D. Nesvorný shows 80-s TTVs caused by an inner (left plot) and outer (right plot) 5 Earth-masses planet ($m_2 = 15 \times 10^{-6}$ $M_\odot$). The shaded area excludes a range of possible eccentricities and semimajor axes for a putative 5 Earth-masses inner/outer planet in the system based on our observational non-detection of TTVs greater than ±80 s. *The thick solid line shows a boundary where a collision between the two planets can occur (the same as in Fig. 17). The thin solid line represents a Hill stability. Credit Nesvorný.*

7.4.1 Transit timing variations analysis

The mean $O-C = 17 \pm 48$ s for all our observations, where the quoted error is the rms scatter in the $O-C$ values and is larger than the mean $O-C$ uncertainty ~ 30 s. However, the rms scatter is less than 2σ significant and we did not find any conclusive evidence of a perturbing body in this system.

Our observations of the TrES-1 system show no evidence of TTVs larger than about ±80 s. We used this conclusion to place mass limits on the existence of planets on orbits interior and exterior to TrES-1b similarly as in section §6.4.1. We determined all mid-transit times of TrES-1b over a time-span of 500 days, an interval long enough to cover at least 14 orbits of all perturbing planets we can exclude, and used these data to estimate TTVs.

Figure 21 shows the range of the inner and outer planetary orbits that produce TTVs smaller/larger than 80 seconds and are thus compatible/incompatible with our TTV observations of the TrES-1 system. The shaded area in Fig. 21 excludes a range of possible eccentricities and semimajor axes for a putative 5 Earth-masses inner/outer planet in the system. Our observations show no evidence for an outer planet down to 5 Earth masses

in the 2:1 and 3:2 exterior resonance orbits with TrES-1b and for the majority of possible eccentricities of the perturber orbit (see Fig. 21) an inner planet down to 5 Earth masses in the 1:2, 1:3 and 2:3 interior resonance orbits with the transiting planet.

Not all of the resonant orbits are Hill stable. We computed Hill stability similarly as for the HD 189733 system (see section §6.4.1) and displayed it in Fig. 21 with thin solid line. The same as for the HD 189733 system applies to the TrES-1 system about eccentric or inclined perturbing planets (Nesvorný, 2009).

Madhusudhan & Winn (2009) found an upper limit of 9.9 $M_\oplus$ for a Trojan in the TrES-1 system. Our TTVs show no evidence for the existence of Trojans with masses higher than 8.3 $M_\oplus$ if their libration amplitudes are similar as for Trojans orbiting near the Sun-Jupiter Lagrange points (Ford & Holman, 2007).

Kipping (2009) predicted TTV amplitude of 3.07 s and TDV amplitude of 5.97 s for an Earth-mass exomoon in a circular orbit about TrES-1b. Increasing the eccentricity of the moon's orbit decreases TTV amplitude, but increases TDV amplitude. However, for the TrES-1 system these variations are too small to be detectable in our data.

7.5 Conclusions and discussion

The accuracy of our measurements could be better in the absence of systematics in our data or in case of their proper elimination. Then we would be able to identify any possible stellar activity features that are now hidden in the data noise/systematics and a proper analysis taking into account a stellar activity improving the mid-transit time accuracy could be done.

Our observations show no evidence for an outer planet down to 5 Earth masses in the 2:1 and 3:2 exterior resonance orbits with TrES-1b and for the majority of possible eccentricities of the perturber orbit (see Fig. 21) an inner planet down to 5 Earth masses in the 1:2, 1:3 and 2:3 interior resonance orbits with the transiting planet. We found no evidence for the existence of Trojans with masses higher than 8.3 $M_\oplus$ if their libration amplitudes are similar as for Trojans orbiting near the Sun-Jupiter Lagrange points (Ford & Holman, 2007).

Based on our data analyses, we recommend additional 'rules of thumb' to these of Gillon et al. (2008): for a high accurate ground-based photometry instruments on telescopes with an equatorial mount placed in a direct Cassegrain focus should be favoured.

8 Conclusions and perspectives

During my Ph.D. studies I intended to better understand distant planetary systems by improving and investigating two fields – barycentric corrections and light-curve modelling. In addition I explored statistical properties of extrasolar planets which may reveal interesting connections between planetary system properties and their formation and evolution history.

I have improved the accuracy of barycentric corrections of radial velocity and time to a few $\mathrm{cm\,s^{-1}}$ and a few hundredths of s, respectively. This can have a great impact for a future, when the expected accuracy of radial-velocity measurements is of the order of $\mathrm{cm\,s^{-1}}$ and thus an accurate correction is essential.

I observed new radial velocities of the 51 Peg system to verify the possible changes in the observed minus calculated values of this system. I did not find any evidence supporting expected variations.

I have developed the program for light-curve modelling of transiting extrasolar systems. I have used the Markov-Chain Monte Carlo simulations to estimate system parameters, mid-transit times and the uncertainties. Reliable determination of mid-transit times is crucial for further investigation of deviations from the predicted mid-transit times, which can reveal the presence of additional bodies in the system, or place limits on their existence. Discovery of such bodies would further constrain theories of planetary system formation and evolution.

I reduced the data of two extrasolar transiting systems, HD 189733 and TrES-1. I modelled light curves using the Markov-Chain Monte Carlo simulations and the resulting mid-transit times were used to search for additional bodies. I did not find any evidence of additional bodies in these two systems due to still limited sets of data, but constraints on their existence were placed.

The observations of the HD 189733 system spanning more than two years show no evidence for the presence of planets down to 1 Earth mass in the 2:1, 3:2 and 5:3 exterior resonance orbits, planets down to 1 Earth mass in the 1:2, 1:3, 2:3 and 2:5 interior resonance orbits, and planets down to 2 Earth masses in the 1:4 interior resonance orbit with HD 189733b. These are the strongest limits to date on the presence of other planets in this system. The highest limit on a Trojan mass is 5.3 $\mathrm{M_\oplus}$ if its libration amplitude is similar as for Trojans orbiting near the Sun-Jupiter Lagrange points.

Limits on additional bodies are less constraining for the TrES-1 system. The observations show no evidence for an outer planet down to 5 Earth masses in the 2:1 and 3:2 exterior resonance orbits with TrES-1b and for the majority of possible eccentricities of the perturber orbit an inner planet down to 5 Earth masses in the 1:2, 1:3 and 2:3 interior resonance orbits with the transiting planet.

Non-detection of additional bodies in the HD 189733 and TrES-1 systems might indicate that bodies more massive than ~ 1 $\mathrm{M_\oplus}$ are not common in systems with the 'hot Jupiter'.

To achieve a reliably determined mid-transit time a good quality photometry is necessary. Therefore I tried to understand systematic errors in the data and concluded that

instruments on telescopes with an equatorial mount placed in a direct Cassegrain focus should be preferred for this purpose.

References

Agol, E., Steffen, J. H., Sari, R., Clarkson, W. 2005, MNRAS, 359, 567

Agol, E., Steffen, J. H. 2007, MNRAS, 374, 941

Agol, E., Cowan, N. B., Bushong, J., Knutson, H., Charbonneau, D., Deming, D., Steffen, J. H. 2009, IAUS, 253, 209

Alibert, Y., Mordasini, C., Benz, W., Winisdoerffer, C. 2005, A&A, 434, 343

Alonso, R., Brown, T. M., Torres, G. et al. 2004, ApJ, 613, L153

Alonso, R., Aigrain, S., Pont, F. et al. 2009, IAUS, 253, 91

Anderson, D. R., Hellier, C., Gillon, M. et al. 2009, submitted to ApJ, ArXiv e-prints: 0908.1553

Bakos, G. Á., Noyes, R. W., Kovács, G., Stanek, K. Z., Sasselov, D. D., Domsa, I. 2004, PASP, 116, 266

Bakos, G. Á., Pál, A., Latham, D. W., Noyes, R. W., Stefanik, R. P. 2006a, ApJ, 641, L57

Bakos, G. Á., Knutson, H. A., Pont, F. et al. 2006b, ApJ, 650, 1160

Bakos, G. Á., Torres, G., Pál, A. et al. 2009, ArXiv e-prints: 0901.0282

Barnes, J. W., O'Brien, D. P. 2002, ApJ, 575, 1087

Barnes, J. W. 2007, PASP, 119, 986

Bennett, D. P., Bond, I. A., Udalski, A. et al. 2008, ApJ, 684, 663

Boss, A. P., Wetherill, G. W., Haghighipour, N. 2002, Icar, 156, 291

Boss, A. P. 2008, ApJ, 677, 607

Boss, A. P. 2009, ApJ, 694, 107

Bouchy, F., Udry, S., Mayor, M. et al. 2005, A&A, 444, L15

Bracewell, R. N., MacPhie, R. H. 1979, Icar, 38, 136

Campbell, B., Walker, G. A. H., Yang, S. 1988, ApJ, 331, 902

Capitaine, N., Wallace, P. T., Chapront, J. 2003, A&A, 412, 567

Chambers, J. E. 2006, ApJ, 652, L133

Charbonneau, D., Brown, T. M., Latham, D. W., Mayor, M. 2000a, ApJ, 529, L45

Charbonneau, D., Noyes, R. W. 2000b, ASPC, 219, 461

Charbonneau, D., Brown, T. M., Noyes, R. W., Gilliland, R. L. 2002, ApJ, 568, 377

Charbonneau, D., Allen, L. E., Megeath, S. T. et al. 2005, ApJ, 626, 523

Charbonneau, D., Brown, T. M., Burrows, A., Laughlin, G. 2007, Protostars and Planets V, University of Arizona Press, 701

Chatterjee, S., Ford, E. B., Matsumura, S., Rasio, F. A. 2008, ApJ, 686, 580

Claret, A. 2000, A&A, 363, 1081

Cochran, W. D., Redfield, S., Endl, M., Cochran, A. L. 2008, ApJ, 683, L59

Croll, B., Matthews, J. M., Rowe, J. F. et al. 2007, ApJ, 671, 2129

de Mooij, E. J. W., Snellen, I. A. G. 2009, A&A, 493, L35

Deming, D., Seager, S., Richardson, L. J., Harrington, J. 2005, Nature, 434, 740

Díaz, R. F., Rojo, P., Melita, M., Hoyer, S., Minniti, D., Mauas, P. J. D., Ruíz, M. T. et al. 2008, ApJ, 682, L49

Dittmann, J. A., Close, L. M., Green, E. M., Fenwick, M. 2009, ApJ, 701, 756

Dong, S., Bond, I. A., Gould, A. et al. 2009, ApJ, 698, 1826

Dunham, E. W., Mandushev, G. I., Taylor, B. W., Oetiker, B. 2004, PASP, 116, 1072

Einstein, A. 1936, Sci, 84, 506

Fabrycky, D., Tremaine, S. 2007, ApJ, 669, 1298

Ford, E. B. 2005, AJ, 129, 1706

Ford, E. B. 2006a, ApJ, 642, 505

Ford, E. B., Gaudi, B. S. 2006b, ApJ, 652, L137

Ford, E. B., Holman, M. J. 2007, ApJ, 664, L51

Fortney, J. J., Lodders, K., Marley, M. S., Freedman, R. S. 2008, ApJ, 678, 1419

Gaudi, B. S., Winn, J. N. 2007, ApJ, 655, 550

Gelman, A., Rubin, D. B. 1992, Stat. Sci., 7, 457

Gelman, A., Carlin, J. B., Stern, H. S., Rubin, D. B. 2003, Bayesian Data Analysis, Chapman & Hall, New York

Gibson, N. P., Pollacco, D., Simpson, E. K. et al. 2009a, ApJ, 700, 1078

Gibson, N. P., Pollacco, D., Barros, S. et al. 2009b, submitted to MNRAS

Gillon, M., Pont, F., Moutou, C., Bouchy, F., Courbin, F., Sohy, S., Magain, P. 2006, A&A, 459, 249

Gillon, M., Pont, F., Demory, B. O. et al. 2007, A&A, 472, L13

Gillon, M., Anderson, D. R., Demory, B. O., Wilson, D. M., Hellier, C., Queloz, D., Waelkens, C. 2008, IAUS, 253, ArXiv e-prints: 0806.4911

Gillon, M. 2009, submitted to MNRAS, ArXiv e-prints: 0906.4904

Gladman, B. 1993, Icar, 106, 247

Gonzalez, G. 1997, MNRAS, 285, 403

Griffin, R. F., Griffin, R. E. 1973, MNRAS, 162, 243

Hadrava, P. 1990, CoSka, 20, 23

Hadrava, P. 1998, HvaOB, 22, 75

Hadrava, P. 2004, PAICz, 92, 1

Hansen, B. M. S., Barman, T. 2007, ApJ, 671, 861

Harmanec, P., Mayer, P. 2008, Lecture notes on Binary stars, Charles University, Prague, http://astro.mff.cuni.cz/vyuka/AST019/ast019.pdf (in Czech)

Hartman, J. D., Bakos, G. A., Torres, G. et al. 2009, ArXiv e-prints: 0904.4704

Hatzes, A. P., Cochran, W. D., Bakker, E. J. 1998, ApJ, 508, 380

Hatzes, A. P., Cochran, W. D., Endl, M., McArthur, B., Paulson, D. B., Walker, G. A. H., Campbell, B., Yang, S. 2003, ApJ, 599, 1383

Hébrard, G., Bouchy, F., Pont, F. et al. 2008, A&A, 488, 763

Henry, G. W., Marcy, G. W., Butler, R. P., Vogt, S. S. 2000, ApJ, 529, L41

Heyl, J. S., Gladman, B. J. 2007, MNRAS, 377, 1511

Holman, M. J., Murray, N. W. 2005, Sci, 307, 1288

Holman, M. J., Winn, J. N., Latham, D. W. et al. 2006, ApJ, 652, 1715

Hrudková, M. 2005, Accurate measurements of radial velocities to extra-solar planet detection, Diploma thesis, Astronomical Institute of the Charles University, Prague

Hrudková, M., Harmanec, P. 2006, Tenth Anniversary of 51 Peg-b: Status of and prospects for hot Jupiter studies proceedings, 141

Hrudková, M., Skillen, I., Benn, C., Pollacco, D., Gibson, N., Joshi, Y., Harmanec, P., Tulloch, S. 2009, IAUS, 253, 446

Johnson, J. A., Winn, J. N., Albrecht, S., Howard, A. W., Marcy, G. W., Gazak, J. Z. 2009, accepted to PASP, ArXiv e-prints: 0907.5204

Kalas, P., Fitzgerald, M. P., Clampin, M., Graham, J. R., Chiang, E., Kite, E. S., Stapelfeldt, K., Krist, J. 2009, AAS, 41, 491

Karttunen, H. 2003, Fundamental astronomy, Springer Berlin, 2003

Kipping, D. M. 2008, MNRAS, 389, 1383

Kipping, D. M. 2009, MNRAS, 392, 181

Knutson, H. A., Charbonneau, D., Cowan, N. B. et al. 2008, ApJ, 690, 822

Lafrenière, D., Marois, C., Doyon, R., Nadeau, D., Artigau, É. 2007, ApJ, 660, 770

Lagrange, A. M., Gratadour, D., Chauvin, G. et al. 2009, A&A, 493, L21

Latham, D. W., Mazeh, T., Stefanik, R. P., Mayor, M., Burki, G. 1989, Nature, 339, 38

Laughlin, G., Chambers, J. E. 2002, AJ, 124, L592

Leger, A., Rouan, D., Schneider, J. et al. 2009, ArXiv e-prints: 0908.0241

Li, C-H., Benedick, A. J., Fendel, P. et al. 2008, Nature, 452, 610

Lieske, J. H., Lederle, T., Fricke, W., Morando, B. 1977, A&A, 58, 1

Madhusudhan, N., Winn, J. N. 2009, ApJ, 693, 784

Mandel, K., Agol, E. 2002, ApJ, 580, 171

Marcy, G. W., Butler, R. P. 1992, PASP, 104, 270

Marois, C., Lafrenière, D., Doyon, R., Macintosh, B., Nadeau, D. 2006, ApJ, 641, 556

Marois, C., Macintosh, B., Barman, T., Zuckerman, B., Song, I., Patience, J., Lafrenière, D., Doyon, R. 2008, Sci, 322, 1348

Mathews, P. M., Herring, T. A., Buffett, B. A. 2002, JGRB, 107, B4, ETG 3–1

Mayer, L., Quinn, T., Wadsley, J., Stadel, J. 2002, Sci, 298, 1756

Mayor, M., Queloz, D. 1995, Nature, 378, 355

Mazeh, T., Naef, D., Torres, G. et al. 2000, ApJ, 532, L55

Mazeh, T., Zucker, S., Pont, F. 2005, MNRAS, 356, 955

McCullough, P. R., Stys, J. E., Valenti, J. A., Fleming, S. W., Janes, K. A., Heasley, J. N. 2005, PASP, 117, 783

McLaughlin, D. B. 1924, ApJ, 60, 22

Miller-Ricci, E., Rowe, J. F., Sasselov, D. et al. 2008, ApJ, 682, 586

Miller-Ricci, E., Rowe, J. F., Sasselov, D. et al. 2008, ApJ, 682, 593

Miralda-Escudé, J. 2002, ApJ, 564, 1019

Mizuno, H. 1980, PThPh, 64, 544

Moutou, C., Hébrard, G., Bouchy, F. et al. 2009, A&A, 498, L5

Murphy, M. T., Udem, Th., Holzwarth, R. et al. 2007, MNRAS, 380, 839

Murray, C. D., Dermott, S. F. 2000, Solar System Dynamics, Cambridge Univ. Press

Naef, D., Mayor, M., Beuzit, J. L., Perrier, C., Queloz, D., Sivan, J. P., Udry, S. 2004, A&A, 414, 351

Naef, D., Mayor, M., Beuzit, J. L., Perrier, C., Queloz, D., Sivan, J. P., Udry, S. 2005, ESASP, 560, 833

Narita, N., Enya, K., Sato, B. et al. 2007, PASJ, 59, 763

Narita, N., Sato, B., Ohshima, O., Winn, J. N. 2008, PASJ, 60, L1

Narita, N., Hirano, T., Sato, B. et al. 2009a, accepted to PASJ, ArXiv e-prints: 0905.4727

Narita, N., Sato, B., Hirano, T., Tamura, M. 2009b, submitted to PASJ, ArXiv e-prints: 0908.1673

Nesvorný, D., Morbidelli, A. 2008, ApJ, 688, 636

Nesvorný, D. 2009, ApJ, 701, 1116

Pepe, F. A., Bouchy, F., Queloz, D., Mayor, M. 2003, ASPC, 294, 39

Pepe, F. A., Lovis, C. 2008, PhST, 130, a4007

Pollacco, D. L., Skillen, I., Cameron, A. C. et al. 2006, PASP, 118, 1407

Pont, F., Zucker, S., Queloz, D. 2006, MNRAS, 373, 231

Pont, F., Aigrain, S., Bakos, G. et al. 2007a, ASPC, 366, 3

Pont, F., Gilliland, R. L., Moutou, C. et al. 2007b, A&A, 476, 1347

Pont, F., Hébrard, G., Irwin, J. M. et al. 2009, A&A, 502, 695

Pravdo, S. H., Shaklan, S. B. 2009, ApJ, 700, 623

Press, W. H., Teukolsky, S. A., Vetterling, W. T., Flannery, B. P. 1992, Numerical recipes, University Press, Cambridge

Rabus, M., Alonso, R., Belmonte, J. A. et al. 2009, A&A, 494, 391

Ron, C., Vondrák, J. 1986, BAC, 37, 96

Rossiter, R. A. 1924, ApJ, 60, 15

Santos, N. C., Israelian, G., Mayor, M. 2001, A&A, 373, 1019

Sartoretti, P., Schneider, J. 1999, A&AS, 134, 553

Seager, S., Sasselov, D. D. 2000, ApJ, 537, 916

Seager, S., Mallén-Ornelas, G. 2003, ApJ, 585, 1038

Seidelmann, P. K. 1982, Cel. Mech., 27, 79

Simon, A., Szatmáry, K., Szabó, Gy. M. 2007, A&A, 470, 727

Sing, D. K., López-Morales, M. 2009, A&A, 493, L31

Smith, B. A., Terrile, R. J. 1984, Sci, 226, 1421

Southworth, J., Wheatley, P. J., Sams, G. 2007, MNRAS, 379, L11

Sozzetti, A., Yong, D., Torres, G. et al. 2004, ApJ, 616, L167

Standish, E. M. 1998a, JPL IOM, 312, F–98–048.

Standish, E. M. 1998b, A&A, 336, 381

Steffen, J. H., Agol, E. 2005, MNRAS, 364, L96

Steffen, J. H. 2006, Ph.D. dissertation, University of Washington

Strand, K. A. 1943, PASP, 55, 29

Stumpff, P. 1977, A&A, 56, 13

Stumpff, P. 1979, A&A, 78, 229

Stumpff, P. 1980, A&AS, 41, 1

Szabó, Gy. M., Szatmáry, K., Divéky, Zs., Simon, A. 2006, A&A, 450, 395

Tegmark, M., Strauss, M. A., Blanton, M. R. et al. 2004, PhRvD, 69, 103501

Udalski, A., Paczynski, B., Zebrun, K. et al. 2002, AcA, 52, 1

Udry, S., Santos, N. C. 2007, ARA&A, 45, 397

Valenti, J. A., Butler, R. P., Marcy, G. W. 1995, PASP, 107, 966

van de Kamp, P. 1963, ApJ, 68, 515

Wahr, J. H. 1981, Geophys. J., 64, 705

Walker, G. A. H., Bohlender, D. A., Walker, A. R., Irwin, A. W., Yang, S. L. S., Larson, A. 1992, ApJ, 396, L91

Walker, G. A. H. 2008, Nature, 452, 538

Ward, W. R., Hahn, J. M. 2003, AJ, 125, 3389

Welsh, W. F. 2009, BAAS, 41, 373

Winn, J. N., Holman, M. J., Henry, G. W. et al. 2007a, AJ, 133, 1828

Winn, J. N., Holman, M. J., Roussanova, A. 2007b, ApJ, 657, 1098

Winn, J. N., Howard, A. W., Johnson, J. A. et al. 2009a, ApJ, in press, ArXiv e-prints: 0907.5205

Winn, J. N., Johnson, J. A., Albrecht, S., Howard, A. W., Marcy, G. W., Crossfield, I. J., Holman, M. J. 2009b, submitted to ApJ Letters, ArXiv e-prints: 0908.1672

Winn, J. N., Johnson, J. A., Fabrycky, D. et al. 2009c, ApJ, 700, 302

Wolszczan, A., Frail, D. A. 1992, Nature, 355, 145

Woolard, E. W., Clemence, G. M. 1966, Spherical Astromony, Academic Press, London

Zhou, J. L., Aarseth, S. J., Lin, D. N. C., Nagasawa, M. 2005, ApJ, 631, L85

List of publications and conference contributions related to this thesis

1. **Hrudková, M.**; Harmanec, P.: 2006, *51 Peg: a star with a second planet or a pulsating star?*, Tenth Anniversary of 51 Peg-b: Status of and prospects for hot Jupiter studies, proceedings, p. 141–143

2. **Hrudková, M.**: 2006, *The Accurate Barycentric Corrections for the Detection of Extrasolar Planets*, WDS'06 Proceedings of Contributed Papers: Part III – Physics (eds. J. Šafránková and J. Pavlů), Prague, Matfyzpress, p. 18–23

3. Pollacco, D.; Skillen, I.; Collier Cameron, A.; Loeillet, B.; Stempels, H. C.; Bouchy, F.; Gibson, N. P.; Hebb, L.; Hébrard, G.; Joshi, Y. C.; McDonald, I.; Smalley, B.; Smith, A. M. S.; Street, R. A.; Udry, S.; West, R. G.; Wilson, D. M.; Wheatley, P. J.; Aigrain, S.; Alsubai, K.; Benn, C. R.; Bruce, V. A.; Christian, D. J.; Clarkson, W. I.; Enoch, B.; Evans, A.; Fitzsimmons, A.; Haswell, C. A.; Hellier, C.; Hickey, S.; Hodgkin, S. T.; Horne, K.; **Hrudková, M.**; Irwin, J.; Kane, S. R.; Keenan, F. P.; Lister, T. A.; Maxted, P.; Mayor, M.; Moutou, C.; Norton, A. J.; Osborne, J. P.; Parley, N.; Pont, F.; Queloz, D.; Ryans, R.; Simpson, E.: 2008, *WASP-3b: a strongly irradiated transiting gas-giant planet*, Monthly Notices of the Royal Astronomical Society, 385, p. 1576–1584

4. Gibson, N. P.; Pollacco, D.; Simpson, E. K.; Joshi, Y. C.; Todd, I.; Benn, C.; Christian, D.; **Hrudková, M.**; Keenan, F. P.; Meaburn, J.; Skillen, I.; Steele, I. A.: 2008, *Updated parameters for the transiting exoplanet WASP-3b using RISE, a new fast camera for the Liverpool Telescope*, Astronomy & Astrophysics, 492, p. 603–607

5. **Hrudková, M.**, Skillen, I.; Benn, C.; Pollacco, D.; Gibson, N.; Joshi, Y.; Harmanec, P.; Tulloch, S.: 2009, *Searching for transit timing variations in transiting exoplanet systems*, Transiting Planets, Proceedings of the International Astronomical Union, IAU Symposium, 253, p. 446-449

6. Gibson, N. P.; Pollacco, D.; Simpson, E. K.; Barros, S.; Joshi, Y. C.; Todd, I.; Keenan, F. P.; Skillen, I.; Benn, C.; Christian, D.; **Hrudková, M.**; Steele, I. A.: 2009, *A Transit Timing Analysis of Nine Rise Light Curves of the Exoplanet System TrES-3*, The Astrophysical Journal, 700, p. 1078–1085

7. Gibson, N. P.; Pollacco, D.; Barros, S.; Benn, C.; Christian, D.; **Hrudková, M.**; Joshi, Y. C.; Keenan, F. P.; Simpson, E. K.; Skillen, I.; Steele, I. A.; Todd, I.: submitted, *A Transit Timing analysis of seven RISE light curves of the exoplanet system HAT-P-3*, Monthly Notices of the Royal Astronomical Society

8. **Hrudková, M.**; Skillen, I.; Benn, C.; Pollacco, D.; Nesvorný, D.; Augusteijn, T.; Gibson, N. P.; Tulloch, S. M; Joshi, Y.: submitted 24. 8. 2009, *Tight constraints on the existence of additional planets around HD 189733*, Monthly Notices of the Royal Astronomical Society